**Copy No.** _____

# Guide for Mechanistic-Empirical Design
## OF NEW AND REHABILITATED PAVEMENT STRUCTURES

**FINAL DOCUMENT**

## APPENDIX JJ:
## TRANSVERSE JOINT FAULTING MODEL

**NCHRP**

**Prepared for**
**National Cooperative Highway Research Program**
**Transportation Research Board**
**National Research Council**

**Submitted by**
**ARA, Inc., ERES Division**
**505 West University Avenue**
**Champaign, Illinois 61820**

**August 2003**

**Acknowledgment of Sponsorship**

This work was sponsored by the American Association of State Highway and Transportation Officials (AASHTO) in cooperation with the Federal Highway Administration and was conducted in the National Cooperative Highway Research Program which is administered by the Transportation Research Board of the National Research Council.



**Acknowledgements**

The research team for NCHRP Project 1-37A: Development of the 2002 Guide for the Design of New and Rehabilitated Pavement Structures consisted of Applied Research Associates, Inc., ERES Consultants Division (ARA-ERES) as the prime contractor with Arizona State University (ASU) as the primary subcontractor. Fugro-BRE, Inc., the University of Maryland, and Advanced Asphalt Technologies, LLC served as subcontractors to either ARA-ERES or ASU along with several independent consultants.

Research into the subject area covered in this Appendix was conducted at ARA-ERES. The author of this appendix is Dr. Lev Khazanovich. Dr. Darter provided technical and managerial coordination of the rigid pavement design group, monitored progress, set schedules and deadlines, and provided periodic technical review of research results as they became available. Data used in model calibration and verification was assembled by Mr. Leslie Titus-Glover.

**Foreword**

This appendix describes the faulting mechanism, as well as adaptation of the chosen best-available JPCP transverse joint faulting models and calibration and implementation of the adapted model into the Design Guide.

The information contained in this appendix serves as a supporting reference to discussions presented in PART 3, Chapters 4 and 7 of the Design Guide.

# APPENDIX JJ: TRANSVERSE JOINT FAULTING MODEL

## INTRODUCTION

The AASHTO design procedure has used pavement serviceability as its only design criterion for nearly 40 years. This situation has had both positive and negative implications for design adequacy. On the positive side, the serviceability concept has ensured that the Nation's pavements are designed to provide the traveling public with a smooth highway. It is also used as a basis for triggering rehabilitation when serviceability needs/requirements are no longer being met. On the negative side, pavement designs based on serviceability alone do not directly address prevention of specific distresses. Performance analysis of in-service pavements shows that these distresses often lead to a decrease in serviceability and eventually to a premature need for pavement rehabilitation.

Transverse joint faulting is one of the main types of distresses in jointed portland cement pavements (JPCP) affecting its serviceability. Joint faulting is defined as the difference in elevation between adjacent joints at a transverse joint. The development of faulting is often attributed to a combination of repeated heavy axle loads, insufficient load transfer between the adjacent slabs, free moisture in the pavement structure, and erodible base or subgrade material. When excess moisture exists in a pavement with an erodible base or underlying fine-grained subgrade material, repeated vehicle loadings typically cause the mixture of water and fine material (fines) to be removed from beneath the leave slab corner and ejected to the surface through the transverse joint or along the shoulder. This process, commonly referred to as pumping, will eventually result in a void below the leave slab corner. In addition, some of the fines that are not ejected will be deposited under the approach slab corner, causing the approach slab to rise. This combination of a buildup of material beneath the approach corner and the loss of support resulting from a void under the leave corner can lead to significant faulting at the joint (especially for JPCP without dowels). Significant joint faulting has a major impact on the life cycle cost of the pavement in terms of early rehabilitation and vehicle operating costs.

This appendix describes the faulting mechanism, as well as adaptation of the chosen best-available JPCP transverse joint faulting models and calibration and implementation of the adapted model in the 2002 Design Guide.

## FAULTING MECHANISM

Faulting is the result of excessive slab edge and corner deflections that cause erosion and pumping of fines from beneath a loaded leave slab. These fines are then deposited under the approach slab. The rate of progression of JCP faulting is increased significantly when a given pavement exhibits a combination of poor load transfer across a joint or crack, heavy axle loads, free moisture beneath the pavement, and erosion and pumping of the supporting base, subbase, or subgrade material from underneath the slab or treated base.[1, 2, 3, 4, 5, 6, 7, 8, 9] The following conditions must exist for faulting to occur: [2, 3, 6, 7, 8]

- Significant differential deflections of adjacent slabs that impart energy to the underlying pavement materials. These deflections cause the movement of the saturated underlying pavement material as equilibrium is reestablished, resulting in erosion and pumping. The differential energy across the joint or crack is amplified by several factors, including heavy wheel loads and inadequate load transfer.
- Underlying pavement materials that are erodible. An unstabilized or weakly stabilized material with a high percentage of fines is a prime candidate for erosion.
- The presence of free water in the pavement structure, which leads to the saturation of the underlying materials at the slab/base or treated base/subgrade interface and provides transportation for pumping and erosion of fines.

Because the erosion of material from underneath the leave slab is caused by pumping, it is important to explain pumping in order to understand the mechanism that leads to faulting.

Pumping refers to the ejection of material from beneath the leave slab of a pavement and its deposition along the pavement edge, under the approach slab, or ejection onto the pavement surface through the joints.[4,5, 6, 7, 8] It is caused by the rapid vertical deflection of the leave slab at a joint or crack, which leads to an ejection of fines and water. As a wheel load approaches a joint or crack, the leave slab deflects, causing water and fine material beneath the leave slab to be forced under the approach slab. Some of the water and materials escape through the joint or crack, while the remaining water and fines are distributed under the approach slab. The entire cycle is repeated with the application of axle loads to the pavement. The buildup of loose material under the approach slab, which elevates it at the joint or crack and the depression of the leave slab, results in the difference in elevation across the joint or crack, leading to faulting.

At the AASHO Road Test, although fine material often washed upward through joints and cracks, this was negligible when compared to the amount of material deposited along the edge of the joint or crack.[10] It was also realized that for JCP with a base or subbase experiencing pumping, the material ejected was from the base or subbase (usually including the coarse fraction) rather than the underlying subgrade material. Pumping of the embankment or subgrade soil was generally confined to those sections without a base or subbase or those with very thin base or subbase (< 75 mm) that pumped so severely than all the granular material had been pumped out prior to failure. It is clear, therefore, that the material most susceptible to erosion and pumping is the unstabilized or weakly stabilized (erodible) layer directly beneath the lowest bound layer under the PCC slab.[10]

Results from the AASHO Road Test provided considerable information about the mechanism of pumping. As part of the Road Test, after each rainfall, all pavement sections under traffic were inspected for signs of pumping, and a rough estimate was made of the material pumped. The result was used to calculate a pumping index that approximated the accumulated volume of material ejected per unit length of pavement, averaged over the test section. The following were observed for the Road Test pavements:[10]

- The average pumping index for failed sections (present serviceability = 1.5) was 134.
- The average pumping index for surviving sections was 34.
- There was no clear-cut value of pumping index corresponding to a serviceability of 1.5.

- No consistent trend was found relating pumping index to untreated granular subbase thickness.
- There was no significant difference between reinforced and nonreinforced JCP (both had dowels).
- Pumping index decreased as slab thickness increased. However, pumping index increased significantly for pavements with the same slab thickness as more axle loads were applied (or vice versa).

By removing the concrete slab from the failed sections and sampling the underlying material, it was observed that erosion and pumping had apparently been due to the movement of water moving across the top of the subbase. The remaining subbase material was relatively intact. The subbase materials for the failed sections had permeabilities ranging from 0.00288 to 1.512 m/day. Pumping could have been reduced if the subbase material was stabilized and therefore resistant to erosion, or if the infiltrated water could be quickly drained through a subsurface drainage system before the pavement was subjected to heavy wheel loads.[10]

Stabilizing the base material does not always prevent pumping, because pumping can occur directly beneath a treated base overlying a subgrade material susceptible to pumping. This can be reduced by placing a thick granular layer (> 3 in) material between the treated base and subgrade.

Although pumping is the basic mechanism that leads to faulting, several other factors can exacerbate the distress and need to be taken into account. Field results show that the reduced support from upward curling or warping of the slab at the joint or crack will increase pumping pressures because of the higher deflections experienced.[11] The potential for faulting of a pavement is significantly lower in the summer months, when the joints are closed due to thermal expansion.[11] Faulting increases in the other seasons, when the joint width is widest and the underlying materials typically have a higher moisture content.[11, 12] The impact of a heavy wheel load as it crosses the joint or crack is far more pronounced if there is inadequate load transfer. The higher differential deflections that occur due to poor or nonexistent load transfer at the joint or crack lead to more pumping and faulting. However, it is important to note that, even for a pavement with 100 percent load transfer, deflections at the joint or crack can be abnormally high and result in horizontal pumping (movement of material from beneath the leave to beneath the approach slab).[4]

The next few sections describe the results from various research studies that have reported the effect of design features and site condition variables on faulting. Critical response parameters used in the formation of M-E based faulting models and available empirical and M-E models are also presented and discussed.

## EXISTING JPCP TRANSVERSE JOINT FAULTING MODELS

In this study, many of the faulting models developed under previous research were reviewed. During the review process, specific attention was paid to the variables chosen for inclusion in the

models. The details of each of the faulting models reviewed under this study are described separately in the following sections.

**SHRP P-020 JPCP Transverse Joint Faulting Model**

In a SHRP study conducted by Simpson et al. in 1994, titled Early Analysis of LTPP General Pavement Studies Data, separate JPCP faulting models were developed for doweled and non-doweled JPCP.[13] Each of these models are presented as follows:

SHRP P-020 Faulting Model for JPCP With Dowels

$$FAULTD = CESAL^{0.25} * [0.0238 + 0.0006 * \left(\frac{JTSPACE}{10}\right)^2 + 0.0037 * \left(\frac{100}{KSTATIC}\right)^2 + 0.0039 * \left(\frac{AGE}{10}\right)^2 - 0.0037 * EDGESUP - 0.0218 * DOWELDIA] \quad (1)$$

where:

| | | |
|---|---|---|
| FAULTD | = | Mean transverse doweled joint faulting, in. |
| CESAL | = | Cumulative 80-kN (18-kip) ESAL's in traffic lane, millions. |
| JTSPACE | = | Mean transverse joint spacing, ft. |
| KSTATIC | = | Mean backcalculated static k-value, psi/in. |
| AGE | = | Age since construction, years. |
| EDGESUP | = | Edge support.<br>1 = tied PCC shoulder.<br>0 = any other shoulder type. |
| DOWELDIA | = | Diameter of dowels in transverse joints, in. |

Statistics:

| | | |
|---|---|---|
| N | = | 59. |
| $R^2$ | = | 0.534. |
| SEE | = | 0.028 in (0.7 mm). |

SHRP P-020 Faulting Model for JPCP Without Dowels

The faulting model developed for non-doweled JPCP was the following:

$$FAULTND = CESAL^{0.25} * [-0.07575 + 0.0251 * \sqrt{AGE} + 0.0013 * \left(\frac{PRECIP}{10}\right)^2 + 0.0012 * \left(FI * \frac{PRECIP}{1000}\right) - 0.0378 * DRAIN] \quad (2)$$

where:

| | | |
|---|---|---|
| FAULTND | = | Mean transverse non-doweled joint faulting, in. |
| CESAL | = | Cumulative 80-kN (18-kip) ESAL's in traffic lane, millions. |
| PRECIP | = | Mean annual precipitation, in. |
| FI | = | Mean freezing index, °F-days. |
| AGE | = | Age since construction, years. |
| DRAIN | = | Drainage type.<br>1 = longitudinal subdrainage.<br>0 = otherwise. |

Statistics:

| | | |
|---|---|---|
| N | = | 25. |
| $R^2$ | = | 0.550. |
| SEE | = | 0.047 in (1.2 mm). |

Both of these models predict faulting as a function of traffic, age, and various site conditions and pavement design features. A review of the output of these models indicates a trend that non-doweled pavements develop more faulting than doweled pavements. In addition, for doweled pavements, faulting decreases as dowel diameter increases. As expected, both models were positively correlated with cumulative ESAL's (i.e., faulting increases with an increase in cumulative ESAL's). Pavement design features that were found to be significant in the models included drainage type, joint spacing, base type, and presence of a tied PCC shoulder. Two climatic variables (precipitation and freezing index) were found to significantly affect the development of faulting for non-doweled pavements; however, it is interesting to note that no climate-related variables were included in the model for doweled JPCP.

In the final SHRP P-020 report, the research team that developed these models acknowledged that both models were developed with limited data, which most likely led to relatively low coefficients of correlation and fairly high SEE. Because of these model statistics, the research team stated that improvements could most likely be made to both models.

**FHWA RPPR 1997 JPCP Transverse Joint Faulting Model**

In 1997, Yu et al. also developed separate JPCP faulting models for doweled and non-doweled pavements as part of the FHWA RPPR project.[3] The development of these models identified several pavement design features and site conditions that significantly affect transverse joint faulting. Each of these models is discussed separately below:

RPPR Faulting Model for JPCP With Dowels

$$\begin{aligned} FAULTD = \text{CESAL}^{0.25} * [&0.0628 - 0.0628 * C_d + 0.3673 * 10^{-8} * \text{BSTRESS}^2 \\ &+ 0.4116 * 10^{-5} * \text{JTSPACE}^2 + 0.7466 * 10^{-9} * \text{FI}^2 * \text{PRECIP}^{0.5} \\ &- 0.009503 * \text{BASE} - 0.01917 * \text{WIDENLANE} + 0.0009217 * \text{AGE}] \end{aligned} \quad (3)$$

where:

| | | |
|---|---|---|
| FAULTD | = | Mean transverse doweled joint faulting, in. |
| CESAL | = | Cumulative 80-kN (18-kip) ESAL's in traffic lane, millions. |
| $C_d$ | = | Modified AASHTO drainage coefficient, calculated from database information. |
| BSTRESS | = | Maximum dowel/concrete bearing stress, psi. |
| JTSPACE | = | Mean transverse joint spacing, ft. |
| FI | = | Mean freezing index, °F-days. |
| PRECIP | = | Mean annual precipitation, in. |
| BASE | = | Base type.<br>0 = nonstabilized base.<br>1 = stabilized base. |
| WIDENLANE | = | Widened lane.<br>0 = not widened.<br>1 = widened. |
| AGE | = | Age since construction, years. |

Statistics:

| | | |
|---|---|---|
| N | = | 146. |
| $R^2$ | = | 0.60. |
| SEE | = | 0.022 in (0.56 mm). |

RPPR Faulting Model for JPCP Without Dowels

$$FAULTND = CESAL^{0.25} * [0.2347 - 0.1516 * C_d - 0.000250 * h_{PCC}{}^2/JTSPACE - 0.0115 * BASE + 0.7784 * 10^{-7} * FI^{1.5} * PRECIP^{0.25} - 0.002478 * DAYS90^{0.5} - 0.0415 * WIDENLANE] \quad (4)$$

where:

| | | |
|---|---|---|
| FAULTND | = | Mean transverse non-doweled joint faulting, in. |
| CESAL | = | Cumulative 80-kN (18-kip) ESAL's in traffic lane, millions. |
| $C_d$ | = | Modified AASHTO drainage coefficient, calculated from database information. |
| $h_{PCC}$ | = | PCC slab thickness, in. |
| JTSPACE | = | Mean transverse joint spacing, ft. |
| BASE | = | Base type.<br>0 = nonstabilized base,<br>1 = stabilized base. |
| FI | = | Mean freezing index, °F-days. |
| PRECIP | = | Mean annual precipitation, in. |
| DAYS90 | = | Mean annual number of hot days (days with maximum temperature greater than 32 °C [90°F]). |
| WIDENLANE | = | Widened lane.<br>0 = not widened. |

1 = widened.

Statistics:

| | | |
|---|---|---|
| N | = | 131. |
| $R^2$ | = | 0.45. |
| SEE | = | 0.034 in (0.86 mm). |

The results of these models generally were found to agree with the results from the models developed under the LTPP Early Analysis (SHRP P-020) study.[13] One important characteristic of both RPPR models that was not addressed in the SHRP P-020 models is the inclusion of presence of a widened traffic lane as an independent variable. The presence of a widened traffic lane was found to be negatively correlated with faulting in both RPPR models (i.e., predicted faulting for pavements with a widened lane will be less than that predicted for a similar pavement without a widened lane).

## ACPA JPCP Transverse Joint Faulting Model[8]

In 1994, Wu et al. developed separate mechanistic-empirical JPCP faulting models for doweled and non-doweled pavements for the American Concrete Paving Association (ACPA).[8] These models were extensions of faulting models originally developed for the Portland Cement Association (PCA) in 1977.[14] These models are unique in that they include erodibility of the base/subgrade material as the main factor influencing faulting. Using the concept of Miner's linear damage, the percent of erosion damage occurring at the slab corner was computed using the following equation:[14]

$$EROSION = 100\sum_i \frac{C_2 n_i}{N_i} \quad (5)$$

where:

| | | |
|---|---|---|
| EROSION | = | Percent erosion damage. |
| $n_i$ | = | Expected number of axle load repetitions for each axle group i. |
| $N_i$ | = | Allowable number of repetitions for axle group i. |
| $C_2$ | = | 0.06 for pavements without a tied PCC shoulder and 0.94 for pavements with a tied PCC shoulder. |

Next, the allowable number of load applications (N) was computed as a function of the power, or rate of work, of each axle pass at the corner of the slab. This equation is shown as the following:[14]

$$LogN = 14.524 - 6.777 * (C1 * P - 9.0)^{0.103} \quad (6)$$

where:

| | | |
|---|---|---|
| N | = | Allowable load repetitions to end of design period. |
| P | = | Power (rate of work) of each axle pass at the corner of the slab. |
| C1 | = | $1 - (KSTATIC / 2000 * [4/h_{PCC}])^2$. |
| KSTATIC | = | Modulus of subgrade reaction, psi/in. |
| $h_{PCC}$ | = | Slab thickness, in. |

The power of each axle pass at the corner of the slab is computed using equation 7:[14]

$$P = 268.7 * p^2 / h_{pcc} / KSTATIC^{0.73} \quad (7)$$

where:

P = Power (rate of work) of each axle pass at the corner of the slab.
p = Pressure at slab-foundation interface, psi.

The final JPCP faulting models developed under this ACPA study are included as equations 8 and 9, respectively.[8]

$$FAULTD = EROSION^{0.25} * [0.0038332 * (PRECIP/10)^{1.84121} + 0.0057763 * JTSPACE^{0.38274}] \quad (8)$$

$$FAULTND = EROSION^{0.25} * [9.75873 * 10^{-4} * (PRECIP)^{0.91907} + 0.0060291 * JTSPACE^{0.54428} - 0.016799 * DRAIN] \quad (9)$$

where:

FAULTD = Mean transverse doweled joint faulting, in.
FAULTND = Mean transverse non-doweled joint faulting, in.
EROSION = Calculated accumulated erosion (using equation 5).
PRECIP = Annual precipitation, in.
JTSPACE = Transverse joint spacing, ft.
DRAIN = Dummy variable for the presence of edge drains.
1 = edge drains are present.
0 = edge drains are not present.

An evaluation of these models found that they generally agreed with the JPCP faulting models developed under the RPPR and SHRP P-020 studies.[3, 13] In addition, it was noted that PCC slab thickness was found to be a significant parameter that is negatively correlated with faulting (i.e., an increase in slab thickness results in a decrease in transverse joint faulting).[5] It is also important to note that the presence of edge drains was included in the non-doweled faulting model, whereas no drainage-related variables were used in the doweled model.

## FHWA NAPCOM JPCP Transverse Joint Faulting Model[6]

Under the FHWA Nationwide Pavement Cost Model (NAPCOM) study completed in 1997, Owusu-Antwi et al. developed the following mechanistic-empirical faulting model for doweled and non-doweled JPCP:[6]

$$FAULT = DAMAGE^{0.23} * (0.35 - 0.0277 * BASE - 0.25 * C_d + 2.17 * 10^{-5} * FI) \quad (10)$$

where:

FAULT = Mean transverse joint faulting, in.
DAMAGE = n/N.
n = Cumulative number of actual axle load applications, in thousands.
N = Number of allowable axle load applications, in thousands.
$C_d$ = AASHTO drainage coefficient.
BASE = Base type.
0 = erodible base.
1 = nonerodible base.
FI = Freezing index, °F-days.

Statistics:

N = 101.
$R^2$ = 0.52.
SEE = 0.03 in (0.8 mm).

The allowable number of load applications (N) is defined as follows:

$$Log(N) = 4.27 - 1.6 * Log(DE - 0.002). \quad (11)$$

where:

N = Number of allowable axle load applications, in thousands.
DE = Differential of subgrade elastic energy density.

The NAPCOM model (equation 10) illustrates that the presence of dowels significantly reduces faulting by reducing the differential of subgrade elastic energy density. In addition, the output of the model illustrates trends showing that a stabilized base, stiff subgrade, and improved drainage are negatively correlated with faulting.[6]

**LTPP Data Analysis Study JPCP Transverse Joint Faulting Model[7]**

In 1999, Titus-Glover et al. recalibrated the 1997 NAPCOM JPCP transverse joint faulting model under a FHWA LTPP data analysis contract.[7] This model, recalibrated using LTPP data only, is as follows:

$$FAULT = DAMAGE^{0.3} * [0.05 + 0.00004 * WETDAYS - 0.0024 * DOWDIA - 0.025 * Cd * (0.5 + BASE)] \quad (12)$$

where:

FAULT = Mean transverse joint faulting, in.
DAMAGE = n/N.
n = Cumulative number of actual 90-kN (18-kip) ESAL applications, in thousands.
N = Number of allowable 90-kN (18-kip) ESAL applications, in thousands.
WETDAYS = Annual average number of wet days.
DOWDIA = Dowel diameter, in.
$C_d$ = AASHTO drainage coefficient.
BASE = Base or subbase type.
0 = erodible base.
1 = nonerodible base.

Statistics:

N = 120.
$R^2$ = 0.56.

SEE = 0.03 in (0.8 mm).

The main difference between the recalibrated model and the original NAPCOM model is that the recalibrated model expresses traffic in terms of ESAL's, whereas the original NAPCOM model uses actual axle loads. In addition, the effects of climate are characterized with different variables in the two models. In the original NAPCOM model, the influence of climate is considered by freezing index, whereas the average annual number of wet days was used as the important climatic parameter in the calibrated LTPP model.[7]

**NCHRP 1-34 Model**

The following faulting model was developed procedure is based on the faulting model developed in 1998 by Yu et al. [15]

$$FAULT = DAMAGE0.2475 * [0.2405 - 0.00118 * DAYS90 + 0.001216 * WETDAYS - 0.04336 * BASETYPE - (0.004336 + 0.007059 * (1 - DOWEL)) * LCB] \quad (13)$$

where:

FAULT = Average transverse joint faulting per joint, in.

BASETYPE = Base type.
= 0 if nonstabilized.
= 1 if asphalt stabilized [ATB], cement stabilized [CTB], or lean concrete base [LCB]).

LCB = Presence of lean concrete base.
= 1 if LCB is present.
= 0 if LCB is not present.

WETDAYS = Average number of wet days per year.

DAYS90 = Number of days per year with the maximum temperature greater than 32 °C (90 °F).

DOWEL = Presence of dowels (1 if dowels are present, 0 if dowels are not present).

DAMAGE = n/N.

n = Actual number of applied cumulative ESAL's.

N = Allowable number of applied cumulative ESAL's.

Statistics:

N = 391.

$R^2$ = 0.50.

SEE = 0.035 in (0.89 mm).

Equation 14 is used to compute allowable ESAL's (N):

$$Log(N) = 0.785983 - 0.92991 * (1 + 0.40 * PERM * (1 - DOWEL)) * Log (DE) \quad (14)$$

where:

PERM = Base permeability (0 = not permeable, 1 = permeable).

DE = Differential energy density at a corner.

The DE at a corner is defined as the energy difference in the elastic subgrade deformation under the loaded slab (leave) and the unloaded slab (approach). The computation of DE involves completing a multi-step process in which maximum corner deflections are computed for loaded and unloaded conditions. The details of this calculation are presented later in this chapter (in the section describing the final joint faulting model developed under this study).

One important equation used in the computation of DE concerns the nondimensional aggregate interlock stiffness (AGG*) factor. When percent consolidation around dowels is not considered, AGG* is computed using equation 15.

$$AGG^* = (AGG/kL) = 2.3\,Exp(1 - 1.987 * JTSPACE / L + 3.48 * DOWELDIA^{3.56}) \quad (15)$$

where:

AGG* = Nondimensional aggregate interlock stiffness.
AGG = Aggregate load transfer stiffness, psi.
k = Dynamic modulus of subgrade reaction (dynamic k-value), psi/in.
L = Slab's radius of relative stiffness, in.
$= [(E_{PCC} * h_{PCC}^3) / (12 * (1 - \mu^2) * k)]^{0.25}$
$E_{PCC}$ = PCC modulus of elasticity, psi.
$h_{PCC}$ = Slab thickness, in.
$\mu$ = PCC Poisson's ratio (assumed to be equal to 0.15).
JTSPACE = Slab length (joint spacing), ft.
DOWELDIA = Dowel diameter, in.

**PAVESPEC 3.0 MODEL**

As part of development of PAVESPEC 3.0 model, the NCHRP 1-34 model was recalibrated using wider database. It resulted in the following model[16]:

$$FAULT = DAMAGE^{0.275} * [0.1741 - 0.0009911 * DAYS90 + 0.001082 * PRECIP] \quad (16)$$

where:

FAULT = Average transverse joint faulting per joint, in.
DAMAGE = n/N.
n = Actual number of applied cumulative ESAL's.
N = Allowable number of applied cumulative ESAL's.
DAYS90 = Number of days per year with the maximum temperature. greater than 32 °C (90 °F).
PRECIP = Average annual precipitation, in.

Statistics:

No. of data = 511.
$R^2$ = 56 percent.

SEE = 0.029 in (0.74 mm).

Equation 17 is used to compute allowable ESAL's (N):

$$Log(N) = 0.785983 - Log(EROD) - 0.92991 * (1 + 0.40 * PERM * (1 - DOWEL)) * Log (DE*(1 - 1.432*DOWELDIA + 0.513*DOWELDIA^2)) \quad (17)$$

where:

| | | |
|---|---|---|
| N | = | Allowable number of applied cumulative million ESAL's. |
| EROD | = | Base erodibility factor for the base (value between 0.5 and 7.5). |
| PERM | = | Base permeability. |
| | = | 0, if not permeable. |
| | = | 1, if permeable. |
| DOWEL | = | Presence of dowels (1 if dowels are present, 0 if dowels are not present). |
| DOWELDIA | = | Dowel diameter, in. (maximum allowed is 1.50 in) |
| DE | = | Differential energy density at a corner. |

As stated previously in this chapter, the DE at a corner is defined as the energy difference in the elastic base/subgrade deformation under the loaded slab (leave) and the unloaded slab (approach). One important equation used in the computation of DE is that for the nondimensional aggregate interlock stiffness (AGG*) factor. When percent consolidation around dowels is not considered, AGG* is computed using equation 18.

$$AGG^* = (AGG/kL) = 2.3 * Exp(-1.987 * JTSPACE / L + DOWELDIA^{2.2}) \quad (18)$$

where:

| | | |
|---|---|---|
| AGG* | = | Nondimensional aggregate interlock stiffness. |
| AGG | = | Aggregate load transfer stiffness, psi. |
| k | = | Dynamic modulus of subgrade reaction (dynamic k-value), psi/in. |
| L | = | Slab's radius of relative stiffness, in. |
| | = | $[(E_{PCC} * h_{PCC}^3) / (12 * (1 - \mu^2) * k)]^{0.25}$ |
| EPCC | = | PCC modulus of elasticity, psi. |
| $h_{PCC}$ | = | Slab thickness, in. |
| $\mu$ | = | PCC Poisson's ratio (assumed to be equal to 0.15). |
| JTSPACE | = | Slab length (joint spacing), ft. |
| DOWELDIA | = | Dowel diameter, in. (maximum allowed is 1.50 in). |

**Analysis of Existing JPCP Transverse Joint Faulting Models**

Factors Affecting Faulting

A review of recently developed JPCP faulting models identified a number of distinct relationships between faulting and traffic, age, and various climatic, site, and pavement design

variables. All of the models showed trends of faulting increasing rapidly and then slowly leveling off over time.

All the models predict that the presence of dowels is the most important design feature affecting joint faulting, and doweled JPCP with larger dowel bars have lower faulting. This is logical, since a larger dowel diameter reduces bearing stresses in concrete and increases the long-term effectiveness of dowels in controlling faulting.

Several of the models indicate that shoulder type has a significant effect on faulting. While the SHRP P-020 doweled faulting model calculates less faulting if a tied PCC shoulder is used, the more recent RPPR study showed that tied PCC shoulders do not have a significant effect in reducing faulting.[3, 13] This finding is attributed to the observation that the sections included in the RPPR database did not supply significant load transfer efficiency at the slab corner to reduce deflections and affect faulting. The RPPR study did, however, find that the presence of a widened lane significantly reduced faulting. [3]

The review of the recently developed transverse joint faulting models identified a number of variables that consistently have been found to have a significant influence on faulting. A summary of the significant variables used in past model development (for those models reviewed in this section) is provided in table 1. This collective list of variables (or variables related to these) will be considered in the transverse faulting model validation/development procedures conducted under this project.

Table 1. Summary of variables found to significantly affect JPCP transverse joint faulting.

| Variable | SHRP P-020 (1984)[13] | RPPR (1997)[3] | ACPA (1994)[8] | NAPCOM (1997)[6] | LTPP Data Analysis (1997)[7] | PaveSpec 3.0[16] |
|---|---|---|---|---|---|---|
| Age | X | X | | | | |
| 80-kN (18-kip) ESAL's | X | X | | | X | X |
| Axle load repetitions | | | X | X | | |
| Drainage type | X | | X | | | X |
| AASHTO drainage coefficient, $C_d$ | | X | | X | X | |
| PCC slab thickness | | X | X | X | X | X |
| PCC modulus of elasticity | | X | | X | X | X |
| Modulus of subgrade reaction (k-value) | X | X | X | X | X | X |
| Base type | | X | | X | X | X |
| Shoulder type | X | X | | X | X | X |
| Transverse joint spacing | X | X | X | X | X | X |
| Dowel diameter | X | X | | | X | X |

The review of the models also shows that the following parameters have been used successfully for faulting prediction:

- Cumulative differential energy parameter
- Base/subgrade erodibility index
- Free water indexes

These parameters are described below.

Differential Energy Concept

Several recent faulting models reviewed in this study directly relate faulting to the dissipation of energy of deformation to the slab support. This dissipated energy to the subgrade is assumed to be proportional to the energy of elastic deformation. The density of energy of elastic deformation can now be presented as the following:

$$E = 1/2\ w\ p \qquad (19)$$

where

E is the density of elastic deformation.
w is the slab's deflection profile.
p is the pressure at the slab-foundation interface.

When a Winkler subgrade model is used the subgrade pressure and slab deflection are related as follows:

$$p = k\ w \qquad (20)$$

where

p is the pressure at the slab-foundation interface.
k is modulus of subgrade reaction.
w is the slab's deflection profile.

Substitution of equation (20) into equation (19) leads to the following equation for the energy of subgrade deformation:

$$E = 1/2\ k\ w^2 \qquad (21)$$

where

E is the density of elastic deformation.
w is the slab's deflection profile.
k is modulus of subgrade reaction.

The concept of deformation energy has been used in many pavement research studies. Larralde developed a pumping model at Purdue to compute the pumped volume of materials as a function of the deformation energy imposed on the pavement by traffic loading.[17] Other researchers have used deformation energy in a similar scenario.[18,19] The Purdue model had the following form:

$$E_{tot} = \Sigma\ k_i A_i w_i^2 \qquad (22)$$

where

$E_{tot}$ is the density of elastic deformation.
$w_i$ is the slab's deflection profile at node i.

$k_i$ is modulus of subgrade reaction at node i.
$A_i$ is threshold index for node i.
=1, if deflection over 20 mils.
=0, if deflection is less than 20 mils.

The concept of the differential energy of subgrade deformation (DE) at the corner was developed in recent studies.[5,6,7] The differential energy is defined as the energy difference in the elastic subgrade deformation under the loaded slab (leave) and unloaded slab (approach):

$$DE = E_L - E_{UL} = 1/2\ k\ w_L^2 - 1/2\ k\ w_{UL}^2 \qquad (23)$$

where
DE is differential energy of subgrade deformation.
$E_L$ is energy of subgrade deformation under the loaded slab corner.
$E_{UL}$ is energy of subgrade deformation under the unloaded slab corner.
$w_L$ is the corner deflection under the loaded slab.
$w_{UL}$ is the corner deflection under the unload slab.
k is modulus of subgrade reaction.

Equation 23 may be re-written in the following form:

$$DE = k/2\ (w_L + w_{UL})(\ w_L - w_{UL}) \qquad (24)$$

where
DE is differential energy of subgrade deformation.
$w_L$ is the corner deflection under the loaded slab.
$w_{UL}$ is the corner deflection under the unload slab.
k is modulus of subgrade reaction.

The term $(w_L + w_{UL})$ is equal to the free corner deflection. It represents the total flexibility of the slab. The higher the slab's flexibility, the greater the differential energy and the joint faulting potential.

The term $(w_L - w_{UL})$ is the differential corner deflection between the loaded slab and unload slab corner. It represents the relative movement between the loaded and unloaded slabs. The greater the difference, the higher the joint faulting will be. Without any differential deflections at the corner, there will not be any faulting, as seen at the AASHO Road Test. The differential corner deflection depends on the free corner deflection and the deflection load transfer efficiency, LTE. If the latter is defined as

$$LTE = \frac{w_{UL}}{w_L} 100\% \qquad (25)$$

then equation 3 can be re-written in the following form:

$$DE = \frac{k}{2}\left(w_L + w_{UL}\right)\frac{1-\frac{LTE}{100}}{1+\frac{LTE}{100}} \quad (26)$$

One can see that joint load transfer efficiency has a major effect on the differential energy of subgrade deformation.

Erodibility

An erodible base is a key factor that must be present for pumping and faulting to occur. Determining base/subbase erodibility (usually a direct input for faulting predicting models) is therefore very important for predicting faulting accurately. Material erodibility can only be characterized accurately if the causes of erosion are understood.

Erodibility is a change in surface property of a material when subjected to friction, shearing, and wear of hydrodynamic origin. This results in the loss of materials on the surface and consequently in modifications to the texture and dimensions of the material due to the formation of cavities. The theory of hydrodynamics and pumping (motions of water, expulsion rate, and critical erosion rate of paving materials) can be used to explain this phenomenon.[20, 21] Surface erosion of a base/subbase layer is caused by hydraulic and mechanical action under traffic loading, which abrades the interface of the two layers.[18] This results in the loosening of compacted material at the surface layer/base or subbase interface. As more and more traffic loads are applied to the pavement, this loosening effect penetrates deeper into the pavement base/subbase layer. The loosened material is distributed horizontally or vertically as the material is moved from an area of high pressure to one of lower pressure.[18] The method by which a base/subbase material will be eroded is highly dependent on material type, (asphalt-, cement-, lime-treated or non-treated material). Asphalt-treated materials with adequate binder content and durable aggregate material are normally fairly insensitive to water under pressure. Their long-term erosion potential depends on the potential for degradation of aggregates, stripping of the binder, and defects in construction such as inadequate compaction. Cement-treated materials with a high cement content are mostly insensitive to water under high pressure. Their sensitivity to moisture depends on the gradation of the aggregates. Fine-grained cement mixtures tend to erode when exposed to moisture, while the coarser materials tend to crack (and, in severe cases, crush) if the parent rock is highly weathered.

For granular materials, gradation and density govern erodibility. Densely compacted materials are less permeable and are less likely to contain infiltrated water, which decreases the possibility of shear failure or internal erosion when subjected to high pore water pressure. Granular materials with a lot of fines are also more likely to erode when exposed to moisture and high pore water pressure.

Since the 1940s, several attempts have been made characterize material erodibility using specifications developed by highway research agencies such as the Permanent International Association of Road Congresses (PIARC) or through the development of various forms of

erosion testing devices. Some of the data used to characterize material erodibility was obtained through coring existing base/subbase layers.[21]

Recent research has focused on developing more comprehensive tests that are based on the mechanisms of erosion. The tests currently being used to assess the erodibility of base/subbase materials include:[18,22,23,24]

- Rotational shear device for cohesive or stabilized materials.
- Jetting test.
- Linear and rotational brush tests.
- Erosion test (South Africa).

None of these tests have been certified by testing agencies such ASTM or AASHTO. However, brief descriptions of the tests are presented in the following sections to inform readers on future approaches to erosion modeling and assessment. It must be noted that some of the erosion tests presented were developed to evaluate the erosion of not only pavement materials but also materials for channels, earth dams, and soil slopes.[19] Results of these tests are typically in the form of an erosion index that can be directly incorporated into the faulting model.

*Rotational Shear Device*

This test is performed by placing a sample test specimen in a relatively stationary position within a rotating cylinder filled with water. A load cell connected through an end plate is used to measure the resultant torque on the specimen introduced by the rotating water. The amount of erosion is measured by calculating the difference in the weight of the original specimen and the eroded material after testing.[19] Typical rotational shear test results indicate that the amount of erosion increases rapidly after the "critical shear stress" of the material under consideration is exceeded. Normally, the rate of increase in erosion is exponential.

This device has been used successfully by several researchers in the investigation of the erosion of materials ranging from clays to treated materials. This is possible because the uniform shear forces generated by the rotating water can be adjusted easily by changing the speed of the water, making the test suitable for a wide range of base/subbase materials with different critical shear stresses.[19] Furthermore, it is the only test in which the shear stresses that cause surface erosion can be measured accurately. The main drawback of this test is that non-cohesive materials cannot be tested.

*Jetting Device*

The jetting erosion test device is a modification of the rotational test device that can evaluate non-cohesive soils.[19] The device consists of a jet placed at an angle of approximately 20 degrees to the upper surface of the test specimen. The jet applies water at varying pressures to the surface of the test specimen. The test can be performed on samples fully or partially submerged or not submerged in water. The shear stress on the surface of the specimen is

calculated by dividing the force applied at the surface by the contact area. A uniform distribution over the area may then be assumed even though the shear stresses on the specimen surface are not uniform.

*Brush Test*

Several brush test devices are used throughout the world, including the linear and rotational brush tests developed by Phu et al.[23] The test is conducted by applying a standard brush under a standard load or pressure to the test specimen. For the linear brush test, applying different weights to the brush may vary the pressure. For the rotational brush test, a standard weight of 1 kg is applied to the brush. Erosion is quantified by the weight loss of the test specimen after testing is complete and is called the brush erosion.[24]

Weight loss is standardized by adopting a unit measure of weight loss called the erodibility index (IE). The IE is defined as the ratio of the weight loss from the test specimen to the weight loss of a reference stabilized granular material. The reference material is a granular material with a gradation (Talbot) n-value of 0.5, treated with 3.5 percent cement, and compacted with an energy of 1613 $kJ/m^3$.[24]

Erosion of 0.026 kg/min is regarded as one unit of IE, and the weight losses of all materials evaluated by the rotational brush test are normalized to the erosion of the reference material. The test method is practical and forms the basis for comparing the erodibility characteristics of different materials.[24]

*South African Erosion Test*

This test consists of a loaded wheel running on a linear track along the topside of the erosion specimen, which is installed in a sealed container and encased in gypsum.[22] The test specimen is placed in a large container sealed at the top with a flexible neoprene membrane. Three friction pads are secured underneath the membrane and are put in direct contact with the test specimen to simulate the aggregate-to-aggregate contact stresses expected at the base/subbase surface layer interface when traffic loads are applied to the pavement. A cyclic wheel load is run on the friction pad/test specimen combination to simulate traffic loading.[22]

The test is performed on a soaked test specimen under water. (The water provides the “vehicle” for removing the free fines from the test specimen during testing.) The friction pad and wheel load provide the necessary stress, which produces free fines in the test specimen as observed in the field.[22] The cyclical normal contact stress provided by the loaded wheel varies from an initial value of approximately 2.2 MPa to approximately 1.0 MPa as the average erosion depth in the test specimen increases from 0 to 10 mm. The reason for this decrease in contact stress is that during testing (especially if the material is relatively erodible) the actual contact area increases as a result of erosion under constant loading. If the specimen is nonerodible (no increases in eroded area), the cyclic stress is constant (approximately 2.2 MPa). This stress approximates the unconfined compressive strength (UCS) of most lightly cementitious materials and is therefore appropriate for producing free fines on the surface of the specimens.[22]

A standardized scale called the Erosion Index (L) is used to quantify erodibility. (Note that this scale has no relationship to IE, obtained from the brush tests.) The Erosion Index is defined as the average depth of erosion (in millimeters) after the application of 5000 wheel load repetitions in the erosion test device. For erodible materials, the test may be terminated before 5000 load repetitions and the depth of erosion at 5000 load repetitions is determined by extrapolation. This ensures that even the most erodible materials can be tested.[22]

The faulting model presented above use erodibility index developed based on the PIARC specifications which groups base/subbase erosion potential into five classes as summarized in Table 2.[21, 35] This was modified in the recently completed performance-related specification (PAVESPEC) study.[16] This modification replaced stabilizer content (asphalt or portland cement) of the base/subbase materials with long-term compressive strength (strength measured at a time much later than 28 days). Recent studies have shown that compressive strength is also a reliable indicator of erodibility, and since it is more readily available than stabilizer content in most databases, it was used to replace stabilizer content.[34] Table 3 presents these recommendations. Hoerner et al. also recommended numeric erodibility factor associated with each PIARC erodibility class (see Table 4).

In this study, the original PIARC specifications were further modified to include permeable materials (treated or untreated granular material with permeability > 300 ft/day) as a base/subbase material type. In table 5, the erodibility resistance ratio is on the order of about five between each class (i.e., class 1 materials are five times more erosion resistant than class 2 and so on). This erodibility levels were used as an input for the 2002 Design Guide faulting model.

Table 2. PIARC recommendations for erosion potential of base/subbase material (adapted after PIARC 1987).

| Class | Description |
|---|---|
| A—Extremely Erosion Resistant | Class A materials are extremely resistant to erosion. The typical material of this category is lean concrete with at least 7 to 8 percent cement (or 6 percent with special addition of fines) or bituminous concrete with a bitumen content of at least 6 percent |
| B—Erosion Resistant | Class B materials are five times more erodible (on average) than class A materials, but they still offer good guarantees of erosion resistance because they are far from the threshold at which erodibility increases exponentially. The typical material of this category is a granular material cement-treated in the plant and containing 5 percent cement |
| C—Erosion Resistant | Class C materials are five times more erodible (on average) than those in class B, and they are close to the threshold under which erodibility increases very rapidly in inverse proportion to the amount of binder. The typical material of this category is a granular material cement-treated in the plant and containing 3.5 percent cement, or a bitumen-treated granular material with 3 percent bitumen |
| D—Fairly Erodible | Class D materials are five times more erodible (on average) than those of class C. Their low binder content makes their erosion resistance properties highly dependent on construction conditions and the homogeneity of the material. The typical material of this category is a granular material treated in place with 2.5 percent cement. Also falling within this category are fine soils treated in place, such as cement-treated silt-lime and cement-treated sand. By extension, clean, well-graded, good quality granular materials would also fall in this category |
| E—Very Erodible | Class E materials are over five times more erodible (on average) than those of class D. Class E materials are untreated or very poorly treated mixes. The typical material of this category is an unprocessed treated material rich in fine elements, and especially untreated silt |

Table 3. Supplemental recommendations for erosion potential of CTB (based on long-term compressive strength).

| Base Erodibility Class | Material Description |
|---|---|
| A | Cement treated granular material with long-term compressive strength > 2,500 psi. |
| B | Cement treated granular material with long-term compressive strength <= 2,500 and > 2,000 psi. |
| C | Cement treated granular material with long-term compressive strength <= 2,000 and > 1000 psi. |
| D | Cement treated granular material with long-term compressive strength <= 1000 psi. |

Table 4. Recommendations for assigning erodibility factor based on PIARC erodibility class.

| PIARC Erodibility Class | Recommended Ranges for Base Erodibility Factor |
|---|---|
| A | 0.5–1.5 |
| B | 1.5–2.5 |
| C | 2.5–3.5 |
| D | 3.5–4.5 |
| E | 4.5–5.5 |
| No base | 5.5–7.5 |

Characterizing Free Water within the Pavement System

Moisture within a pavement system, which is typically a function of time and space, is a key factor for accurately estimating the potential for faulting damage. The general methods characterizing the moisture regime within a pavement are (1) using climate-related data such as precipitation and wet days or (2) using empirically derived models that describe the cyclic behavior of moistures based on factors such as precipitation, material type and gradation, soil suction, and water table that are known to significantly influence it. A summary of the climate-related variables used to characterize moisture within the pavement system is presented in table 6. Also, a summary of the typical empirical methods used to describe moisture with the pavement system and incorporated in the EICM software is presented in the following sections.

Table 5. 2002 Design Guide recommendations for assessing erosion potential of base material.

| Erodibility Class | Material Description and Testing |
|---|---|
| 1 | (a) Lean concrete with approximately 8 percent cement; or with long-term compressive strength > 2,500 psi (>2,000 psi at 28-days) and a granular subbase layer or a stabilized soil layer, or a geotextile fabric is placed between the treated base and subgrade, otherwise class 2.<br>(b) Hot mixed asphalt concrete with 6 percent asphalt cement that passes appropriate stripping tests and aggregate tests and a granular subbase layer or a stabilized soil layer (otherwise class 2).<br>(c) Permeable drainage layer (asphalt treated aggregate or cement treated aggregate and with an appropriate granular or geotextile separation layer placed between the treated permeable base and subgrade. |
| 2 | (a) Cement treated granular material with 5 percent cement manufactured in plant, or long-term compressive strength 2,000 to 2,500 psi (1,500 to 2,000 psi at 28-days) and a granular subbase layer or a stabilized soil layer, or a geotextile fabric is placed between the treated base and subgrade; otherwise class 3.<br>(b) Asphalt treated granular material with 4 percent asphalt cement that passes appropriate stripping test and a granular subbase layer or a treated soil layer or a geotextile fabric is placed between the treated base and subgrade; otherwise class 3. |
| 3 | (a) Cement-treated granular material with 3.5 percent cement manufactured in plant, or with long-term compressive strength 1,000 to 2,000 psi (750 psi to 1,500 at 28-days).<br>(b) Asphalt treated granular material with 3 percent asphalt cement that passes appropriate stripping test. |
| 4 | Unbound crushed granular material having dense gradation and high quality aggregates. |
| 5 | Untreated soils (PCC slab placed on prepared/compacted subgrade) |

Table 6. Climate-related variables used in describing within pavement moisture regime.

| Variable | Significance |
|---|---|
| Wet days | An indicator of the number of days in a given period (e.g., year) with a minimum amount of precipitation (e.g., > 0.1 in) |
| Precipitation | Average daily, monthly, or annual precipitation |
| Freezing index | Average daily, monthly, or annual mean freezing index |
| Freeze-thaw cycles | Number of air or pavement free-thaw cycles within a given time period (e.g., a year) |

## 2002 DESIGN GUIDE FAULTING MODEL

### Approach

As discussed earlier, there are four main components of an ideal M-E faulting model: damage due to axle load applications, inadequate load transfer, erodibility of the underlying materials, and the presence of free water. It is obvious that models for predicting joint faulting can be categorized as mechanistic-empirical or empirical, depending on how these components are formulated. Based on the current state of the art, the following can be concluded:

- There are currently no mechanistic procedures for predicting of the effect of the moisture state of the underlying materials on faulting. However, indirectly, this effect can be accounted for by including seasonal variation of subgrade stiffness into prediction of structural responses.
- There are currently no mechanistic procedures for determining the erodibility of the underlying materials. However, several material-related variables have been identified as affecting erodibility (e.g., base, subbase, and subgrade type, gradation, percent fines, and treatment or stabilizer type and amount).
- The stresses, deflections, and work or power to which the underlying pavement materials are subjected have been satisfactorily modeled using current technology based on mechanistic principles. Two main approaches have been identified and discussed.

It is obvious that it is not possible to incorporate a totally mechanistic model in the 2002 Design Guide because it is not possible to develop a totally mechanistic model using current technology. However, existing M-E models are available that have been developed and calibrated using an incremental damage approach that utilizes mechanistic and empirical damage clusters.

The PAVESPEC 3.0 faulting model was found to be the most advanced models among the models evaluated in this study and was selected as a basis for faulting model adaptation. Nevertheless, the model has significant limitations:

- The model uses ESALs, not axle spectrum distributions, to characterize traffic.
- The model uses “average” parameters for load transfer characterization, instead of an incremental damage approach.
- The model neglects seasonal and environmental effects on faulting development. Incorporation of the EICM into the 2002 Design Guide permits more realistic modeling the effects of such factors as seasonal variation in subgrade k-value, PCC slab warping, and curling.

To address these limitations, the PAVESPEC 3.0 model was further enhanced and calibrated. The 2002 Design Guide faulting model uses incremental damage accumulation approach for faulting development. Each month of the design period mean joint faulting increases by a certain amount, which depends on the following parameters:

- Damage increment expressed through differential energy of subgrade deformation, which in turn depends on the level of traffic and magnitude of corner deflections of loaded and unloaded slabs.
- Potential erodibility of the underlying layers.
- Current faulting level: rate of faulting development is higher when faulting laver is lower.

The main difference of the 2002 Design Guide faulting model from the PAVESPEC 3.0 is that the 2002 model accounts for incremental deterioration of transverse joints. Joint deterioration reduces joint load transfer efficiency, increases the magnitude of differential PCC slab deflection across the joint, and as a result, increases the magnitude of differential energy of subgrade deformation for the same traffic level and faulting development. Since this concept has a paramount importance on faulting prediction, it is described in detail below.

**Joint Deterioration Model**

When a traffic load is applied near a joint in a PCC pavement, both loaded and unloaded slabs deflect because a portion of the load applied to the loaded slab is transferred to the unloaded slab. As a result, deflections in the loaded slab may be significantly less than if, instead of a joint with another slab, there was a free edge. The magnitude of reduction in deflections by a joint compared to a free edge depends on the joint's LTE.

Traditionally, LTE at the joint is determined based on the ratio of the maximum deflection at the joint of the loaded slab and the deflection of the unloaded slab measured right across the joint from the maximum deflection using equation 25.

If a joint exhibits poor ability to transfer load, then the deflection of the unloaded slab is much less than the deflection at the joint of the loaded slab and the LTE has values close to 0. If a joint's load transfer ability is very good, then the deflections at the both sides of the joint are equal and the LTE has a value close to 100 percent.

Load transfer between the slabs occurs through aggregate particles of the fractured surface below the saw cut at a joint, through steel dowels (if they exist), and through the base and subgrade. LTE may vary throughout the day and year due to variation in PCC temperature. When temperature decreases, a joint opens wider, which decreases contact between two slabs and may decrease LTE, especially if no dowels exist. Also, PCC slab curling may change the contact between the slab and the underlying layer and affect measured load-induced deflections.

Mechanistic modeling of the load transfer mechanism is a complex problem. Frieberg was one of the first researchers who attempted to tackle this problem.[28] The introduction of a finite element method for analysis of JCP gave a significant boost to understanding load transfer mechanisms.[29] However, although many comprehensive finite element models have been developed, this work on the development of a comprehensive, practical, and reliable model for joints of rigid pavements is far from complete.[30,31,32,33]

The 2002 Design Guide joint model characterizes joint stiffness through deflection LTE measured for a flat slab conditions (i.e., assuming that no significant separation between the

foundation and the PCC slab exists). Testing early in the morning (from about 6 to 8 a.m.) usually resembles these conditions closely.

The joints are modeled using vertical shear spring finite elements. The equivalent stiffness of the spring element, AGG-factor, is selected to provide appropriate deflection LTE for flat slab (no curling) conditions. For transverse joints, the total deflection LTE includes the contribution of three major mechanisms of load transfer:

- Load transfer by PCC aggregates.
- Load transfer by joint dowels (if applicable).
- Joint transfer by the base/subgrade.

The combined LTE can be determined from the following equation:

$$LTE_{joint} = 100\left(1-(1-LTE_{dowel}/100)(1-LTE_{agg}/100)(1-LTE_{base}/100)\right) \quad (27)$$

where,

$LTE_{joint}$ = Total joint LTE, percent.
$LTE_{dowel}$ = Joint LTE if dowels are the only mechanism of load transfer, percent.
$LTE_{base}$ = Joint LTE if the base is the only mechanism of load transfer, percent.
$LTE_{agg}$ = Joint LTE if aggregate interlock is the only mechanism of load transfer, percent.

Modeling of each of these LTE mechanisms is presented below.

Aggregate Interlock LTE

Ioannides and Korovesis identified the following nondimensional parameters governing aggregate joint behavior:[25]

$$J_{agg} = \frac{AGG}{k\,\ell} \quad (28)$$

where

$J_{AGG}$ = Nondimensional stiffnesses of aggregate joint.
AGG = Shear stiffness of a unit length of an aggregate interlock.
$\ell$ = PCC slab radius of relative stiffness.
k = Coefficient of subgrade reaction (k-value).

Using the finite element program ILLI-SLAB, Ioannides and Korovesis also identified a unique relationship between these parameters and LTE (see figure 1). The following assumptions were made in derivation of these relationships:

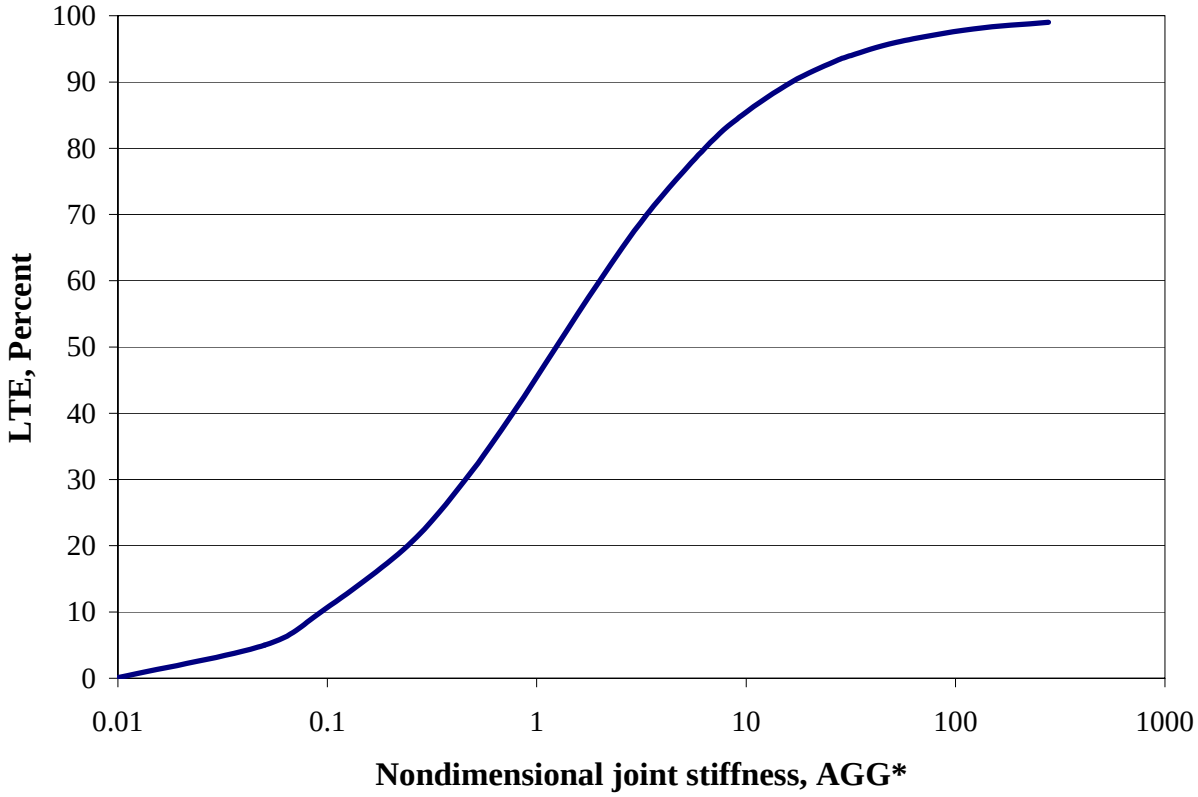


Figure 1. LTE versus nondimensional joint stiffness.

- Prior to loading, PCC slabs are flat and in full contact with the foundation.
- A PCC joint propagates through the base layer (if present). No load transfer occurs through the base layer.
- The subgrade is modeled as a Winkler foundation, which assumes no load transfer through the subgrade.
- The PCC joint has uniform LTE across its width. The entire load transfer in nondoweled joints occurs through aggregate interlock.

As stated above, it was assumed in this study that each load transfer mechanism acts independently from others so these assumptions Ioannides and Korovesis assumptions do not create any limitations.

The 2002 faulting prediction model adopted Zollinger et al. aggregate interlock model.[27] This model states that the nondimensional stiffness of an aggregate joint is a function of load shear capacity, S.

$$Log(J_{AGG}) = -3.19626 + 16.09737 * e^{-e^{-\left(\frac{S-e}{f}\right)}} \quad (29)$$

where,

$J_{AGG}$ = $(Agg/kl)_c$ = Joint stiffness on the transverse joint for current increment.

e = 0.35.
f = 0.38.
S = Joint shear capacity.

The joint shear capacity is depends on joint width and past damage and is defined as follows:

$$S = 0.05*h_{PCC*}e^{-0.028jw} - \Delta s_{tot} \quad (30)$$

where,

$S$ = Dimensionless aggregate joint shear capacity.
jw = Joint opening, mils (0.001 in).
h = PCC slab thickness, in
$\Delta s_{tot}$ = Cumulative loss of sheer capacity at the beginning of the current month.

In 2002 Design faulting modes, joint width is calculated for each month based on PCC temperature of set, PCC shrinkage, and PCC mean nighttime monthly temperature:

$$jw = Max(12000 * STSpace * \beta * (\alpha_{PCC} * (T_{constr} - T_{mean}) + \varepsilon_{sh,mean}),0) \quad (31)$$

where,

jw = Joint opening, mils (0.001 in).
$\varepsilon_{sh,mean}$ = PCC slab mean shrinkage strain.
$\alpha_{PCC}$ = PCC coefficient of thermal expansion, in/in/$^0$F.
JTSpace = Joint spacing, ft.
$\beta$ = Joint open/close coefficient assumed equal to 0.85 for a stabilized base and 0.65 for a unbound granular base.
$T_{mean}$ = Mean monthly nighttime mid depth temperature, $^0$F.
$T_{constr}$ = PCC temperature at set, $^0$F.

Loss of shear capacity is also computed on a monthly basis. Each axle load application contributes toward loss of shear. The cumulative loss of shear at the end of the month (i.e. in the beginning of the next design month) is determined as follows:

$$\Delta s_{tot}^{end} = \Delta s_{tot}^{b} - \sum_i n_i \Delta s_i \quad (32)$$

where:

$\Delta s_{tot}^{b}$ is cumulative loss of sheer capacity at the end of the current month equal to sum of loss of shear capacity form every axle load application.
$n_i$ is the number of application of axle load i.
$\Delta s_i$ is loss of capacity shear due to single application of an axle load i defined as follows:

$$\Delta s_i = \begin{cases} 0 & if \quad jw < 0.001\, h_{PCC} \\ \dfrac{0.005*10^{-6}}{1.0+(jw\ /\ h_{PCC})^{-5.7}}\left(\dfrac{\tau_{i,}}{\tau_{ref}}\right) & if \quad 0.001 < jw < 3.8\, h_{PCC} \\ \dfrac{0.068*10^{-6}}{1.0+6.0*(jw\ /\ h_{PCC}-3)^{-1.98}}\left(\dfrac{\tau_{i,}}{\tau_{ref}}\right) & if \quad jw > 3.8\, h_{PCC} \end{cases} \qquad (33)$$

where

$\Delta s_i$ = Loss of shear capacity from a single repetition of an axle load of group i

$h_{PCC}$ = PCC slab thickness, in.

jw = Joint opening, mils (0.001 in).

$\tau_i$ = Shear stress on the transverse joint surface from the response model for the load group i.

$\tau_{ref}$ = Reference shear stress derived from the PCA test results.

Figure 2 presents an example of predicted aggregate interlock component of joint LTE over the pavement design life. One can observe that two major trends in aggregate interlock LTE variation:

- Seasonal variability
- Reduction with time

Seasonal variation comes from change in joint opening due to seasonal change in mean PCC temperature. LTE reduction with time comes from loss of shear capacity and increase in joint opening due to shrinkage.

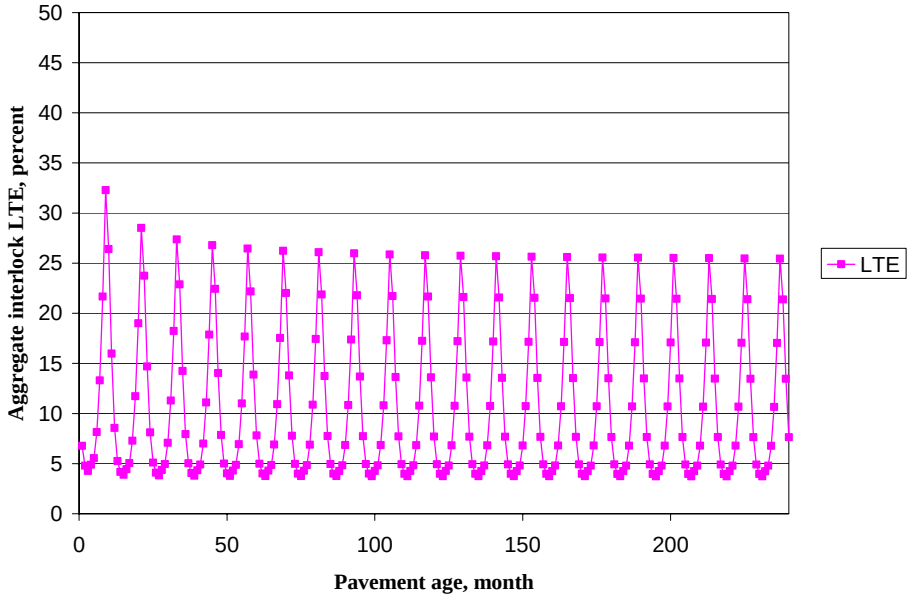


Figure 2. Example of predicted AGG interlock LTE (flat slab conditions).

Doweled Joint Load Transfer

Analysis of every faulting model described above as well as the results of several other major studies agrees that presence of dowels of an appropriate diameter significantly reduces faulting.[36] Several mechanistic-empirical models indicated that presence of dowels increase long term LTE.[6,15,16] Ioannides and Korovesis identified the following nondimensional parameters governing aggregate joint behavior:[25,26]

$$J_D = \frac{D}{DowelSpace\, k\, \ell} \quad (34)$$

where

$J_D$ = Dimensional stiffnesses of doweled joints.
D = A shear stiffness of a single dowel (including dowel-PCC interaction).
$\ell$ = PCC slab radius of relative stiffness,
k = Subgrade k-value,
DowelSpace = dowel spacing.

The same unique relationship between the nondimensional aggregate interlock stiffness and LTE identified by Ioannides and Korovesis is also valid for the nondimensional dowel joint stiffness if the following assumptions are satisfied:

- Prior to loading, PCC slabs are flat and in full contact with the foundation.
- A PCC joint propagates through the base layer (if present). No load transfer occurs through the base layer.
- The subgrade is modeled as a Winkler foundation, which assumes no load transfer through the subgrade.
- The PCC joint has uniform LTE across its width. The entire load transfer in doweled joints occurs through dowels,

Since this study assumes that each load transfer mechanism acts independently from others, these assumptions do not create any limitations.

The 2002 faulting prediction model adopted the following model for nondimensional dowel joint stiffness:

$$J_d = J^*_d + (J_0 - J^*_d)\exp(-DAM_{dowels}) \quad (35)$$

where:

$J_d$ = Nondimensional dowel stiffness.
$J_0$ = Initial nondimensional dowel stiffness.
$J^*_d$ = Critical nondimensional dowel stiffness.

$DAM_{dowels}$ = Damage accumulated by a doweled joints due to past traffic.

The initial and long-term nondimensional doweled stiffnesses depend on the ration of the area of dowel cross-section to dowel to PCC thickness and are defined in a following way:

$$J_0 = \frac{152.8 A_d}{h_{PCC}} \tag{36}$$

$$J^*_d = \begin{cases} 118, & if \ \frac{A_d}{h_{PCC}} > 0.656 \\ 210.0845 \frac{A_d}{h_{PCC}} - 19.8, & if \ 0.009615 \le \frac{A_d}{h_{PCC}} \le 0.656 \\ 0.4, & if \ \frac{A_d}{h_{PCC}} < 0.009615 \end{cases} \tag{37}$$

where:

$J_0$ = Initial nondimensional dowel stiffness.
$J^*_d$ = Critical nondimensional dowel stiffness.
$h_{PCC}$ = PCC slab thickness.
$A_d$ = Area of dowel cross-section:

$$A_d = \frac{\pi d^2}{4} \tag{38}$$

where
d = Dowel diameter.

Dowel joint damage accumulated for the current month is determined from the following equation:

$$\Delta DOWDAM_{tot} = \sum_{j=1}^{N} C_8 * F_j \frac{n_j}{d f_c^*} \tag{39}$$

where

$\Delta DOWDAM_{tot}$ = Cumulative dowel damage for the current month.
$n_i$ = umber of axle load applications for current increment and load group *j*.
N = Number of load categories.

$f_c^*$ = PCC compressive stress estimated.
$C_8$ = Calibration constant.
$F_j$ = Effective dowel shear force induced by axle loading of load category j.

$$F_j = J_d * \left(\delta_{L,j} - \delta_{U,j}\right) * DowelSpace \quad (40)$$

where

$F_j$ = Dowel shear force induced by axle loading load category j.

$J_d$ = Joint stiffness on the doweled joint computed for the time increment

$\delta_{L,j}$ = Corner deflections of the loaded slab caused by axle loading of type A and load category i.

$\delta_{U,j}$ = Corner deflections of the unloaded slab caused by axle loading of load category i.

j = Parameter defining axle weight

DowelSpace = Space between adjacent dowels in the wheel path, in.

Base Load Transfer

Even if no dowels present in the base and joints are open so widely than no aggregate interlock exists, joint load transfer efficiency is not equal to zero. A certain portion of load is transferred from the loaded to unloaded slab through the base, subbase, and subgrade pavement layers. The 2002 Design Guide procedure accounts for this effect by assigning a percentage of load transfer efficiency of the base layer, $LTE_{base}$, depending on the base layer type. In most cases, the value of the load transfer efficiency can be determined from table 7 (and it is assumed in the Design Guide software). As can be observed from table 7, the 2002 Design Guide procedure assumes that a properly designed stabilized layer provides better load transfer efficiency than a granular base. However, even the load transfer efficiency of a lean concrete base is not extremely high.

Table 7. Assumed effective base LTE for different base types.

| **Base Type** | $\boldsymbol{LTE_{Base}}$ |
|---|---|
| Aggregate base | 20% |
| ATB or CTB base | 30% |
| LCB base | 40% |

There is a very important exception from this rule. It is recognized that if the pavement system is frozen, then even the LTE of undoweled joints increases. Considering that in the cold temperature the joints are open the most (i.e., the aggregate portion of the LTE is smaller than in the warm weather), this increase should come from the increase of the LTE of the base layer. To account for this effect, the 2002 Design Guide software calculates the mean monthly mid-depth PCC temperatures. If for a given month this temperature is less than 32 °F, then $LTE_{base}$ is set equal to 90 percent for that month.

**2002 Design Guide Faulting Model – General Overview**

The mean transverse joint faulting is predicted using an incremental approach, as illustrated in figure 3. A faulting increment is determined each month, and the current faulting level affects the magnitude of increment. The faulting at each month is determined as a sum of faulting increments from all previous months in the pavement life since the traffic opening using the following model:

$$Fault_m = \sum_{i=1}^{m} \Delta Fault_i \tag{41}$$

$$\Delta Fault_i = C_{34} * (FAULTMAX_{i-1} - Fault_{i-1})^2 * DE_i \tag{42}$$

$$FAULTMAX_i = FAULTMAX_0 + C_7 * \sum_{j=1}^{m} DE_j * Log(1 + C_5 * 5.0^{EROD})^{C_6} \tag{43}$$

$$FAULTMAX_0 = C_{12} * \delta_{curling} * \left[ Log(1 + C_5 * 5.0^{EROD}) * Log(\frac{P_{200} * WetDays}{p_s}) \right]^{C_6} \tag{44}$$

where,

| | | |
|---|---|---|
| $Fault_m$ | = | Mean joint faulting at the end of month m, in. |
| $\Delta Fault_i$ | = | Incremental change (monthly) in mean transverse joint faulting during month *i*, in. |
| $FAULTMAX_i$ | = | Maximum mean transverse joint faulting for month *i*, in. |
| $FAULTMAX_0$ | = | Initial maximum mean transverse joint faulting, in. |
| $EROD$ | = | Base/subbase erodibility factor. |
| $DE_i$ | = | Differential deformation energy accumulated during month *i*. |
| $EROD$ | = | Base/subbase erodibility factor. |
| $\delta_{curling}$ | = | Maximum mean monthly slab corner upward deflection PCC due to temperature curling and moisture warping. |
| $P_S$ | = | Overburden on subgrade, lb. |
| $P_{200}$ | = | Percent subgrade material passing #200 sieve. |
| $WetDays$ | = | Average annual number of wet days (greater than 0.1 in rainfall). |

$$C_{12} = C_1 + C_2 * FR^{0.25} \tag{45}$$

$$C_{34} = C_3 + C_4 * FR^{0.25} \tag{46}$$

$FR$ = Base freezing index defined as percentage of time the top base temperature is below freezing (32 °F) temperature.

$C_1$ through $C_8$ are calibration constants.

The functional form of the model reflects the hypothesis that faulting potential depends of amount of the PCC slab curling, base erodibility, and the presence of fines and free water in the subgrade. Faulting potential decreases with an increase of overburden pressure on the subgrade.

The rate of faulting development depends of the faulting level and decreases when faulting increases until it stabilizes to a certain level.

Prediction of transverse joint faulting in the 2002 Design Procedure involves the following steps:

1. Tabulate input data – summarize all inputs needed for predicting JPCP transverse joint faulting.
2. Process traffic data – the processed traffic data needs to be further processed to determine equivalent number of single, tandem, and tridem axles produced by each passing of tandem, tridem, and quad axles.
3. Process pavement temperature profile data – the hourly pavement temperature profiles generated using EICM (nonlinear distribution) need to be converted to effective nighttime differences by calendar month.
4. Process monthly relative humidity data – the effects of seasonal changes in moisture conditions on differential shrinkage is considered in terms of monthly deviations in slab warping, expressed in terms equivalent temperature differential.
5. Calculate initial maximum faulting.
6. Evaluate joint LTE.
7. Calculate current maximum faulting.
8. Determine critical pavement responses for the increment.
9. Evaluate loss of shear capacity and dowel damage.
10. Calculate faulting increment.
11. Calculate cumulative faulting.

The incremental design procedure requires thousands of deflection calculations to compute damage monthly (for the different loads, joint stiffnesses, and equivalent temperature differences) over a design period of many years. These computations would take hours (if not days) using existing finite element programs. Thus, it is not practical to include a finite element program with the design guide software at this time. To reduce computer time to a practical level, neural networks (NNs) have been developed to accurately compute critical corner deflections virtually instantaneously. This makes it possible to conduct detailed incremental analysis (month by month) to sum damage over time in a realistic way. The neural networks reproduce the same deflections very accurately given the set of required inputs. Neural networks were developed separately for single, tandem, and tridem axles.

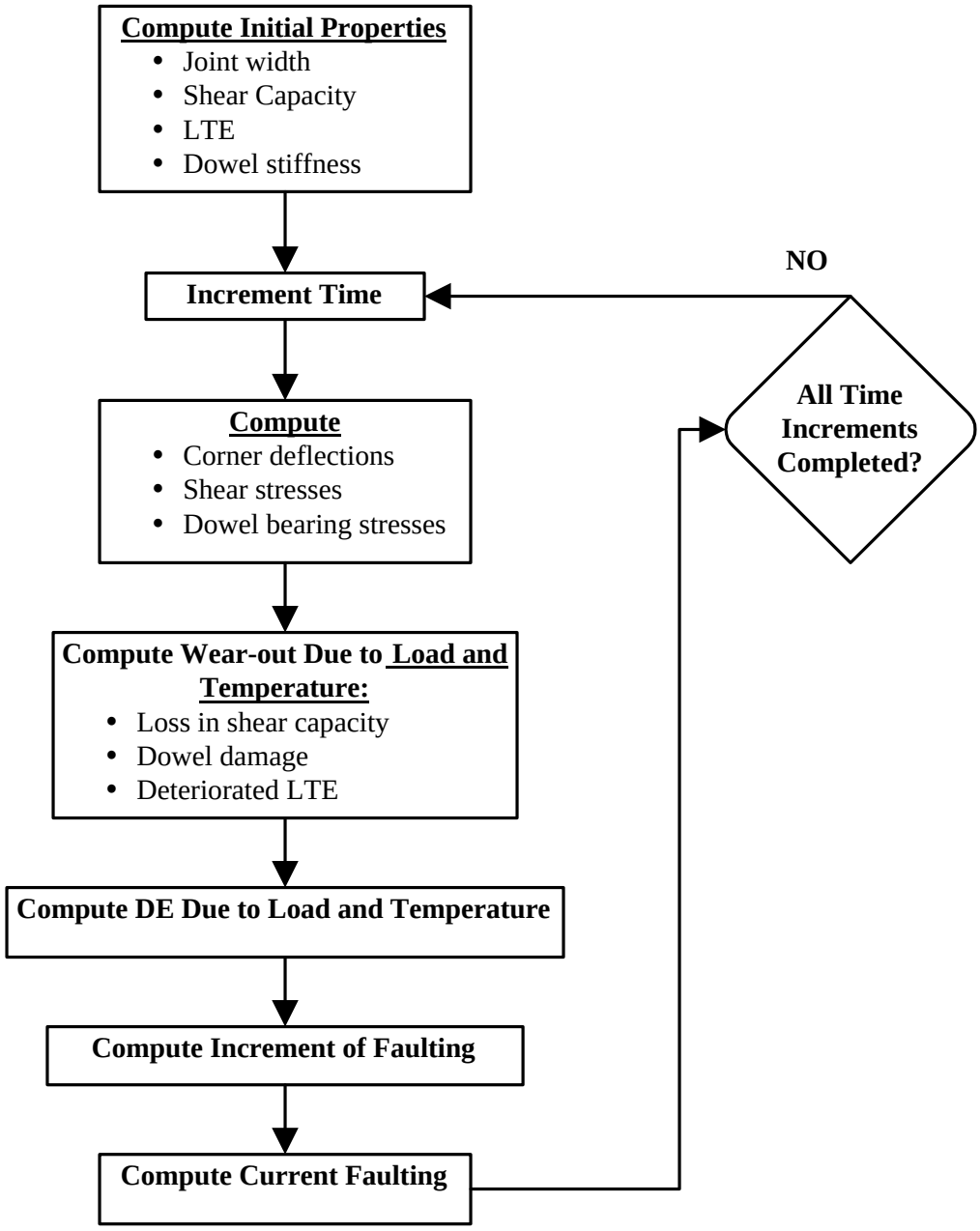


Figure 3. Flowchart showing the transverse joint faulting prediction process (computations will be performed by a neural network program).

## CALIBRATION OF 2002 DESIGN FAULTING MODEL

The JPCP transverse joint faulting model given in equations 41 through 46 is a result of calibration based on performance of 248 field sections located in 22 States. The calibration sections consist of 138 LTPP GPS-3 and SPS-2 sections and 110 sections from the FHWA study, *Performance of Concrete Pavements.*[3] Time-series data were available for many of the sections, making the total number of field cracking observations 560.

### Calibration Process

The process of calibration involved determination of the calibration parameters $C_1$ through $C_7$ from equations 41 through 46 and rate of dowel deterioration parameter, $C_8$, from equation 39, which minimize the error function, ERR, defined as:

$$ERR(C_1, C_2, ..., C_8) = \sum_{ob=1}^{Nob} \left(FaultPredicted_{ob} - FaultMeasured_{ob}\right)^2 \qquad (47)$$

Where

| | | |
|---|---|---|
| ERR | = | Error function. |
| $C_1, C_2, ..., C_8$ | = | Calibration parameters. |
| $FaultPredicted_{ob}$ | = | Predicted faulting for observation *ob* in the calibration database. |
| $FaultMeasured_{ob}$ | = | Measured faulting for observation *ob* in the calibration Database. |
| Nob | = | Number of observation in the calibration database. |

To minimize the error function, the following conditions should be satisfied:

$$\frac{\partial ERR(C_1, C_2, ..., C_8)}{\partial C_1} = 0$$
$$\frac{\partial ERR(C_1, C_2, ..., C_8,)}{\partial C_2} = 0 \qquad (48)$$
$$....$$
$$\frac{\partial ERR(C_1, C_2, ..., C_8)}{\partial C_8} = 0$$

These conditions do not guarantee reaching a global minimum of the error function. Nevertheless, if these values are within reasonable limits it will provide a practically acceptable solution. The procedure involves the following steps:

1. Prepare several typical examples of the design inputs.
2. Perform sensitivity analysis of faulting prediction to the calibration parameters
3. Select reasonable ranges of the calibration parameters.
4. Assemble database of performance data along with 2002 Design Guide inputs.
5. Fix several calibration parameters and vary the remaining ones to find their values corresponding to the lowers value of the error function.

6. Fix the parameters varied in the in the previous step to the values corresponding to the lowest value of the error function and vary other parameters.

Note 1. Repeat steps 5 and 6 many times until no significant reduction in error function can be found.
Note 2. The easiest way to perform, steps 5 and 6 is to change the variable value with a small step within pre-assigned interval. If the lowest value of the error function corresponds to one of the end of the interval then the interval should be increased.

The process used to determine the calibration parameters is described below. The same procedure is recommended for calibration of the 2002 Design Guide faulting model for local conditions.

Step 1. Prepare typical examples of design inputs.

A typical PCC pavement section located in Aurora, Illinois, was selected. This section was used as a baseline for the sensitivity study. The design inputs for that section are provided in table 8. One can see that this is a 9-in-thick PCC undoweled pavement with a granular base placed over A-7-6 subgrade, according to AASHTO classification. The pavement has an AC shoulder. The traffic volume is approximately 10.3 million heavy trucks (or approximately 19 million ESALs) over the design life.

Step 2. Perform sensitivity of faulting prediction to calibration parameters.

The calibration parameters can be divided into two groups:

- Parameters affecting the shape of the faulting vs. traffic or faulting vs. time prediction curve (parameters $C_1$, $C_2$, $C_3$, $C_4$, and $C_7$)
- Parameters magnifying the effects of design feature and site condition, such as dowel diameter of base erodibility (parameters $C_6$, $C_7$, and $C_8$).

Parameters affecting the shape of the faulting curve can be further subdivided into there groups:

- Parameters affecting the magnitudes of mid-range faulting ($C_1$ and $C_2$). Parameter $C_1$ affects faulting prediction regarding of the climatic conditions. Parameter $C_2$ affect sensitivity of faulting prediction to percentage of time the bottom of the PCC slab is frozen.
- Parameters affecting the rate of the initial faulting development ($C_3$ and $C_4$). Parameter $C_3$ affects rate of faulting development prediction regarding of the climatic conditions. Parameter $C_3$ affect sensitivity of rate of faulting prediction to percentage of time the bottom of the PCC slab is frozen.
- A parameter affecting the long term rate of faulting increase ($C_7$)

Figure 4 illustrates different parts of the faulting development. Figures 5, 6, and 7 present sensitivity of faulting prediction to parameters $C_1$, $C_3$, and $C_7$. One can see that change of these coefficients may significantly change the shape of the faulting development curve and the

magnitude of the predicted faulting. It should be also noted that change in the initial slope naturally changes mid-ranges faulting prediction and vise versa.

Parameters $C_5$, $C_6$, and $C_8$ are responsible for magnifying the effect of different design feature on faulting prediction. Parameter $C_5$ correlates change in erodibility with change in predicted faulting. Parameter $C_6$ correlates influence of overburden on subgrade, percent subgrade material passing #200 sieve, and average annual number of wet days with faulting potential. Parameter $C_8$ is responsible for the rate of deterioration of doweled joints. Figure 8 present sensitivity of faulting prediction to parameters $C_8$ for a sections with input parameters summarized in table 8 but dowel diameter equal to 1 in. One see that increase in $C_8$ leads to decrease of the effect of dowels on predicted faulting.

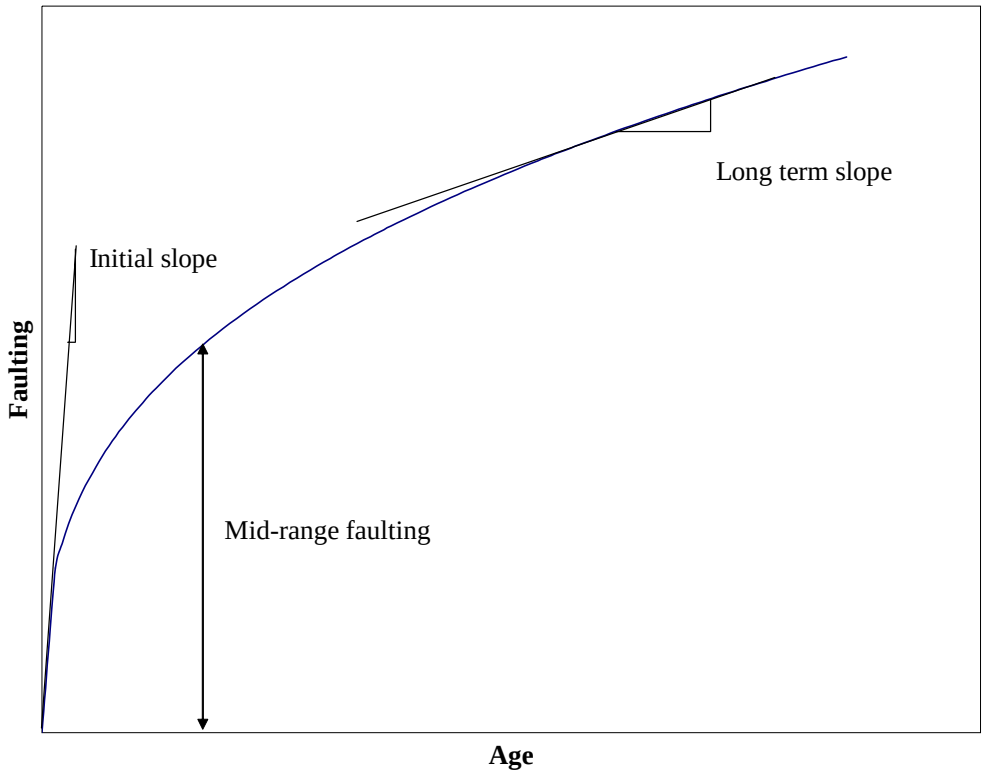


Figure 4. Different stages of faulting development.

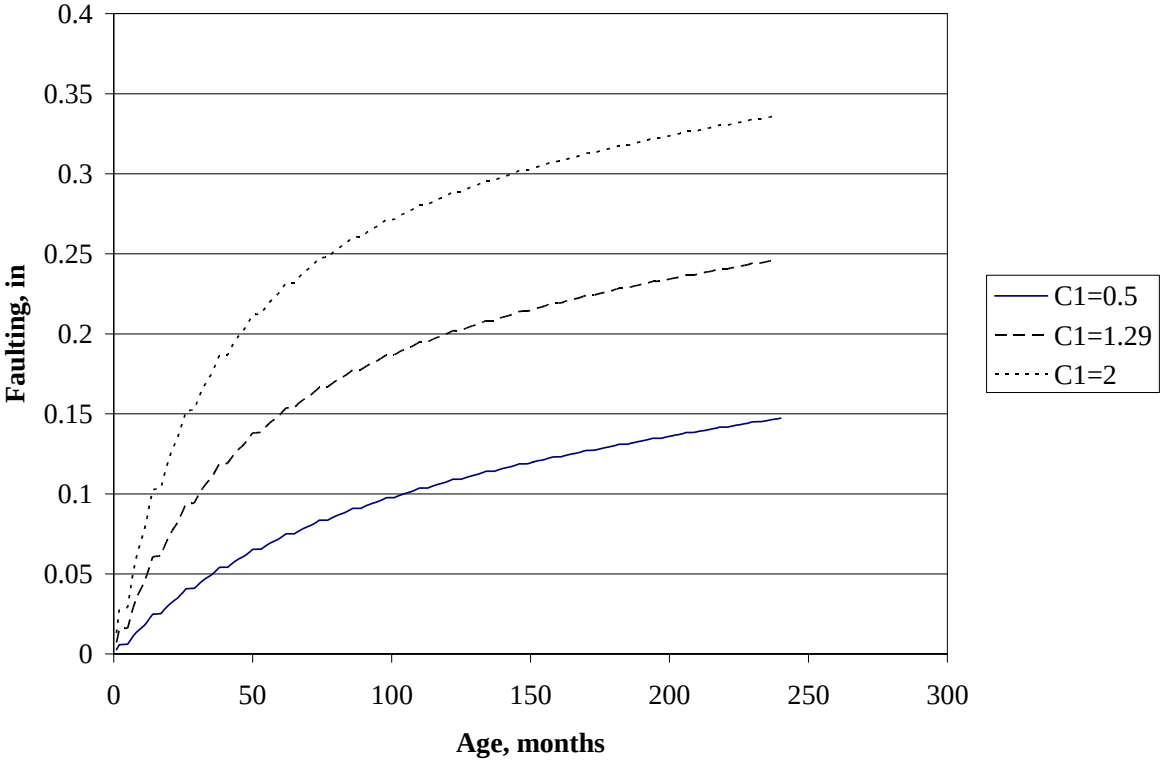


Figure 5. Effect of parameter $C_1$ on faulting prediction.

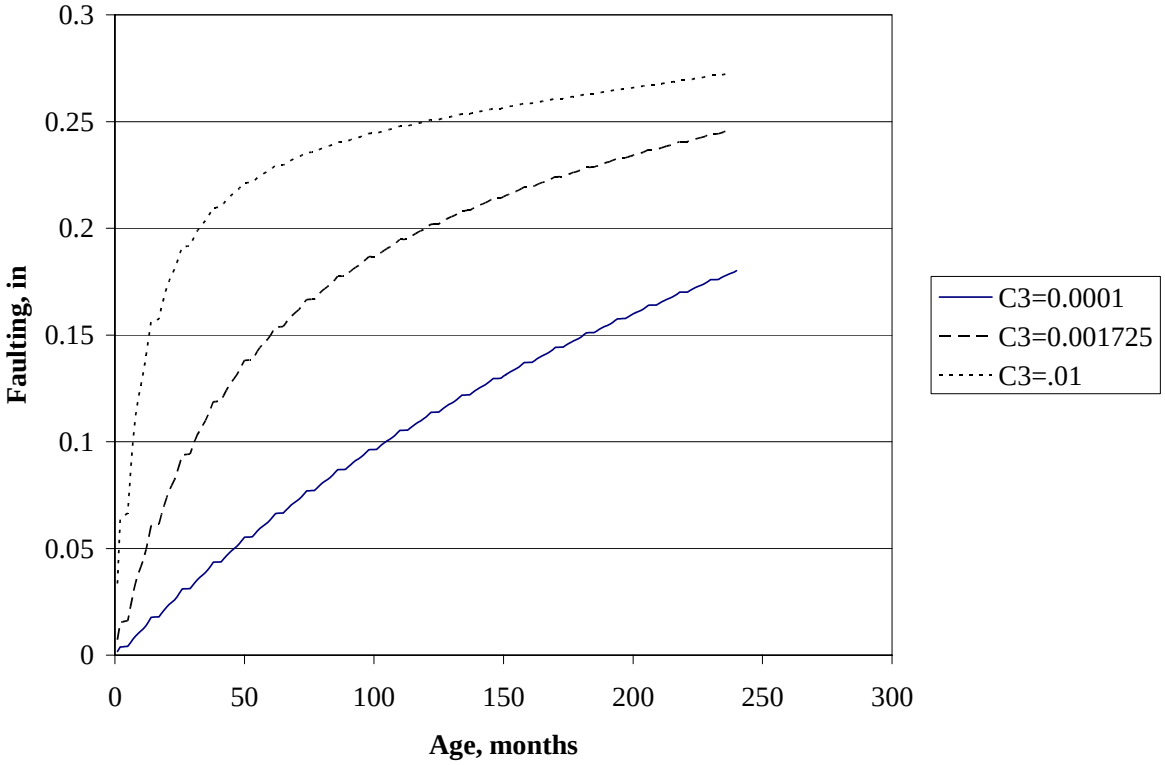


Figure 6. Effect of parameter $C_3$ on faulting prediction.

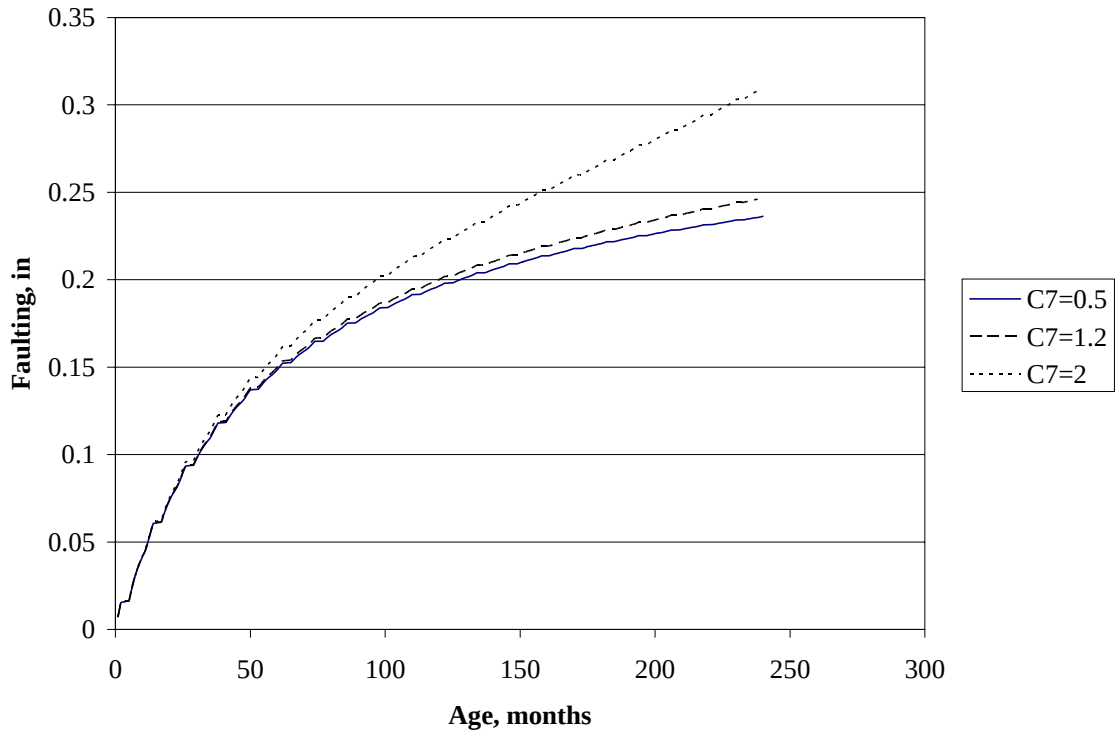


Figure 7. Effect of parameter $C_7$ on faulting prediction.

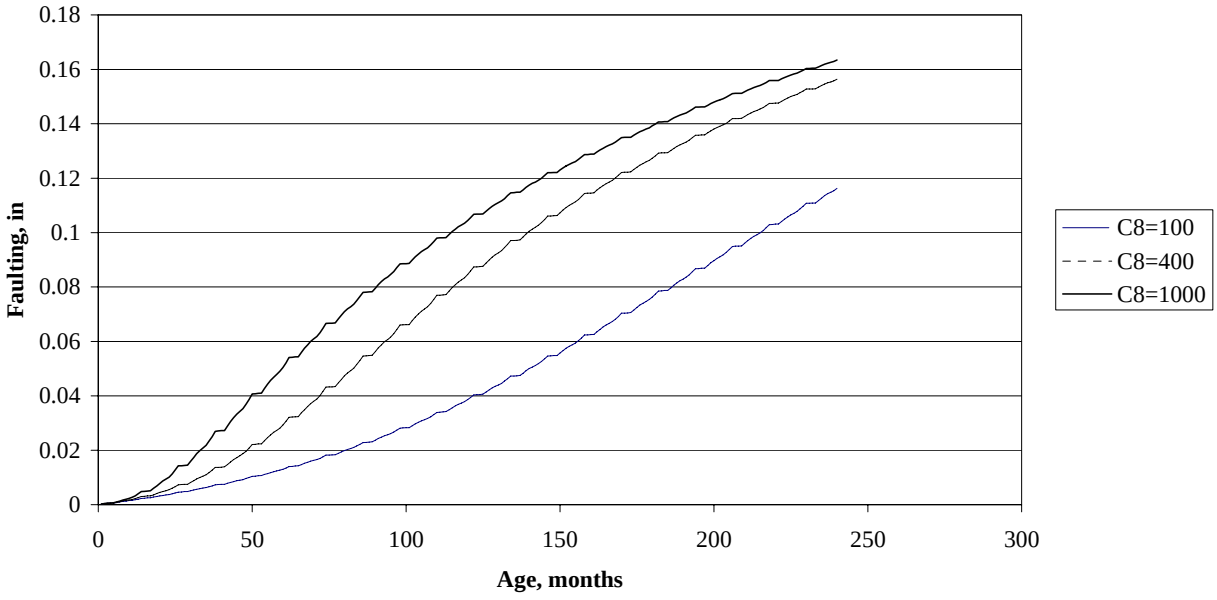


Figure 8. Effect of parameter $C_8$ on faulting prediction.

Table 8. Input parameter for a typical pavement section.

## General Information

| | |
|---|---|
| Design Life | 20 years |
| Pavement construction month: | September, 2003 |
| Traffic open month: | October, 2003 |
| Type of design | JPCP |

## Traffic

| | |
|---|---|
| Two-way average annual daily truck traffic: | 2000 |
| Number of lanes in design direction: | 2 |
| Percent of trucks in design direction (%): | 50 |
| Percent of trucks in design lane (%): | 95 |
| Operational speed (mph): | 60 |

## Traffic -- Monthly Adjustment Factors

**Monthly Adjustment Factors** (Level 3, Default MAF)

| Month | Vehicle Class | | | | | | | | | |
|---|---|---|---|---|---|---|---|---|---|---|
| | Class 4 | Class 5 | Class 6 | Class 7 | Class 8 | Class 9 | Class 10 | Class 11 | Class 12 | Class 13 |
| January | 1.00 | 1.00 | 1.00 | 1.00 | 1.00 | 1.00 | 1.00 | 1.00 | 1.00 | 1.00 |
| February | 1.00 | 1.00 | 1.00 | 1.00 | 1.00 | 1.00 | 1.00 | 1.00 | 1.00 | 1.00 |
| March | 1.00 | 1.00 | 1.00 | 1.00 | 1.00 | 1.00 | 1.00 | 1.00 | 1.00 | 1.00 |
| April | 1.00 | 1.00 | 1.00 | 1.00 | 1.00 | 1.00 | 1.00 | 1.00 | 1.00 | 1.00 |
| May | 1.00 | 1.00 | 1.00 | 1.00 | 1.00 | 1.00 | 1.00 | 1.00 | 1.00 | 1.00 |
| June | 1.00 | 1.00 | 1.00 | 1.00 | 1.00 | 1.00 | 1.00 | 1.00 | 1.00 | 1.00 |
| July | 1.00 | 1.00 | 1.00 | 1.00 | 1.00 | 1.00 | 1.00 | 1.00 | 1.00 | 1.00 |
| August | 1.00 | 1.00 | 1.00 | 1.00 | 1.00 | 1.00 | 1.00 | 1.00 | 1.00 | 1.00 |
| September | 1.00 | 1.00 | 1.00 | 1.00 | 1.00 | 1.00 | 1.00 | 1.00 | 1.00 | 1.00 |
| October | 1.00 | 1.00 | 1.00 | 1.00 | 1.00 | 1.00 | 1.00 | 1.00 | 1.00 | 1.00 |
| November | 1.00 | 1.00 | 1.00 | 1.00 | 1.00 | 1.00 | 1.00 | 1.00 | 1.00 | 1.00 |
| December | 1.00 | 1.00 | 1.00 | 1.00 | 1.00 | 1.00 | 1.00 | 1.00 | 1.00 | 1.00 |

**Vehicle Class Distribution**

(Level 3, Default Distribution)

**AADTT distribution by vehicle class**

| | |
|---|---|
| Class 4 | 1.8% |
| Class 5 | 24.6% |
| Class 6 | 7.6% |
| Class 7 | 0.5% |
| Class 8 | 5.0% |
| Class 9 | 31.3% |
| Class 10 | 9.8% |
| Class 11 | 0.8% |
| Class 12 | 3.3% |
| Class 13 | 15.3% |

**Hourly truck traffic distribution**

by period beginning:

| | | | |
|---|---|---|---|
| Midnight | 2.3% | Noon | 5.9% |
| 1:00 am | 2.3% | 1:00 pm | 5.9% |
| 2:00 am | 2.3% | 2:00 pm | 5.9% |
| 3:00 am | 2.3% | 3:00 pm | 5.9% |
| 4:00 am | 2.3% | 4:00 pm | 4.6% |
| 5:00 am | 2.3% | 5:00 pm | 4.6% |
| 6:00 am | 5.0% | 6:00 pm | 4.6% |
| 7:00 am | 5.0% | 7:00 pm | 4.6% |
| 8:00 am | 5.0% | 8:00 pm | 3.1% |
| 9:00 am | 5.0% | 9:00 pm | 3.1% |
| 10:00 am | 5.9% | 10:00 pm | 3.1% |
| 11:00 am | 5.9% | 11:00 pm | 3.1% |

**Traffic Growth Factor**

| Vehicle Class | Growth Rate | Growth Function |
|---|---|---|
| Class 4 | 4.0% | Compound |
| Class 5 | 4.0% | Compound |
| Class 6 | 4.0% | Compound |
| Class 7 | 4.0% | Compound |
| Class 8 | 4.0% | Compound |
| Class 9 | 4.0% | Compound |
| Class 10 | 4.0% | Compound |
| Class 11 | 4.0% | Compound |
| Class 12 | 4.0% | Compound |
| Class 13 | 4.0% | Compound |

## Traffic -- Axle Load Distribution Factors

Level 3: Default -- normalized initial axle load distribution factors are summarized in worksheet: "Initial LDF"

## Traffic -- General Traffic Inputs

| | |
|---|---|
| Mean wheel location (inches from the lane marking): | 18 |
| Traffic wander standard deviation (in): | 10 |
| Design lane width (ft): | 12 |

Table 8. Input parameter for a typical pavement section (continued).

**Number of Axles per Truck**

| Vehicle Class | Single Axle | Tandem Axle | Tridem Axle | Quad Axle |
|---|---|---|---|---|
| Class 4 | 1.62 | 0.39 | 0.00 | 0.00 |
| Class 5 | 2.00 | 0.00 | 0.00 | 0.00 |
| Class 6 | 1.02 | 0.99 | 0.00 | 0.00 |
| Class 7 | 1.00 | 0.26 | 0.83 | 0.00 |
| Class 8 | 2.38 | 0.67 | 0.00 | 0.00 |
| Class 9 | 1.13 | 1.93 | 0.00 | 0.00 |
| Class 10 | 1.19 | 1.09 | 0.89 | 0.00 |
| Class 11 | 4.29 | 0.26 | 0.06 | 0.00 |
| Class 12 | 3.52 | 1.14 | 0.06 | 0.00 |
| Class 13 | 2.15 | 2.13 | 0.35 | 0.00 |

## Climate

icm file: aurora
Latitude (degrees.minutes): 41.46
Longitude (degrees.minutes): -88.29
Elevation (ft): 706
Depth of water table (ft): 15

## Structure--Design Features

Permanent curl/warp effective temperature difference (°F): -10

### Joint Design

Joint spacing (ft): 15
Sealant type: Liquid
Dowel diameter (in): n/a
Dowel bar spacing (in): n/a

### Edge Support

None
Long-term LTE(%): n/a
Slab width(ft): n/a

### Base Properties

Base type: Granular
Erodibility index: Fairly Erodable (4)
Base/slab friction coefficient: 0.85

## Structure--ICM Properties

Surface shortwave absorptivity: 0.85

#### Drainage Parameters

Infiltration: Minor (10%)
Drainage path length (ft): 12
Pavement cross slope (%): 2

## Structure--Layers

### Layer 1 -- JPCP

#### General Properties

PCC material: JPCP
Layer thickness (in): 9
Unit weight (pcf): 150
Poisson's ratio: 0.2

#### Thermal Properties

Coefficient of thermal expansion (per F° x 10- 6): 5.5
Thermal conductivity (BTU/hr-ft-F°) : 1.25
Heat capacity (BTU/lb-F°): 0.28

#### Mix Properties

Cement type: Type I
Cement content (lb/yd^3): 600
Water/cement ratio: 0.42
Aggregate type: Limestone
PCC zero-stress temperature (F°) n/a
Ultimate shrinkage at 40% R.H (microstrain) n/a
Reversible shrinkage (% of ultimate shrinkage): 50
Time to develop 50% of ultimate shrinkage (days): 35
Curing method: Curing compound

Table 8. Input parameter for a typical pavement section (continued).

**Layer 2 -- A-1-a**

| | |
|---|---|
| Unbound Material: | A-1-a |
| Thickness(in): | 6 |

**Strength Properties**

| | |
|---|---|
| Input Level: | Level 3 |
| Analysis Type: | ICM inputs (Using ICM) |
| Poisson's ratio: | 0.35 |
| Coefficient of lateral pressure,Ko: | 0.5 |
| Modulus (input) (psi): | 40000 |

**ICM Inputs**

Gradation and Plasticity Index

| | |
|---|---|
| Plasticity Index, PI: | 1 |
| Passing #200 sieve (%): | 3 |
| Passing #4 sieve (%): | 20 |
| D60 (mm): | 8 |

Thermal Properties

| | |
|---|---|
| Dry thermal conductivity (BTU/hr-ft-F°): | 0.23 |
| Dry heat capacity (BTU/lb-F°): | 0.17 |

Calculated/Derived Parameters

| | |
|---|---|
| Maximum dry unit weight (pcf): | 122.2 (derived) |
| Specific gravity of solids, Gs: | 2.66 (derived) |
| Saturated hydraulic conductivity (ft/hr): | 263 (derived) |
| Optimum gravimetric water content (%): | 11.1 (derived) |
| Calculated degree of saturation (%): | 82 (calculated) |

Soil water characteristic curve parameters: Default values

| Parameters | Value |
|---|---|
| a | 11.1 |
| b | 1.83 |
| c | 0.51 |
| Hr. | 361 |

**Layer 3 -- A-7-6**

| | |
|---|---|
| Unbound Material: | A-7-6 |
| Thickness(in): | Semi-infinite |

**Strength Properties**

| | |
|---|---|
| Input Level: | Level 3 |
| Analysis Type: | ICM inputs (Using ICM) |
| Poisson's ratio: | 0.35 |
| Coefficient of lateral pressure,Ko: | 0.5 |
| Modulus (input) (psi): | 8000 |

**ICM Inputs**

Gradation and Plasticity Index

| | |
|---|---|
| Plasticity Index, PI: | 40 |
| Passing #200 sieve (%): | 90 |
| Passing #4 sieve (%): | 99 |
| D60 (mm): | 0.01 |

Thermal Properties

| | |
|---|---|
| Dry thermal conductivity (BTU/hr-ft-F°): | 0.23 |
| Dry heat capacity (BTU/lb-F°): | 0.17 |

Calculated/Derived Parameters

| | |
|---|---|
| Maximum dry unit weight (pcf): | 91.3 (derived) |
| Specific gravity of solids, Gs: | 2.77 (derived) |
| Saturated hydraulic conductivity (ft/hr): | 4.86e-008 (derived) |
| Optimum gravimetric water content (%): | 28.8 (derived) |
| Calculated degree of saturation (%): | 89.4 (calculated) |

Soil water characteristic curve parameters: Default values

| Parameters | Value |
|---|---|
| a | 750 |
| b | 0.911 |
| c | 0.772 |
| Hr. | 47500 |

**Calibration Database**

As it was mentioned above, the calibration databases consists of 248 field sections located in 22 States, as shown in figure 9. The calibration sections consist of 138 LTPP GPS-3 and SPS-2 sections and 110 sections from the FHWA study *Performance of Concrete Pavements*.[3] Table 9 presents key parameters of the sections used in calibration. One can see that more than one-third of the sections (86 sections) are nondoweled. The dowel diameter in the remaining sections varies from 1 in to 1.5 in. For the faulting model calibration, unlike the JPCP cracking model calibration, the sections with random joint spacing were considered as sections with joint spacing equal to mean joint spacing. Time-series data were available for many of the sections, making the total number of field cracking observations 560.

The age distribution of the JPCP faulting calibration sections is shown in figure 10. About one-third of the sections were 10 years or older at the time of cracking survey, and more than a quarter of the sections had experienced 5 million trucks or more. In terms of ESALs, about 20 percent of the sections had experienced more than 10 million ESALs at the time of the cracking survey. Thus, the JPCP faulting calibration database includes a sufficient number of pavement sections with adequate age and traffic levels to form a reasonable basis for calibrating a model that will be used to predict the performance of pavements subjected to heavy traffic over a long period of time.

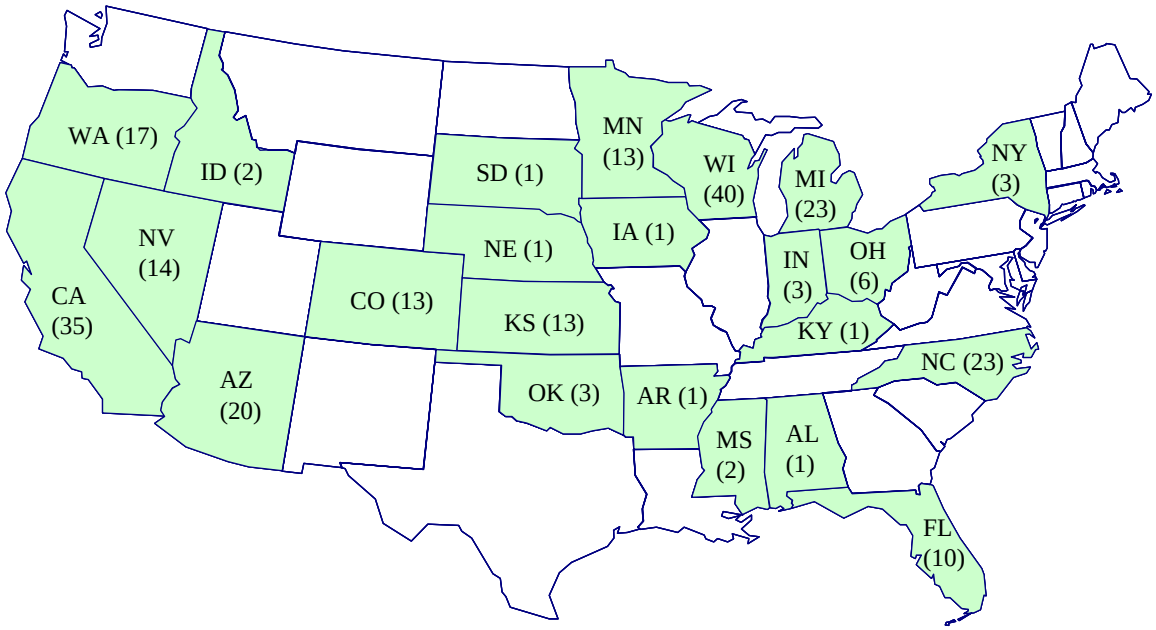


Figure 9. Geographical distribution of JPCP cracking calibration sections.

**Calibration Results**

Using non-linear optimization techniques, the following values of the calibration parameters were found:

| | | | |
|---|---|---|---|
| $C_1$ = 1.29 | | $C_5$ = | 250 |
| $C_2$ = 1.1 | | $C_6$ = | 0.4 |
| $C_3$ = 0.001725 | | $C_7$ = | 1.2 |
| $C_4$ = 0.0008 | | $C_8$ = | 400 |

Plots of the predicted versus measured faulting, and residuals versus predicted faulting, are shown in figures 11 and 12, respectively. The diagnostic statistics and both plots verify that the model is effective for predicting transverse joint faulting. The $R^2$ of 71 percent and SEE of 0.0267 in are very reasonable given the large number of data points (N = 560) used in model development.

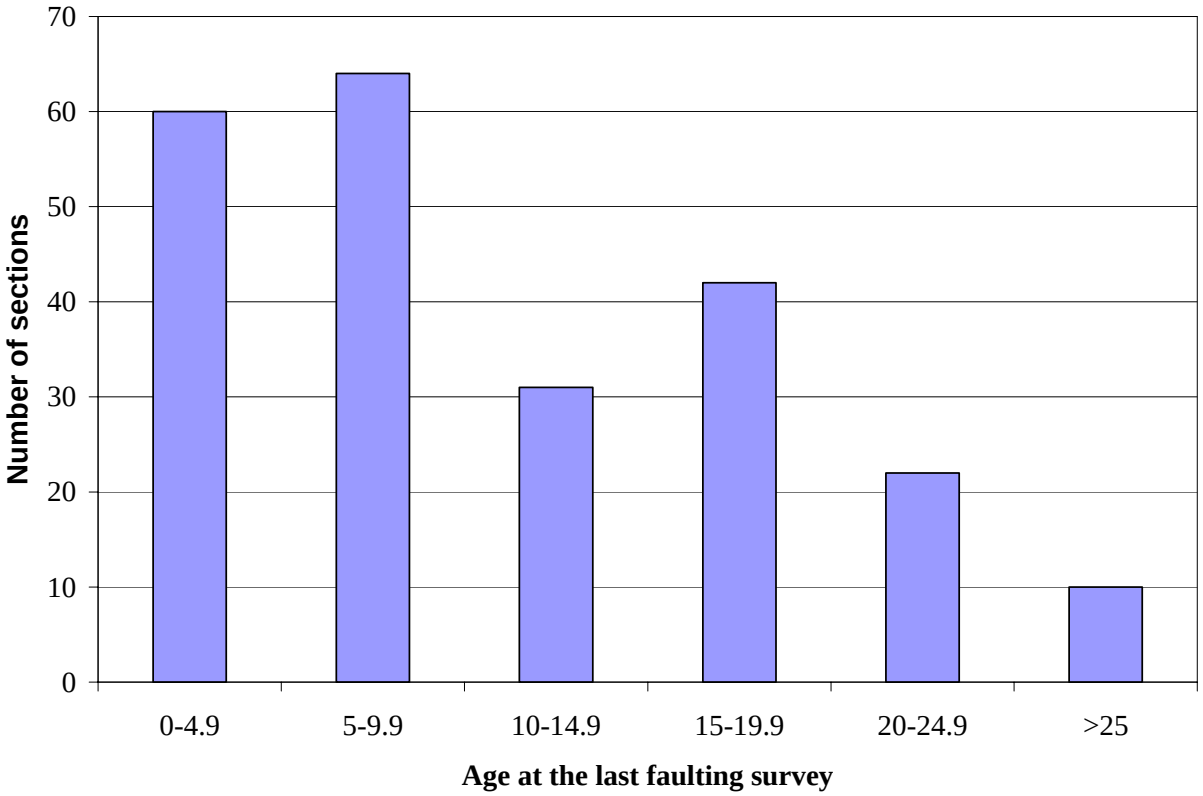


Figure 10. Age distribution of JPCP faulting calibration data points.

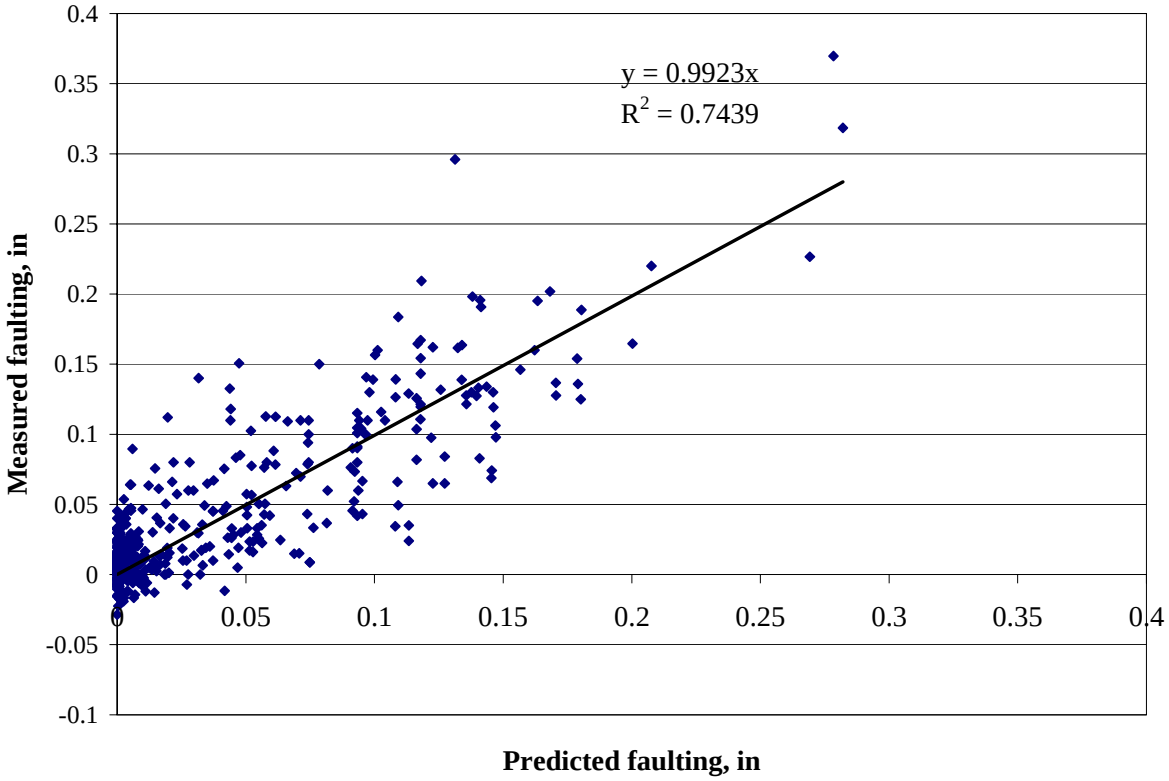


Figure 11. Actual vs. predicted cracking.

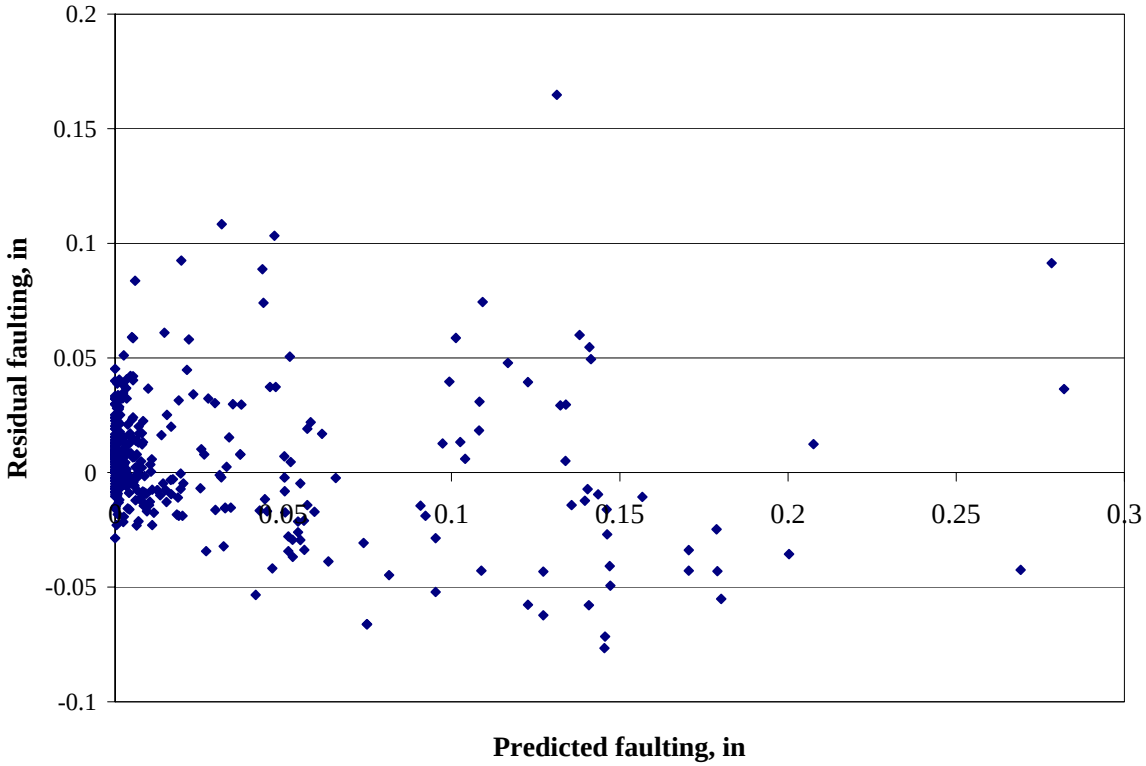


Figure 12. Actual vs. residual cracking.

Table 9. Major characteristics of pavement sections used in calibration.

| Section ID | Database | PCC Thickness, in | Joint Spacing, Ft | Dowel Diameter, in | Shoulder LTE, Percent | Base Type | Base Erodibility |
|---|---|---|---|---|---|---|---|
| 1_3028 | LTPP | 10.2 | 20.0 | 0.00 | 10.00 | AGG | 4 |
| 12_3804 | LTPP | 12.0 | 19.5 | 1.25 | 25.00 | CTB | 3 |
| 12_3811 | LTPP | 9.4 | 20.0 | 0.00 | 10.00 | CTB | 3 |
| 12_4000 | LTPP | 8.2 | 20.0 | 0.00 | 10.00 | CTB | 3 |
| 12_4057 | LTPP | 13.3 | 15.5 | 1.25 | 25.00 | AGG | 4 |
| 12_4059 | LTPP | 6.4 | 14.0 | 0.00 | 10.00 | ATB | 4 |
| 12_4109 | LTPP | 7.1 | 14.0 | 0.00 | 10.00 | AGG | 4 |
| 12_4138 | LTPP | 8.0 | 20.0 | 0.00 | 10.00 | CTB | 3 |
| 16_3017 | LTPP | 10.3 | 14.5 | 1.25 | 10.00 | ATB | 3 |
| 18_3002 | LTPP | 9.5 | 15.5 | 1.25 | 25.00 | AGG | 4 |
| 18_3003 | LTPP | 10.2 | 20.0 | 1.25 | 10.00 | ATB | 1 |
| 18_3031 | LTPP | 10.2 | 15.5 | 1.25 | 10.00 | ATB | 3 |
| 20_0201 | LTPP | 7.7 | 15.0 | 1.25 | 10.00 | AGG | 4 |
| 20_0202 | LTPP | 7.4 | 15.0 | 1.25 | 10.00 | AGG | 4 |
| 20_0203 | LTPP | 11.1 | 15.0 | 1.50 | 10.00 | AGG | 4 |
| 20_0204 | LTPP | 11.3 | 15.0 | 1.50 | 10.00 | AGG | 4 |
| 20_0205 | LTPP | 7.8 | 15.0 | 1.25 | 10.00 | CTB | 1 |
| 20_0206 | LTPP | 7.9 | 15.0 | 1.25 | 10.00 | CTB | 1 |
| 20_0207 | LTPP | 11.3 | 15.0 | 1.50 | 10.00 | CTB | 1 |
| 20_0208 | LTPP | 11.0 | 15.0 | 1.50 | 10.00 | CTB | 1 |
| 20_0209 | LTPP | 8.5 | 15.0 | 1.25 | 10.00 | ATB | 1 |
| 20_0210 | LTPP | 8.3 | 15.0 | 1.25 | 10.00 | ATB | 1 |
| 20_0211 | LTPP | 11.1 | 15.0 | 1.50 | 10.00 | ATB | 1 |
| 20_0212 | LTPP | 10.9 | 15.0 | 1.50 | 10.00 | ATB | 1 |
| 21_3016 | LTPP | 11.8 | 15.0 | 1.37 | 10.00 | AGG | 4 |
| 26_0213 | LTPP | 8.6 | 15.0 | 1.25 | 10.00 | AGG | 4 |
| 26_0215 | LTPP | 11.2 | 15.0 | 1.50 | 10.00 | AGG | 4 |
| 26_0216 | LTPP | 11.4 | 15.0 | 1.50 | 10.00 | AGG | 4 |
| 26_0217 | LTPP | 8.5 | 15.0 | 1.25 | 10.00 | CTB | 1 |
| 26_0218 | LTPP | 7.1 | 15.0 | 1.25 | 10.00 | CTB | 1 |
| 26_0219 | LTPP | 10.9 | 15.0 | 1.50 | 10.00 | CTB | 1 |
| 26_0220 | LTPP | 11.1 | 15.0 | 1.50 | 10.00 | CTB | 1 |
| 26_0221 | LTPP | 8.2 | 15.0 | 1.25 | 10.00 | ATB | 1 |
| 26_0222 | LTPP | 8.4 | 15.0 | 1.25 | 10.00 | ATB | 1 |
| 26_0223 | LTPP | 11.0 | 15.0 | 1.50 | 10.00 | ATB | 1 |
| 26_0224 | LTPP | 11.2 | 15.0 | 1.50 | 10.00 | ATB | 1 |
| 28_3018 | LTPP | 9.3 | 20.0 | 1.00 | 10.00 | CTB | 3 |
| 28_3019 | LTPP | 9.4 | 20.0 | 1.00 | 10.00 | CTB | 3 |
| 31_3018 | LTPP | 11.9 | 15.5 | 0.00 | 25.00 | CTB | 3 |
| 32_0201 | LTPP | 9.2 | 15.0 | 1.25 | 10.00 | AGG | 4 |
| 32_0202 | LTPP | 8.2 | 15.0 | 1.25 | 10.00 | AGG | 4 |

Table 9. Major characteristics of pavement sections used in calibration (continued).

| Section ID | Database | PCC Thickness, in | Joint Spacing, ft | Dowel Diameter, in | Shoulder LTE, Percent | Base Type | Base Erodibility |
|---|---|---|---|---|---|---|---|
| 32_0203 | LTPP | 11.9 | 15.0 | 1.50 | 10.00 | AGG | 4 |
| 32_0204 | LTPP | 11.8 | 15.0 | 1.50 | 10.00 | AGG | 4 |
| 32_0205 | LTPP | 8.5 | 15.0 | 1.25 | 10.00 | CTB | 1 |
| 32_0206 | LTPP | 7.8 | 15.0 | 1.25 | 10.00 | CTB | 1 |
| 32_0207 | LTPP | 10.9 | 15.0 | 1.50 | 10.00 | CTB | 1 |
| 32_0208 | LTPP | 11.0 | 15.0 | 1.50 | 10.00 | CTB | 1 |
| 32_0209 | LTPP | 8.9 | 15.0 | 1.25 | 10.00 | ATB | 1 |
| 32_0210 | LTPP | 10.1 | 15.0 | 1.25 | 10.00 | ATB | 1 |
| 32_0211 | LTPP | 11.3 | 15.0 | 1.50 | 10.00 | ATB | 1 |
| 32_3010 | LTPP | 9.7 | 15.5 | 0.00 | 10.00 | CTB | 3 |
| 32_7084 | LTPP | 11.0 | 13.5 | 0.00 | 25.00 | ATB | 1 |
| 37_0201 | LTPP | 9.0 | 15.0 | 1.50 | 10.00 | AGG | 4 |
| 37_0202 | LTPP | 10.2 | 15.0 | 1.50 | 10.00 | AGG | 4 |
| 37_0203 | LTPP | 11.2 | 15.0 | 1.50 | 10.00 | AGG | 4 |
| 37_0204 | LTPP | 11.2 | 15.0 | 1.50 | 10.00 | AGG | 4 |
| 37_0205 | LTPP | 8.0 | 15.0 | 1.50 | 10.00 | CTB | 1 |
| 37_0206 | LTPP | 8.4 | 15.0 | 1.50 | 10.00 | CTB | 1 |
| 37_0207 | LTPP | 11.6 | 15.0 | 1.50 | 10.00 | CTB | 1 |
| 37_0208 | LTPP | 11.2 | 15.0 | 1.50 | 10.00 | CTB | 1 |
| 37_0209 | LTPP | 8.6 | 15.0 | 1.50 | 10.00 | ATB | 1 |
| 37_0210 | LTPP | 8.4 | 15.0 | 1.50 | 10.00 | ATB | 1 |
| 37_0211 | LTPP | 11.4 | 15.0 | 1.50 | 10.00 | ATB | 1 |
| 37_0212 | LTPP | 10.9 | 15.0 | 1.50 | 10.00 | ATB | 1 |
| 37_3008 | LTPP | 7.9 | 21.3 | 1.00 | 10.00 | CTB | 2 |
| 37_3011 | LTPP | 10.0 | 30.0 | 1.25 | 10.00 | ATB | 3 |
| 37_3807 | LTPP | 9.4 | 21.3 | 0.00 | 25.00 | CTB | 3 |
| 37_3816 | LTPP | 9.3 | 30.0 | 1.12 | 10.00 | CTB | 3 |
| 39_3013 | LTPP | 8.3 | 17.0 | 0.00 | 10.00 | CTB | 3 |
| 39_3801 | LTPP | 9.2 | 20.0 | 1.25 | 10.00 | CTB | 3 |
| 4_0213 | LTPP | 7.9 | 15.0 | 1.25 | 10.00 | AGG | 4 |
| 4_0214 | LTPP | 8.3 | 15.0 | 1.25 | 10.00 | AGG | 4 |
| 4_0215 | LTPP | 11.3 | 15.0 | 1.50 | 10.00 | AGG | 4 |
| 4_0216 | LTPP | 11.2 | 15.0 | 1.50 | 10.00 | AGG | 4 |
| 4_0217 | LTPP | 8.1 | 15.0 | 1.25 | 10.00 | CTB | 1 |
| 4_0218 | LTPP | 8.3 | 15.0 | 1.25 | 10.00 | CTB | 1 |
| 4_0219 | LTPP | 10.8 | 15.0 | 1.50 | 10.00 | CTB | 1 |
| 4_0220 | LTPP | 11.3 | 15.0 | 1.50 | 10.00 | CTB | 1 |
| 4_0221 | LTPP | 8.2 | 15.0 | 1.25 | 10.00 | ATB | 1 |
| 4_0222 | LTPP | 8.6 | 15.0 | 1.25 | 10.00 | ATB | 1 |
| 4_0223 | LTPP | 11.1 | 15.0 | 1.50 | 10.00 | ATB | 1 |
| 4_0224 | LTPP | 10.7 | 15.0 | 1.50 | 10.00 | ATB | 1 |
| 4_7614 | LTPP | 9.7 | 15.0 | 1.25 | 10.00 | CTB | 3 |
| 40_4162 | LTPP | 9.2 | 15.0 | 0.00 | 10.00 | ATB | 1 |

Table 9. Major characteristics of pavement sections used in calibration (continued).

| Section ID | Database | PCC Thickness, in | Joint Spacing, ft | Dowel Diameter, in | Shoulder LTE, Percent | Base Type | Base Erodibility |
|---|---|---|---|---|---|---|---|
| 46_3012 | LTPP | 10.1 | 15.0 | 0.00 | 10.00 | AGG | 4 |
| 5_3011 | LTPP | 10.1 | 15.0 | 1.00 | 10.00 | ATB | 3 |
| 53_0201 | LTPP | 8.7 | 15.0 | 1.25 | 10.00 | AGG | 4 |
| 53_0202 | LTPP | 8.3 | 15.0 | 1.25 | 10.00 | AGG | 4 |
| 53_0203 | LTPP | 11.1 | 15.0 | 1.50 | 10.00 | AGG | 4 |
| 53_0204 | LTPP | 11.2 | 15.0 | 1.50 | 10.00 | AGG | 4 |
| 53_0205 | LTPP | 8.5 | 15.0 | 1.25 | 10.00 | CTB | 1 |
| 53_0206 | LTPP | 8.6 | 15.0 | 1.25 | 10.00 | CTB | 1 |
| 53_0208 | LTPP | 11.2 | 15.0 | 1.50 | 10.00 | CTB | 1 |
| 53_0209 | LTPP | 9.0 | 15.0 | 1.25 | 10.00 | ATB | 1 |
| 53_0210 | LTPP | 8.3 | 15.0 | 1.25 | 10.00 | ATB | 1 |
| 53_0211 | LTPP | 11.8 | 15.0 | 1.50 | 10.00 | ATB | 1 |
| 53_0212 | LTPP | 11.3 | 15.0 | 1.50 | 10.00 | ATB | 1 |
| 53_3011 | LTPP | 9.6 | 11.5 | 0.00 | 10.00 | AGG | 4 |
| 53_3013 | LTPP | 8.2 | 15.5 | 0.00 | 10.00 | AGG | 4 |
| 53_3014 | LTPP | 10.4 | 11.5 | 0.00 | 10.00 | AGG | 4 |
| 53_3019 | LTPP | 9.9 | 11.5 | 0.00 | 10.00 | AGG | 4 |
| 53_3813 | LTPP | 8.0 | 15.0 | 0.00 | 10.00 | AGG | 4 |
| 53_7409 | LTPP | 9.3 | 11.5 | 0.00 | 10.00 | AGG | 4 |
| 55_3009 | LTPP | 8.6 | 15.3 | 0.00 | 10.00 | AGG | 4 |
| 55_3010 | LTPP | 10.8 | 14.9 | 0.00 | 25.00 | AGG | 4 |
| 55_3016 | LTPP | 8.9 | 15.5 | 0.00 | 10.00 | AGG | 4 |
| 55_6351 | LTPP | 10.0 | 15.5 | 0.00 | 10.00 | AGG | 4 |
| 55_6352 | LTPP | 9.2 | 15.5 | 1.13 | 10.00 | AGG | 4 |
| 55_6353 | LTPP | 10.5 | 15.5 | 0.00 | 10.00 | CTB | 3 |
| 55_6354 | LTPP | 9.6 | 15.5 | 0.00 | 10.00 | ATB | 1 |
| 55_6355 | LTPP | 9.3 | 15.5 | 1.13 | 10.00 | ATB | 1 |
| 6_3021 | LTPP | 8.1 | 15.5 | 0.00 | 10.00 | CTB | 3 |
| 8_0213 | LTPP | 8.7 | 15.0 | 1.25 | 10.00 | AGG | 4 |
| 8_0214 | LTPP | 8.4 | 15.0 | 1.25 | 10.00 | AGG | 4 |
| 8_0215 | LTPP | 11.4 | 15.0 | 1.50 | 10.00 | AGG | 4 |
| 8_0216 | LTPP | 11.8 | 15.0 | 1.50 | 10.00 | AGG | 4 |
| 8_0217 | LTPP | 8.6 | 15.0 | 1.25 | 10.00 | CTB | 1 |
| 8_0218 | LTPP | 7.7 | 15.0 | 1.25 | 10.00 | CTB | 1 |
| 8_0219 | LTPP | 11.1 | 15.0 | 1.50 | 10.00 | CTB | 1 |
| 8_0220 | LTPP | 11.1 | 15.0 | 1.50 | 10.00 | CTB | 1 |
| 8_0221 | LTPP | 8.3 | 15.0 | 1.25 | 10.00 | ATB | 1 |
| 8_0222 | LTPP | 8.7 | 15.0 | 1.25 | 10.00 | ATB | 1 |
| 8_0223 | LTPP | 11.8 | 15.0 | 1.50 | 10.00 | ATB | 1 |
| 8_0224 | LTPP | 11.7 | 15.0 | 1.50 | 10.00 | ATB | 1 |
| 8_3032 | LTPP | 8.6 | 15.5 | 0.00 | 10.00 | CTB | 1 |
| AZ1_1 | RIPPER | 9.0 | 15.0 | 0.00 | 10.0 | CTB | 2.00 |
| AZ1_2 | RIPPER | 13.0 | 15.0 | 0.00 | 40.0 | AGG | 4.00 |
| AZ1_4 | RIPPER | 13.0 | 15.0 | 0.00 | 40.0 | AGG | 4.00 |
| AZ1_5 | RIPPER | 11.0 | 15.0 | 0.00 | 40.0 | AGG | 4.00 |

Table 9. Major characteristics of pavement sections used in calibration (continued).

| Section ID | Database | PCC Thickness, in | Joint Spacing, ft | Dowel Diameter, in | Shoulder LTE, Percent | Base Type | Base Erodibility |
|---|---|---|---|---|---|---|---|
| AZ1_6 | RIPPER | 9.0 | 15.0 | 0.00 | 40.0 | CTB | 3.00 |
| AZ1_7 | RIPPER | 9.0 | 15.0 | 0.00 | 40.0 | CTB | 3.00 |
| AZ2 | RIPPER | 10.0 | 15.0 | 1.25 | 40.0 | CTB | 1.00 |
| CA1_10 | RIPPER | 8.4 | 15.5 | 0.00 | 10.0 | CTB | 2.00 |
| CA1_3 | RIPPER | 8.4 | 15.5 | 0.00 | 10.0 | CTB | 2.00 |
| CA1_4 | RIPPER | 8.4 | 15.5 | 0.00 | 10.0 | CTB | 2.00 |
| CA1_5 | RIPPER | 11.4 | 15.5 | 0.00 | 10.0 | CTB | 2.00 |
| CA1_6 | RIPPER | 11.4 | 15.5 | 0.00 | 10.0 | CTB | 2.00 |
| CA1_7 | RIPPER | 8.4 | 15.5 | 0.00 | 10.0 | CTB | 2.00 |
| CA1_8 | RIPPER | 8.4 | 15.5 | 0.00 | 10.0 | CTB | 2.00 |
| CA1_9 | RIPPER | 8.4 | 15.5 | 0.00 | 10.0 | CTB | 2.00 |
| CA10 | RIPPER | 9.0 | 15.5 | 0.00 | 10.0 | ATB | 2.00 |
| CA2_2 | RIPPER | 8.4 | 15.5 | 0.00 | 10.0 | CTB | 2.00 |
| CA2_3 | RIPPER | 8.4 | 15.5 | 0.00 | 10.0 | CTB | 2.00 |
| CA3_1 | RIPPER | 9.0 | 15.5 | 0.00 | 25.00 | CTB | 2.00 |
| CA3_10 | RIPPER | 9.0 | 15.5 | 0.00 | 25.00 | CTB | 2.00 |
| CA3_2 | RIPPER | 9.0 | 15.5 | 0.00 | 25.00 | CTB | 2.00 |
| CA3_3 | RIPPER | 9.0 | 15.5 | 0.00 | 25.00 | CTB | 2.00 |
| CA3_4 | RIPPER | 9.0 | 15.5 | 0.00 | 25.00 | CTB | 2.00 |
| CA3_5 | RIPPER | 9.0 | 15.5 | 0.00 | 25.00 | CTB | 2.00 |
| CA3_6 | RIPPER | 9.0 | 15.5 | 0.00 | 25.00 | CTB | 2.00 |
| CA3_7 | RIPPER | 9.0 | 15.5 | 0.00 | 25.00 | CTB | 2.00 |
| CA3_8 | RIPPER | 9.0 | 15.5 | 0.00 | 25.00 | CTB | 2.00 |
| CA3_9 | RIPPER | 9.0 | 15.5 | 0.00 | 25.00 | CTB | 2.00 |
| CA6_1 | RIPPER | 9.0 | 15.5 | 0.00 | 10.0 | CTB | 2.00 |
| CA6_2 | RIPPER | 9.0 | 15.5 | 0.00 | 10.0 | ATB | 1.00 |
| CA7 | RIPPER | 10.2 | 15.5 | 0.00 | 10.0 | CTB | 2.00 |
| CA8 | RIPPER | 10.2 | 15.5 | 0.00 | 10.0 | ATB | 2.00 |
| CA9_10 | RIPPER | 9.0 | 15.5 | 0.00 | 10.0 | CTB | 2.00 |
| CA9_2 | RIPPER | 9.0 | 15.5 | 0.00 | 10.0 | CTB | 2.00 |
| CA9_3 | RIPPER | 9.0 | 15.5 | 0.00 | 10.0 | CTB | 2.00 |
| CA9_4 | RIPPER | 9.0 | 15.5 | 0.00 | 10.0 | CTB | 2.00 |
| CA9_5 | RIPPER | 9.0 | 15.5 | 0.00 | 10.0 | CTB | 2.00 |
| CA9_8 | RIPPER | 9.0 | 15.5 | 0.00 | 10.0 | CTB | 2.00 |
| FL2 | RIPPER | 13.0 | 15.5 | 1.25 | 25.00 | AGG | 5.00 |
| FL3 | RIPPER | 9.0 | 16.0 | 1.00 | 10.0 | CTB | 5.00 |
| FL4_1 | RIPPER | 9.0 | 20.0 | 1.25 | 10.0 | CTB | 5.00 |
| MI1_10a | RIPPER | 9.0 | 15.5 | 0.00 | 10.0 | ATB | 2.00 |
| MI1_4a | RIPPER | 9.0 | 15.5 | 0.00 | 10.0 | ATB | 1.00 |
| MI1_4a10 | RIPPER | 9.0 | 15.5 | 0.00 | 25.00 | ATB | 1.00 |
| MI1_4a12 | RIPPER | 9.0 | 15.5 | 0.00 | 25.00 | ATB | 1.00 |
| MI1_7a | RIPPER | 9.0 | 15.5 | 1.25 | 10.0 | AGG | 4.00 |
| MI1_7a5 | RIPPER | 9.0 | 15.5 | 1.25 | 10.0 | AGG | 4.00 |
| MI1_7b | RIPPER | 9.0 | 15.5 | 1.25 | 10.0 | AGG | 4.00 |
| MI1_7b5 | RIPPER | 9.0 | 15.5 | 1.25 | 10.0 | AGG | 4.00 |

Table 9. Major characteristics of pavement sections used in calibration (continued).

| Section ID | Database | PCC Thickness, in | Joint Spacing, ft | Dowel Diameter, in | Shoulder LTE, Percent | Base Type | Base Erodibility |
|---|---|---|---|---|---|---|---|
| MN2_1 | RIPPER | 9.0 | 15.5 | 1.00 | 25.00 | AGG | 4.00 |
| MN2_2 | RIPPER | 8.0 | 15.5 | 1.00 | 25.00 | AGG | 4.00 |
| MN4 | RIPPER | 7.5 | 15.5 | 1.00 | 10.0 | AGG | 4.00 |
| MN7_10 | RIPPER | 9.0 | 15.0 | 0.00 | 10.0 | AGG | 4.00 |
| MN7_15 | RIPPER | 9.0 | 15.0 | 1.00 | 10.0 | AGG | 4.00 |
| MN7_17 | RIPPER | 9.0 | 20.0 | 0.00 | 10.0 | AGG | 4.00 |
| MN7_18 | RIPPER | 9.0 | 15.0 | 0.00 | 10.0 | AGG | 4.00 |
| MN7_24 | RIPPER | 9.0 | 15.0 | 1.00 | 10.0 | AGG | 4.00 |
| MN7_9 | RIPPER | 9.0 | 15.0 | 0.00 | 10.0 | AGG | 4.00 |
| NC1_2 | RIPPER | 9.0 | 30.0 | 1.00 | 10.0 | CTB | 2.00 |
| NC1_3 | RIPPER | 9.0 | 30.0 | 0.00 | 10.0 | CTB | 2.00 |
| NC1_4 | RIPPER | 9.0 | 30.0 | 1.00 | 10.0 | AGG | 4.00 |
| NC1_5 | RIPPER | 9.0 | 30.0 | 0.00 | 10.0 | CTB | 4.00 |
| NC1_8 | RIPPER | 9.0 | 30.0 | 0.00 | 10.0 | AGG | 4.00 |
| NC2 | RIPPER | 9.0 | 21.3 | 1.38 | 25.00 | CTB | 2.00 |
| NY2_11 | RIPPER | 9.0 | 26.7 | 1.50 | 25.00 | AGG | 3.00 |
| NY2_3 | RIPPER | 9.0 | 20.0 | 1.50 | 25.00 | AGG | 3.00 |
| NY2_9 | RIPPER | 9.0 | 20.0 | 1.50 | 25.00 | AGG | 3.00 |
| OH2_1 | RIPPER | 15.0 | 20.0 | 0.00 | 25.00 | AGG | 5.00 |
| OH2_2 | RIPPER | 15.0 | 20.0 | 0.00 | 25.00 | AGG | 5.00 |
| OH2_3 | RIPPER | 15.0 | 20.0 | 0.00 | 10.0 | AGG | 5.00 |
| WI1_1 | RIPPER | 11.0 | 18.5 | 1.50 | 10.0 | CTB | 1.00 |
| WI1_2 | RIPPER | 11.0 | 18.5 | 1.50 | 10.0 | CTB | 1.00 |
| WI1_3 | RIPPER | 11.0 | 18.5 | 1.50 | 10.0 | CTB | 1.00 |
| WI2_1 | RIPPER | 9.0 | 15.5 | 1.25 | 10.0 | CTB | 1.00 |
| WI2_2 | RIPPER | 9.0 | 15.5 | 1.25 | 10.0 | ATB | 2.00 |
| WI2_3 | RIPPER | 9.0 | 15.5 | 1.25 | 10.0 | AGG | 2.00 |
| WI2_4 | RIPPER | 9.0 | 15.5 | 1.25 | 10.0 | AGG | 4.00 |
| WI2_5 | RIPPER | 9.0 | 15.5 | 1.25 | 10.0 | AGG | 4.00 |
| WI3_1 | RIPPER | 8.0 | 15.5 | 0.00 | 10.0 | ATB | 1.00 |
| WI3_2 | RIPPER | 8.0 | 15.5 | 0.00 | 10.0 | AGG | 4.00 |
| WI3_3 | RIPPER | 8.0 | 15.5 | 0.00 | 10.0 | AGG | 4.00 |
| WI4_6 | RIPPER | 9.0 | 20.0 | 0.00 | 10.0 | AGG | 4.00 |
| WI5_1 | RIPPER | 10.0 | 15.5 | 0.00 | 10.0 | AGG | 4.00 |

## SENSITIVITY ANALYSIS

### Effect of Dowel Diameter and Edge Support

Figures 13 through 32 present a sensitivity analysis of faulting prediction to dowel diameter and different edge support conditions for typical pavement sections located in Illinois (wet-freeze climate), North Dakota (dry-freeze climate), Florida (wet-no freeze climate), and Arizona (dry-no freeze climate). The following design parameters were used in this sensitivity analysis:

- PCC slab thickness – 9 in
- Base type – aggregate base
- Base thickness – 6 in
- Subgrade type – A-7-6
- Design period – 20 years
- Cumulative number of heavy trucks – 10.3 million (about 19 million ESALs)
- PCC built-in curling - -10$^{o}$F
- Construction month - September

Figures 13 through 17 present the prediction of faulting development over the pavement design life for Illinois sections for an AC shoulder, a PCC shoulder constructed separately, a PCC shoulder constructed monolithically, a widened slab with an AC shoulder, and a widened slab with and a PCC shoulder. For all edge support conditions, the dowel diameter is the most important factor affecting faulting prediction. Proper selection of a dowel diameter is the key in achieving desired long0term pavement performance with respect to faulting. One can also observe that, for all locations, a PCC shoulder constructed monolithically (daytime design LTE = 70%) is more effective in faulting reduction than a PCC shoulder constructed separately (design LTE = 40%). The latter is more effective than an AC shoulder. Analysis of the similar sensitivity plots for North Dakota sections (figures 18 through 22), Florida sections (figures 23 through 27), and Arizona sections (figures 28 through 32) shows that this conclusion is valid for all climatic conditions.

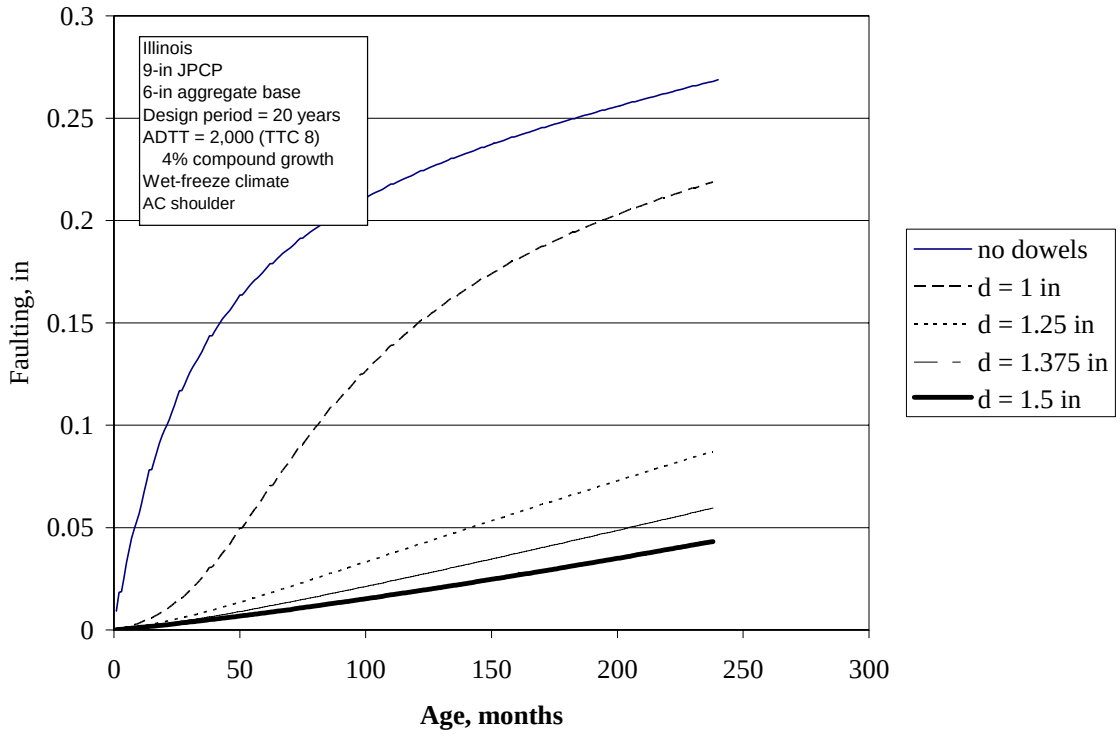


Figure 13. Faulting prediction for Illinois sections. AC shoulder.

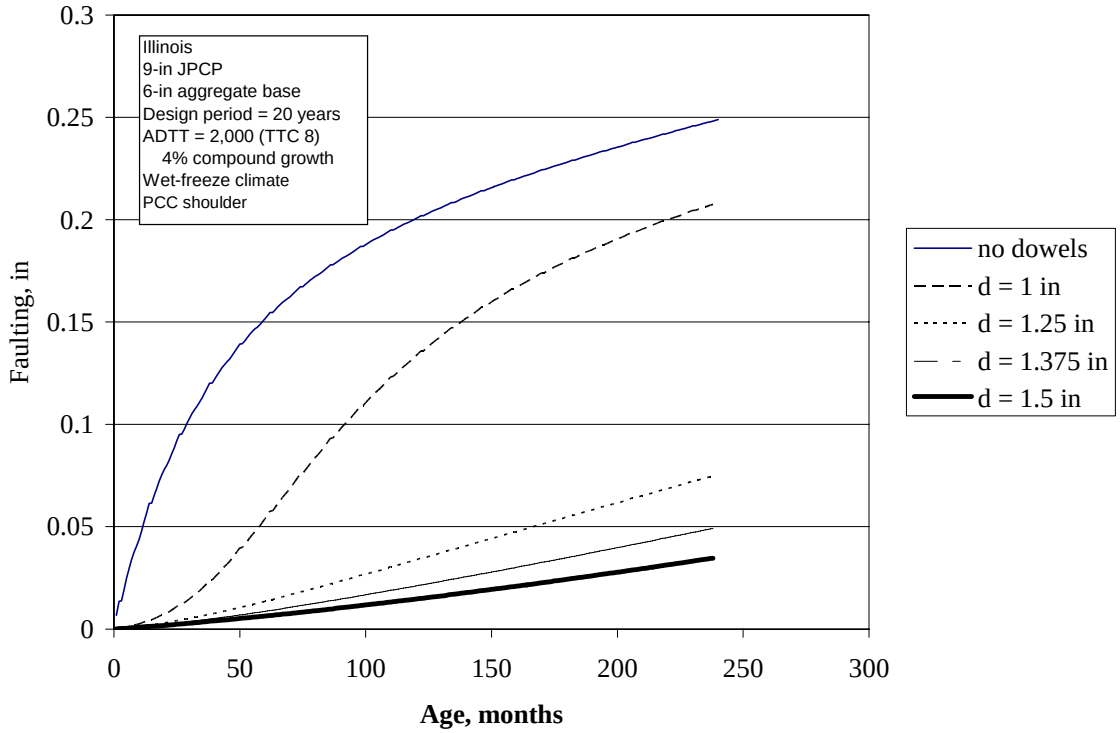


Figure 14. Faulting prediction for Illinois sections. PCC shoulder.

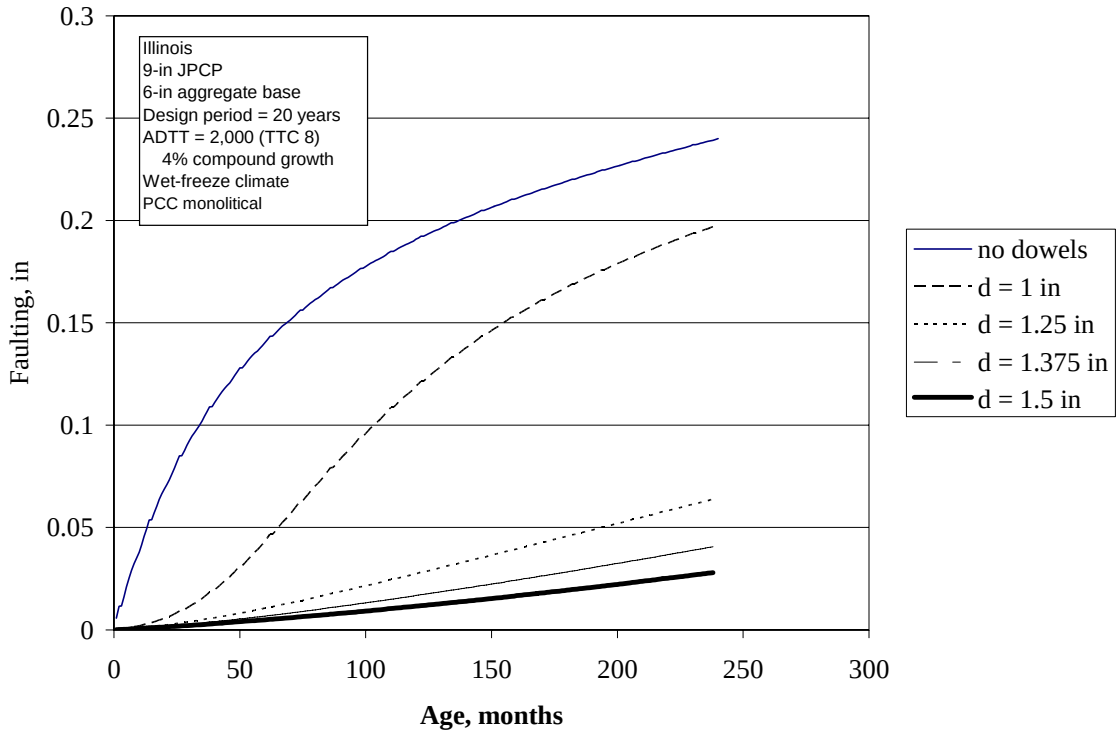


Figure 15. Faulting prediction for Illinois sections. PCC shoulder, constructed monolithically.

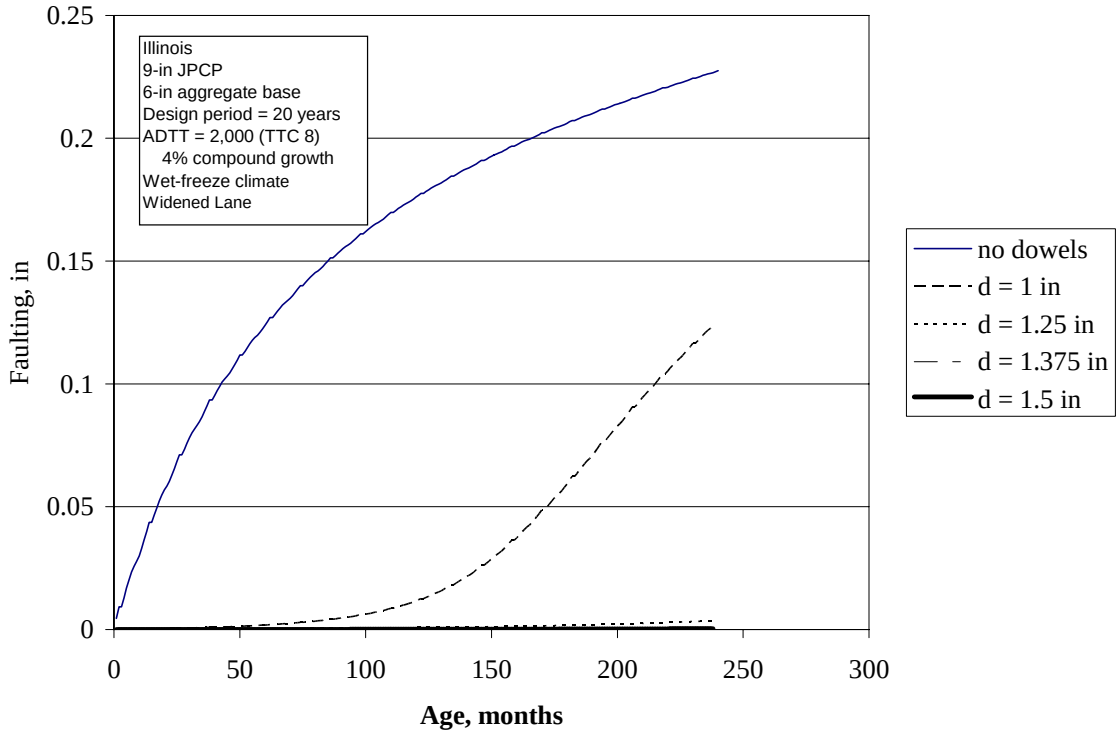


Figure 16. Faulting prediction for Illinois sections. Widened lane, AC shoulder.

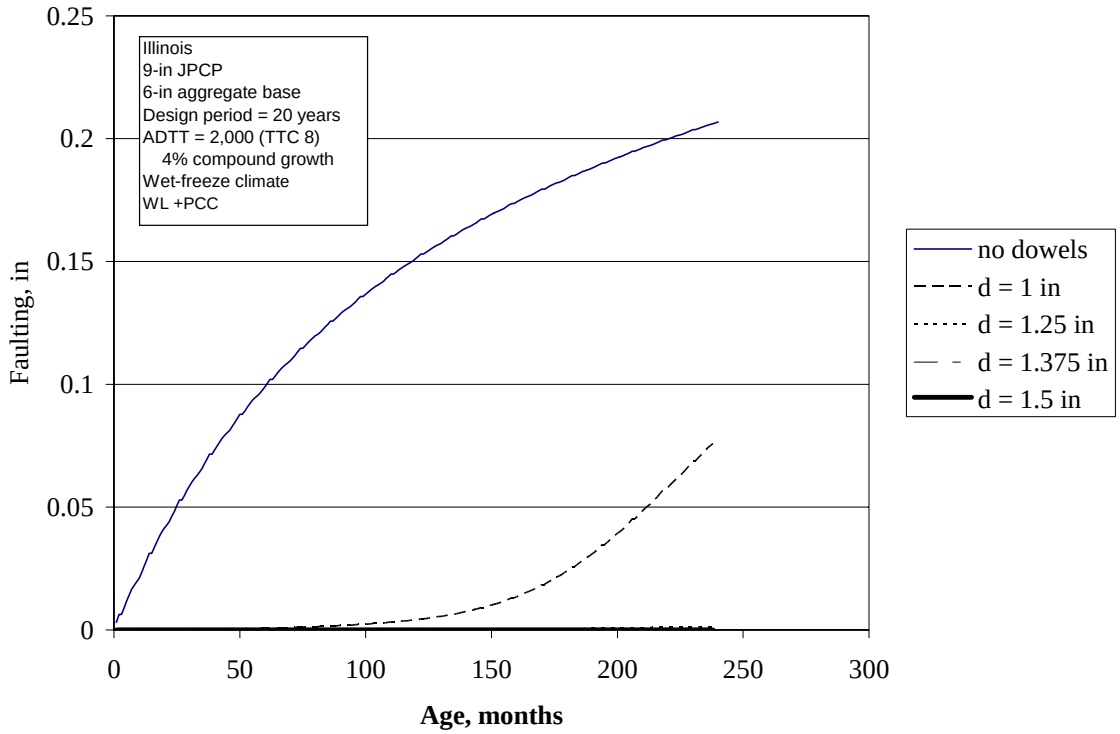


Figure 17. Faulting prediction for Illinois sections. Widened lane, PCC shoulder.

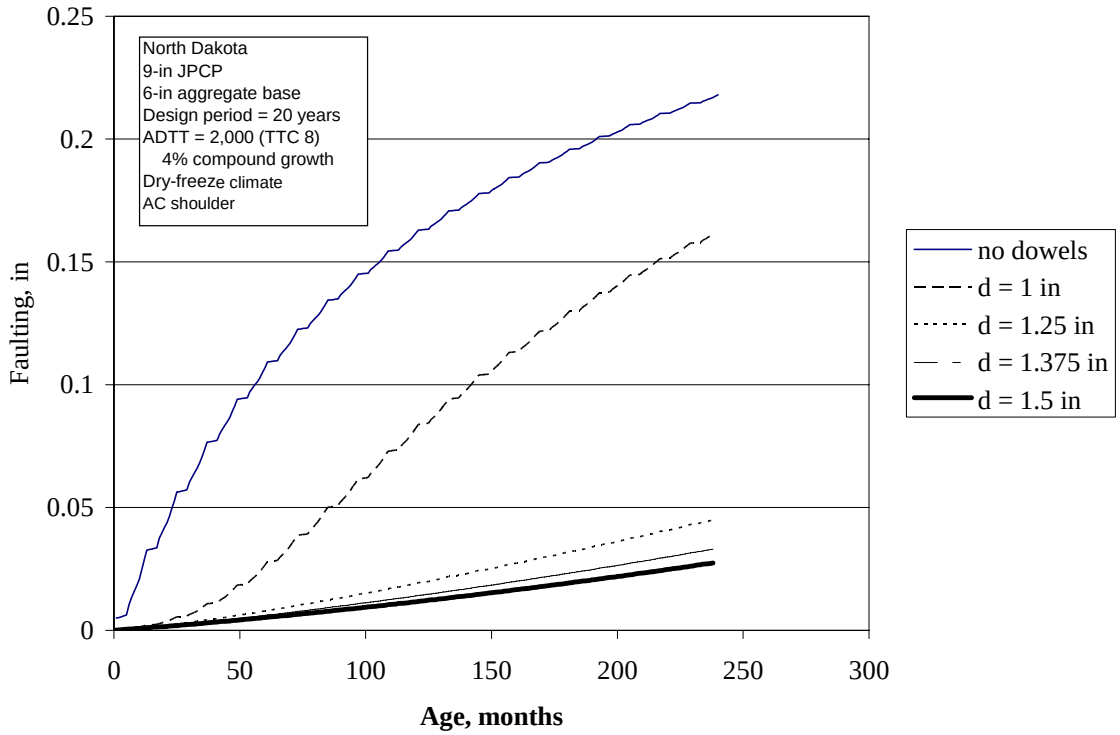


Figure 18. Faulting prediction for North Dakota sections. AC shoulder.

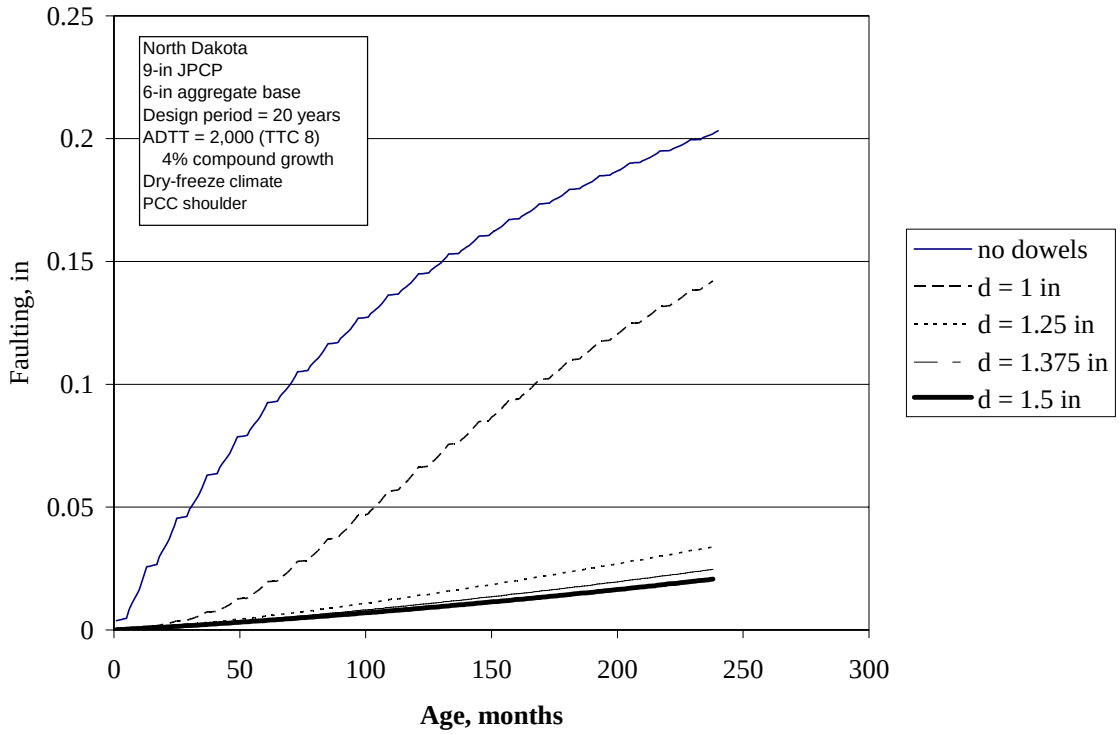


Figure 19. Faulting prediction for North Dakota sections. PCC shoulder.

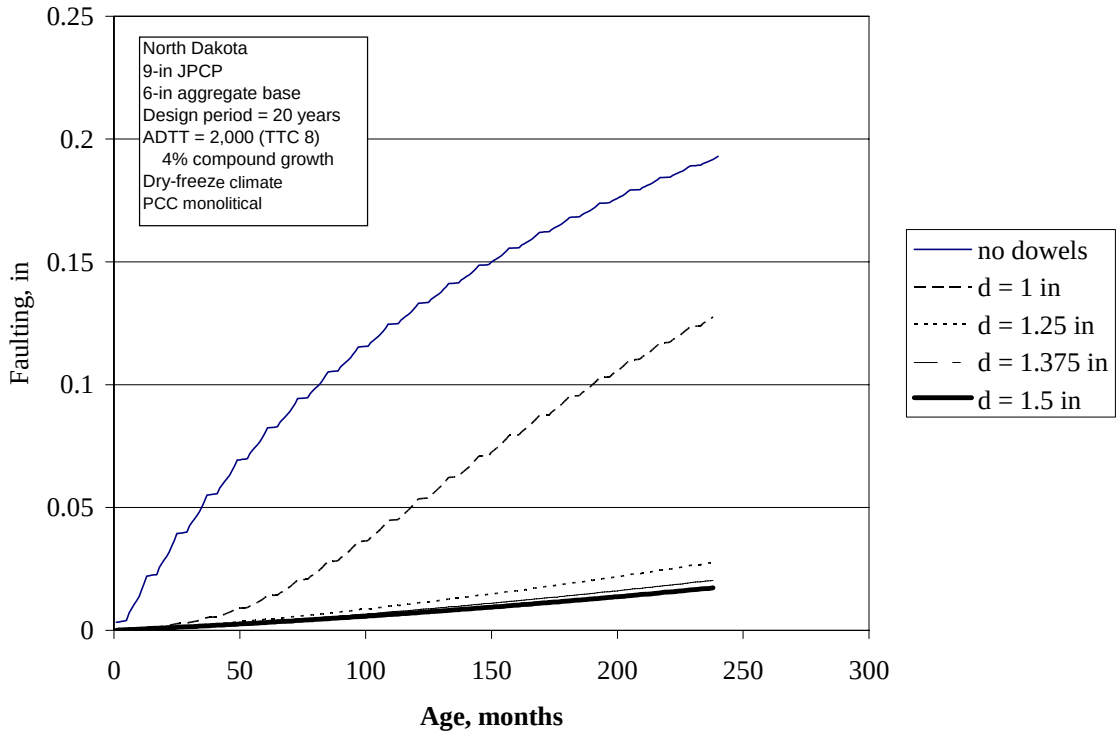


Figure 20. Faulting prediction for North Dakota sections. PCC shoulder, constructed monolithically.

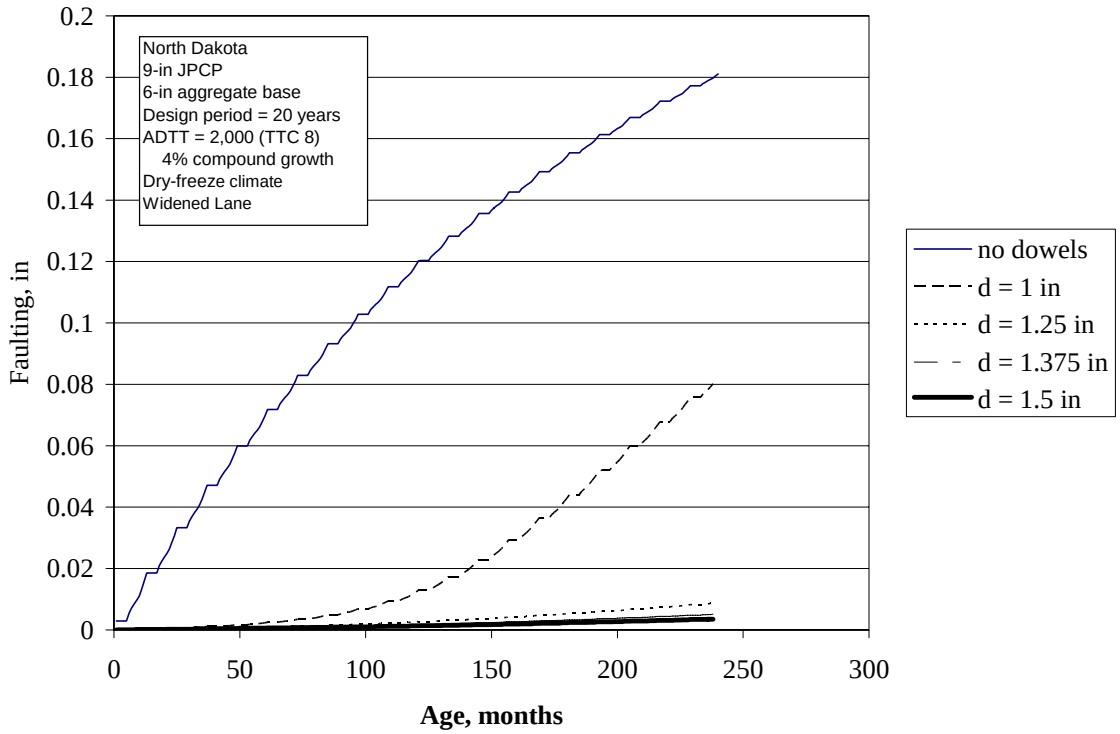


Figure 21. Faulting prediction for North Dakota sections. Widened lane, AC shoulder.

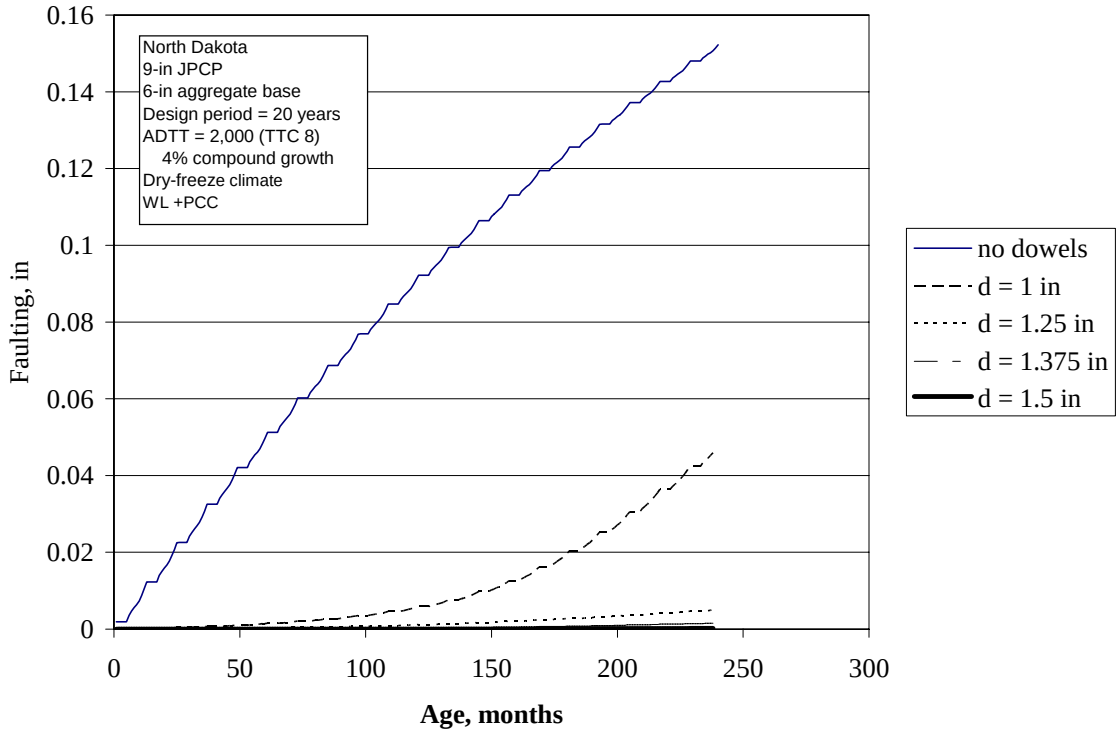


Figure 22. Faulting prediction for North Dakota sections. Widened lane, PCC shoulder.

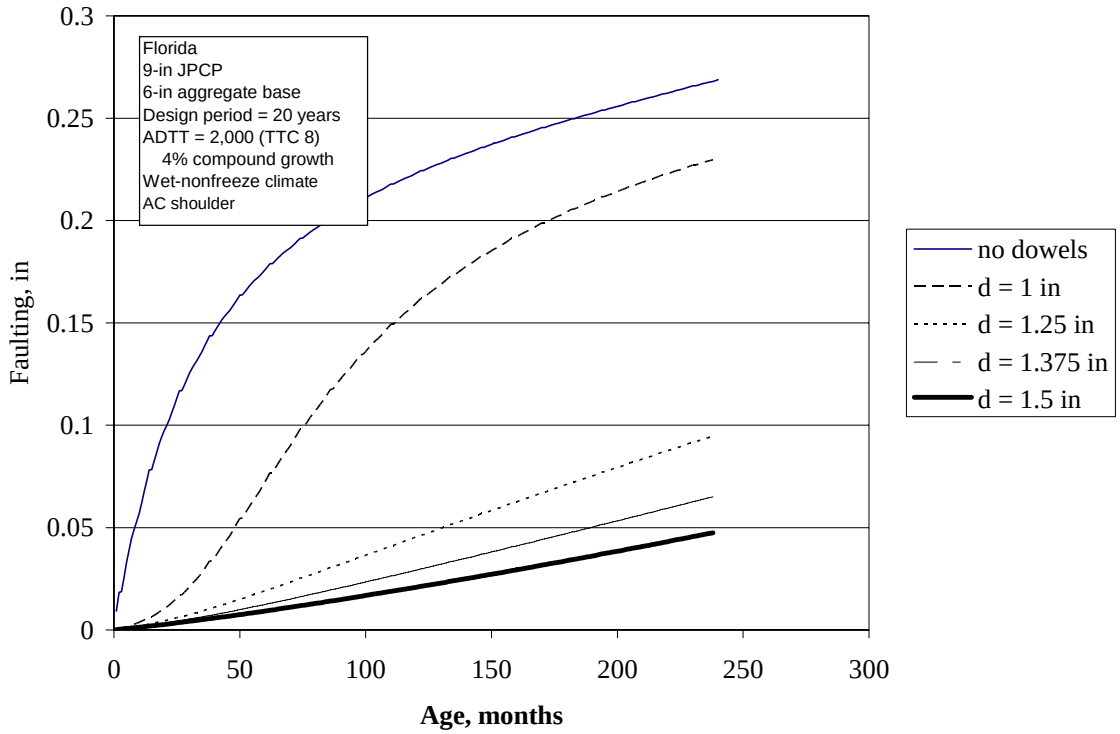


Figure 23. Faulting prediction for Florida sections. AC shoulder.

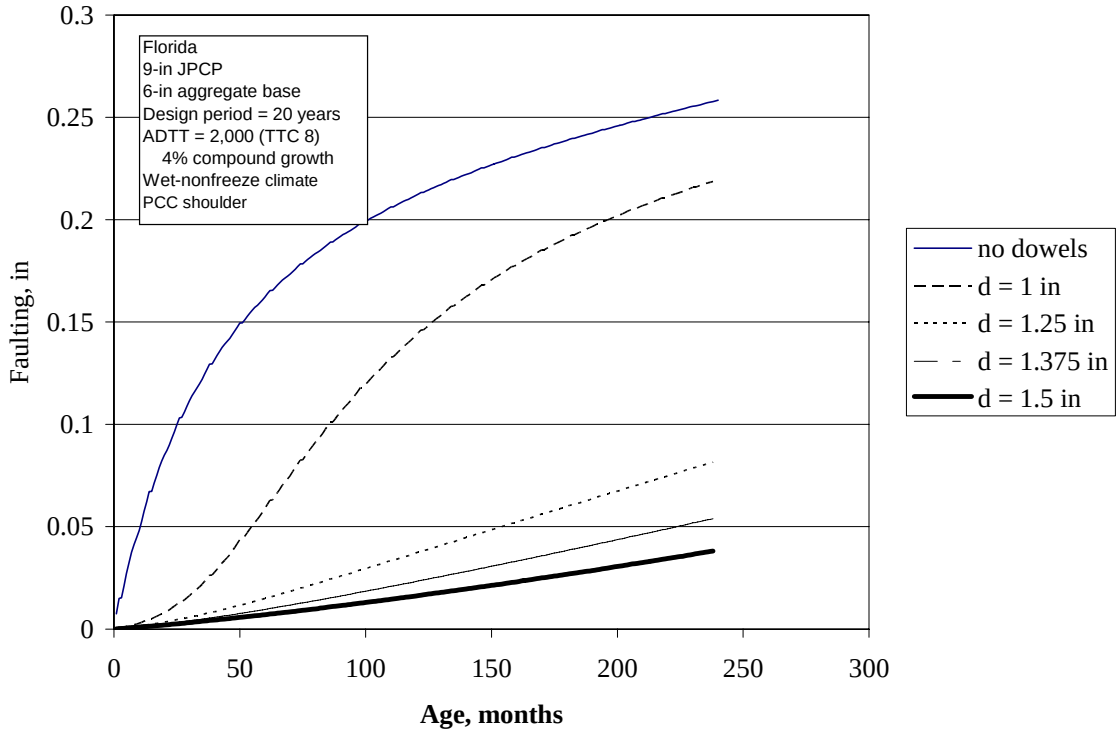


Figure 24. Faulting prediction for Florida sections. PCC shoulder.

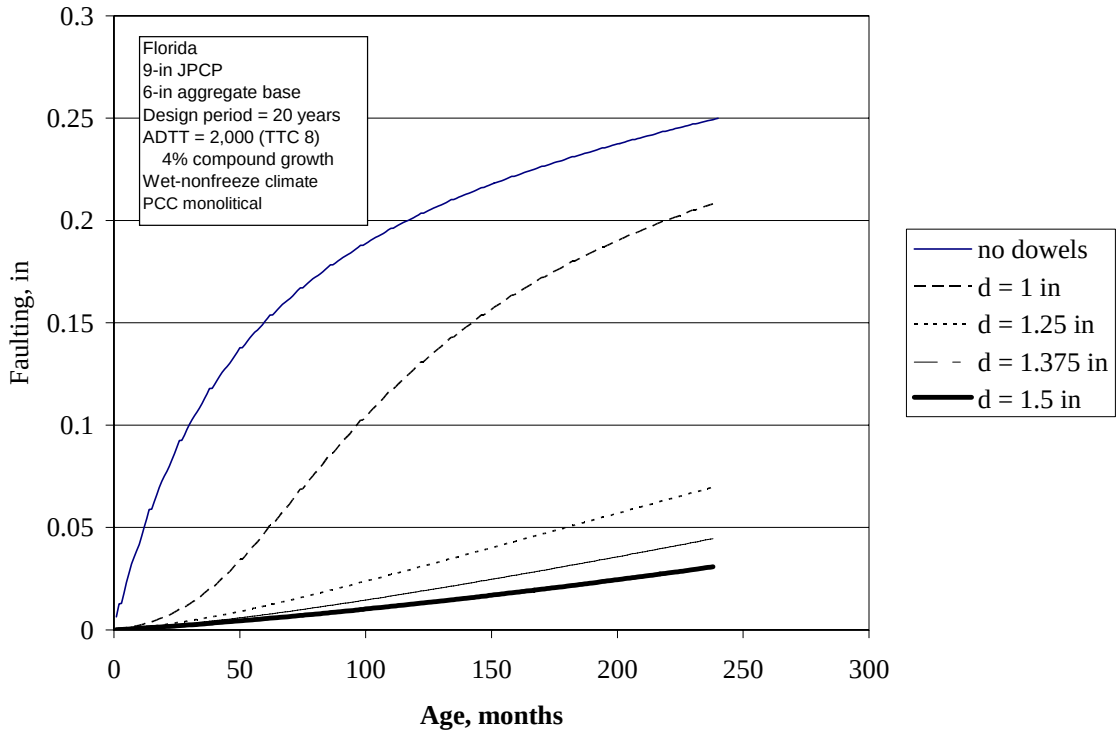


Figure 25. Faulting prediction for Florida sections. PCC shoulder, constructed monolithically.

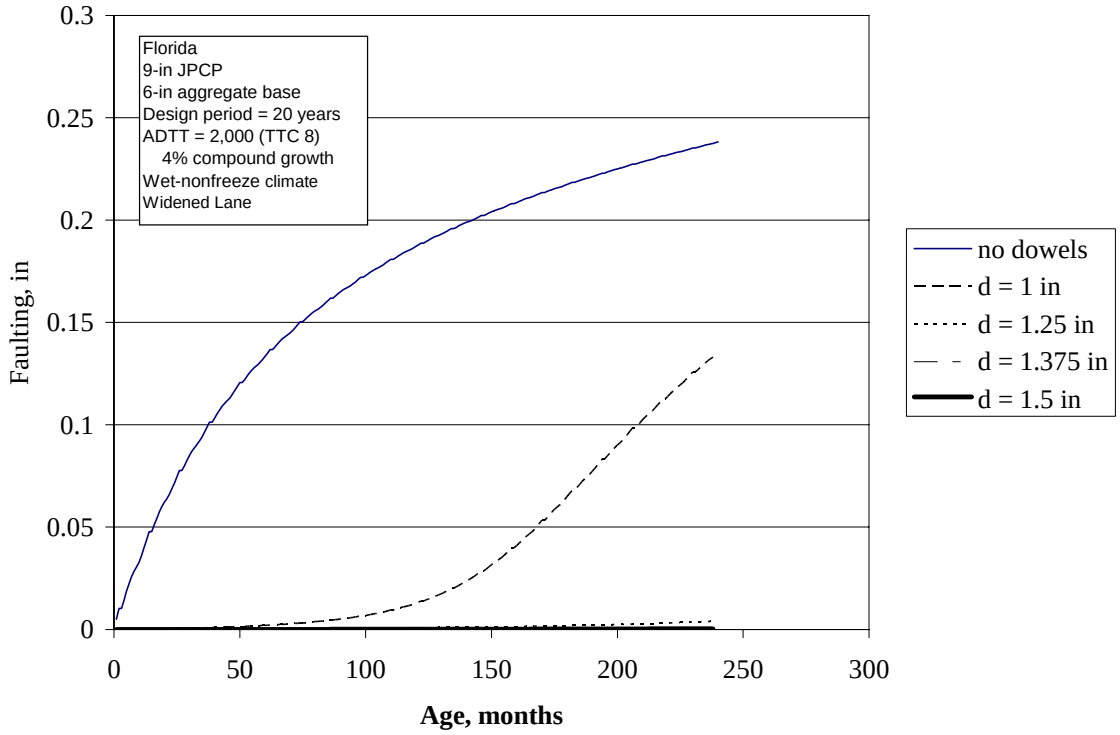


Figure 26. Faulting prediction for Florida sections. Widened lane, AC shoulder.

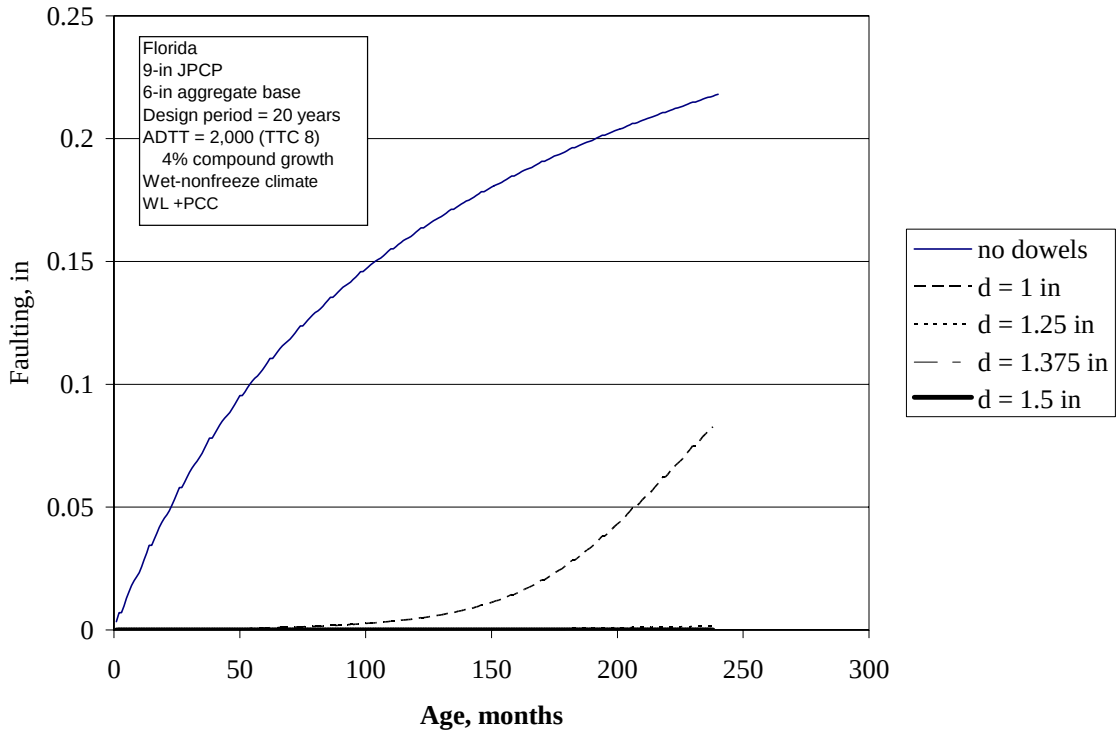


Figure 27. Faulting prediction for Florida sections. Widened lane, PCC shoulder.

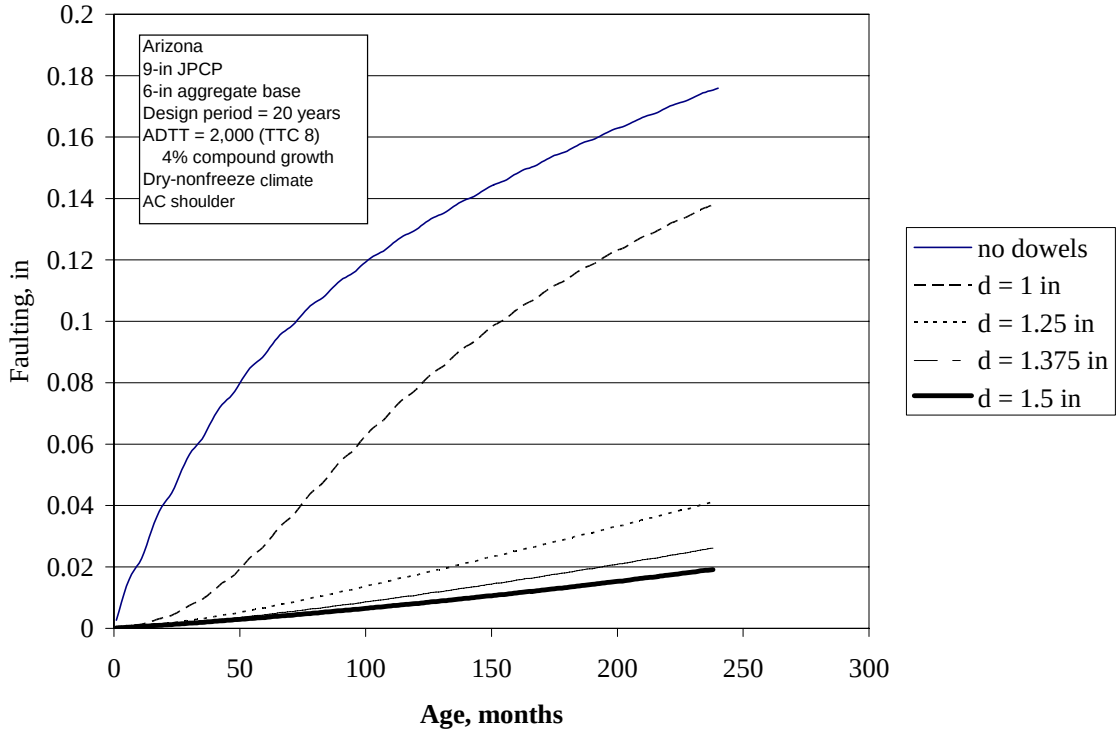


Figure 28. Faulting prediction for Arizona sections. AC shoulder.

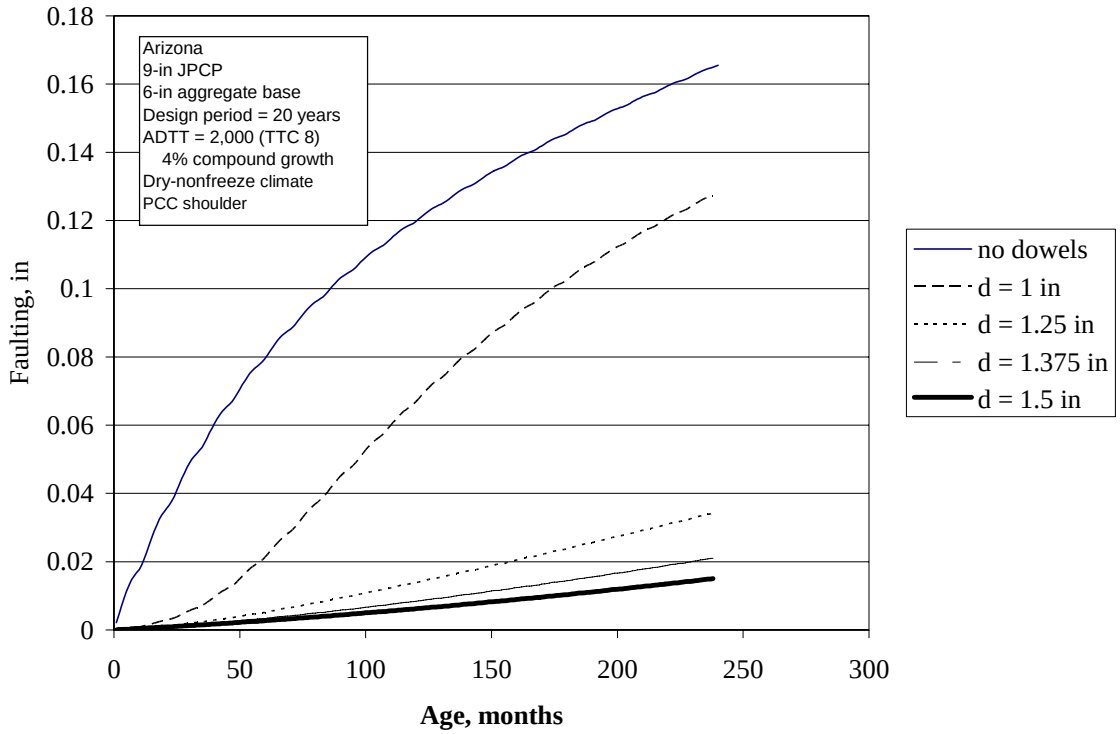


Figure 29. Faulting prediction for Arizona sections. PCC shoulder.

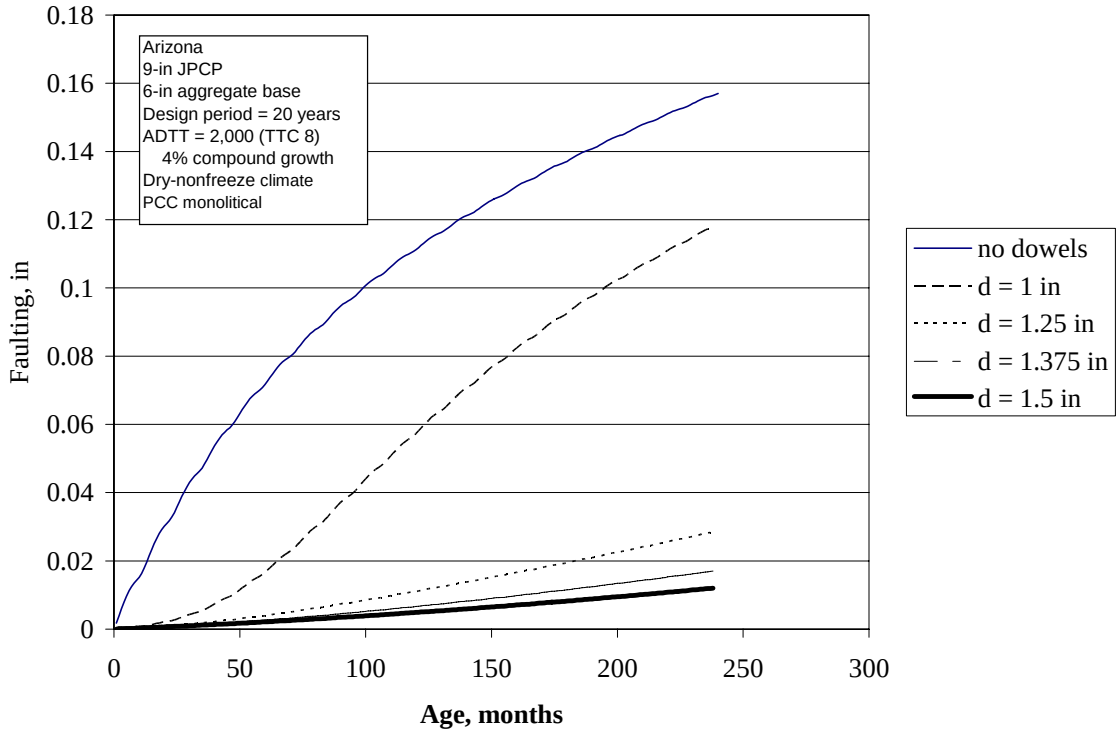


Figure 30. Faulting prediction for Arizona sections. PCC shoulder, constructed monolithically.

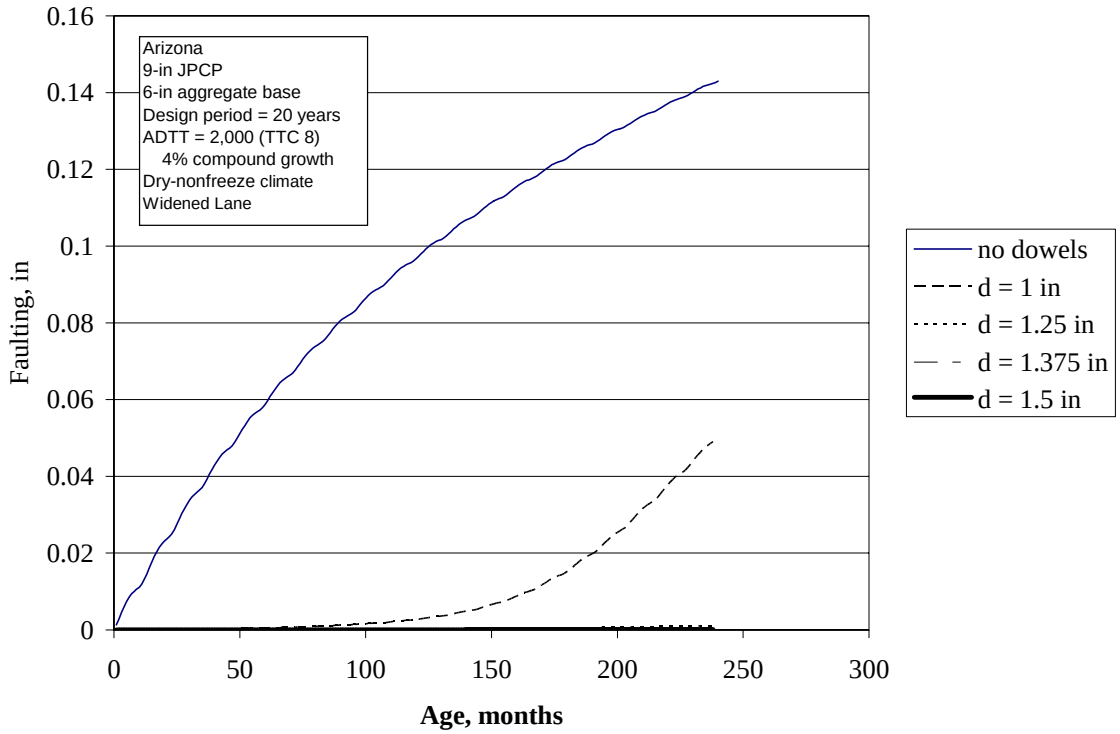


Figure 31. Faulting prediction for Arizona sections. Widened lane, AC shoulder.

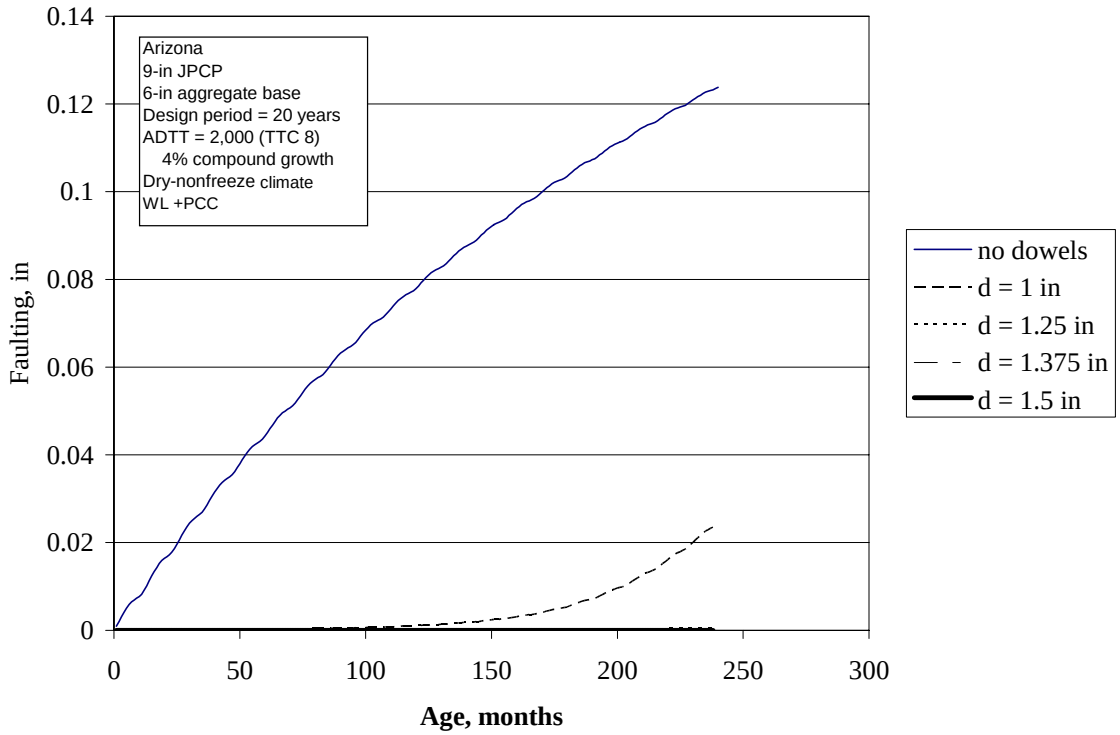


Figure 32. Faulting prediction for Arizona sections. Widened lane, PCC shoulder.

Joint spacing has a great impact on predicted faulting. Figure 33 demonstrates that an increase of joint spacing for a 9-in PCC pavement section with 1-in dowels leads to a significant increase in predicted faulting.

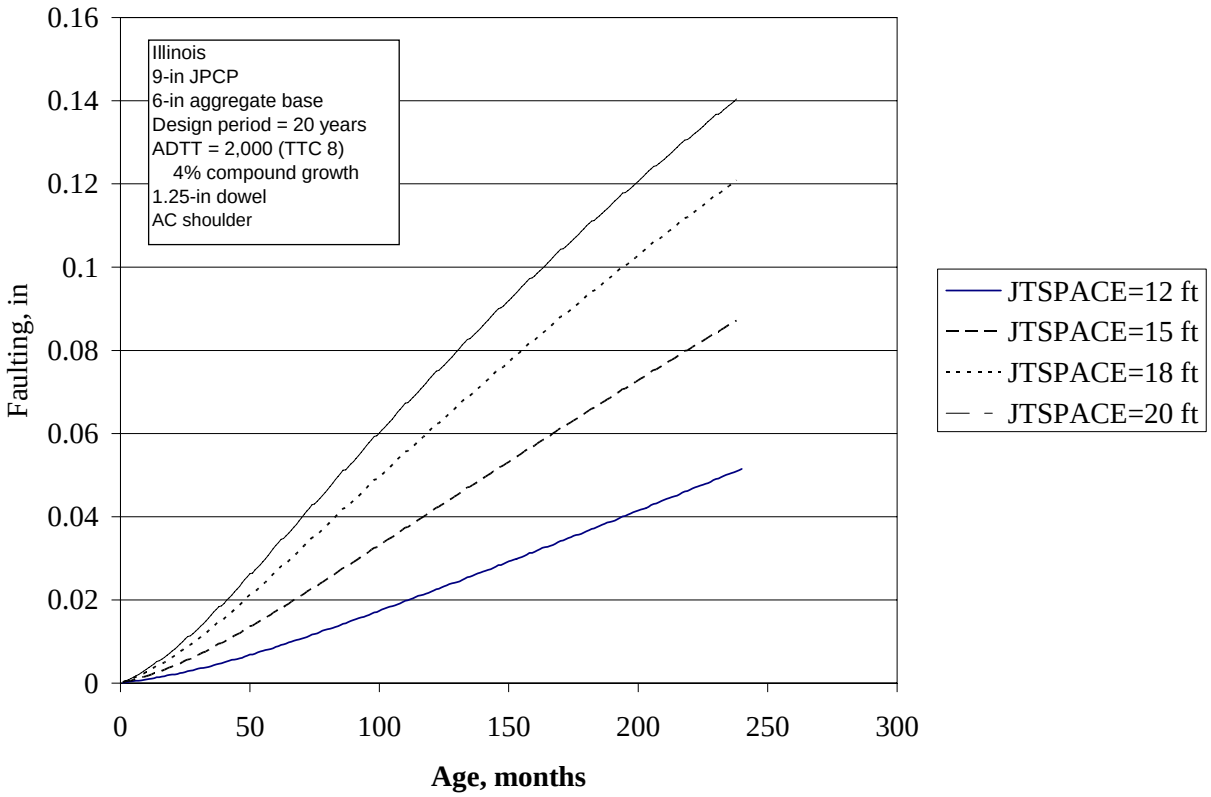


Figure 33. Effect of joint spacing on faulting prediction.

Construction practices also significantly affect pavement performance. Figures 34 and 35 show the effect of built-in curling and zero-stress temperature on long-term faulting prediction. A decrease in built-in temperature gradient from -6°F to -14°F increases predicted faulting more than three times. A decrease in zero-stress temperature also leads to lower faulting, although the effect is not as pronounced.

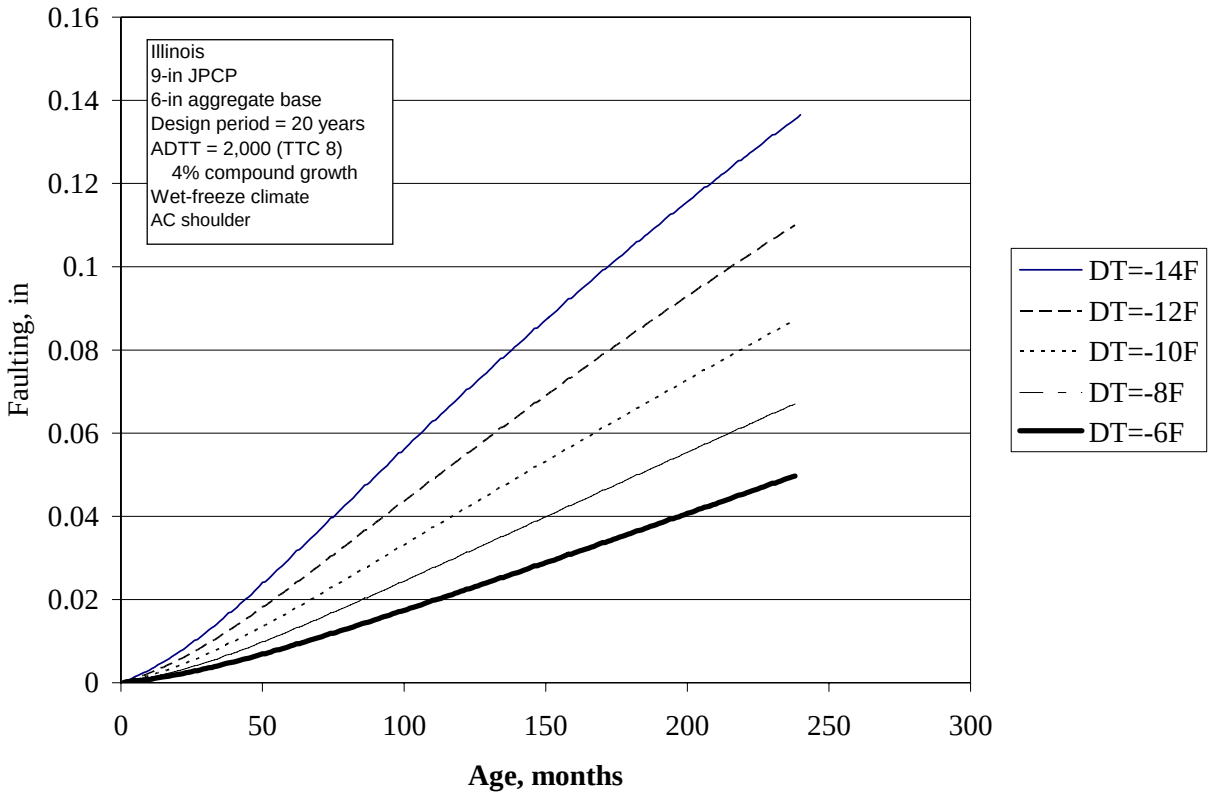


Figure 34. Effect of built-in curling on faulting prediction.

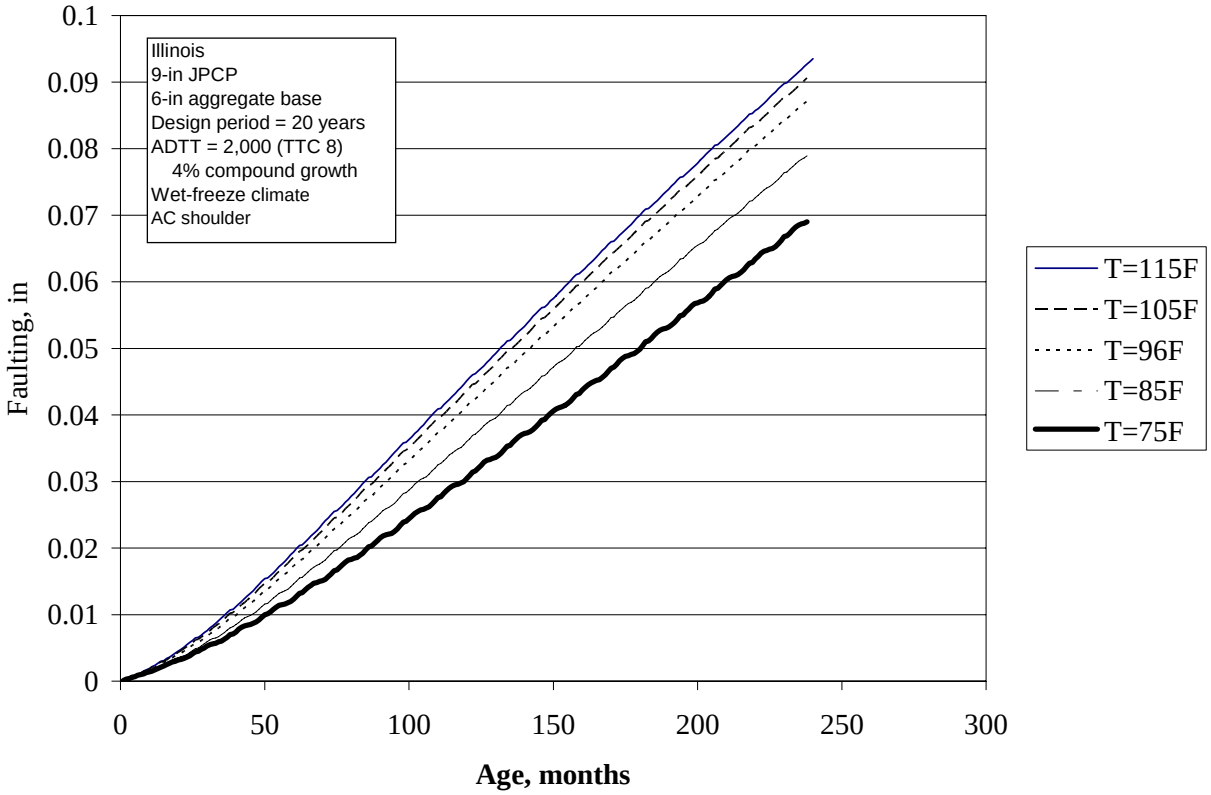


Figure 35. Effect of zero-stress temperature on faulting prediction.

Increasing base erodibility is another effective way to combat faulting. Figure 36 presents a comparison of faulting prediction for a nondoweled Illinois section for different levels of erodibility. A cement treated base was analyzed for EROD indexes of 1, 2, and 3. A granular base was used for EROD indexes of 4 and 5. One can see that an increase in erodibility index from 1 (Extremely Resistant) to 5 (Very Erodible) leads to an increase in predicted faulting.

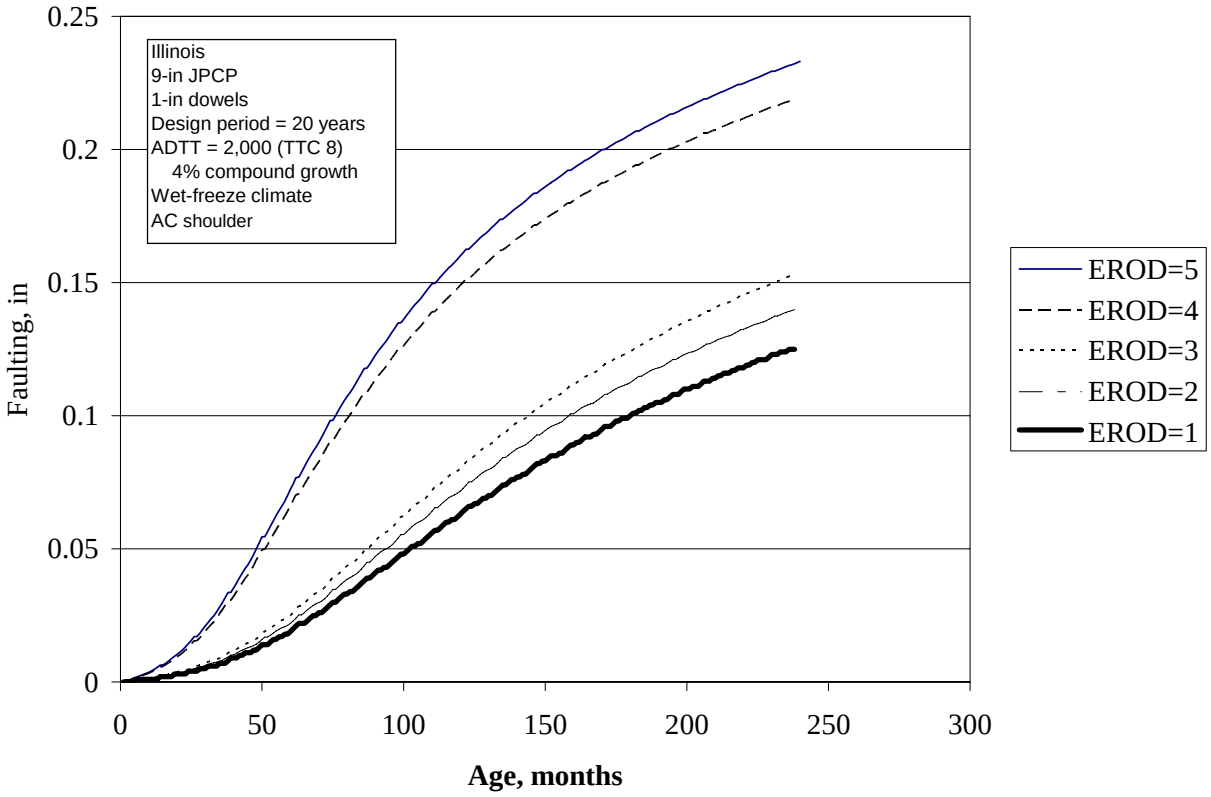


Figure 36. Effect of base erodibility on faulting prediction.

The effect of PCC thickness on faulting prediction is more complicated. To demonstrate this effect, several pavement sections located in California were considered. The following design parameters were used in this analysis:

- PCC slab thickness – 9, 10, or 12 in
- Base type – cement treated base (EROD=2)
- Base thickness – 6 in
- Joint spacing – 15 ft
- Subgrade type – A-7-6
- Design period – 20 years
- Cumulative number of heavy trucks – 77.5 million (about 143 million ESALs)
- PCC built-in curling -10$^{o}$F
- Construction month - September

Figures 37 and 38 present a comparison of predicted faulting for nondoweled and doweled joints, respectively. An increase in PCC slab thickness decreases joint faulting for nondoweled pavements; however, the picture is more complex for doweled pavements. As can be observed from figure 38, an increase in PCC thickness from 9 to 10 in decreases faulting almost negligibly. On the other hand, an increase in PCC thickness from 10 to 12 in leads to higher faulting because an increase in PCC thickness leads to a decrease in the ratio of dowel cross-section to PCC cross-section which, in turn, reduces dowel shear effectiveness. Thus, an increase in PCC thickness may require an increase in dowel diameter.

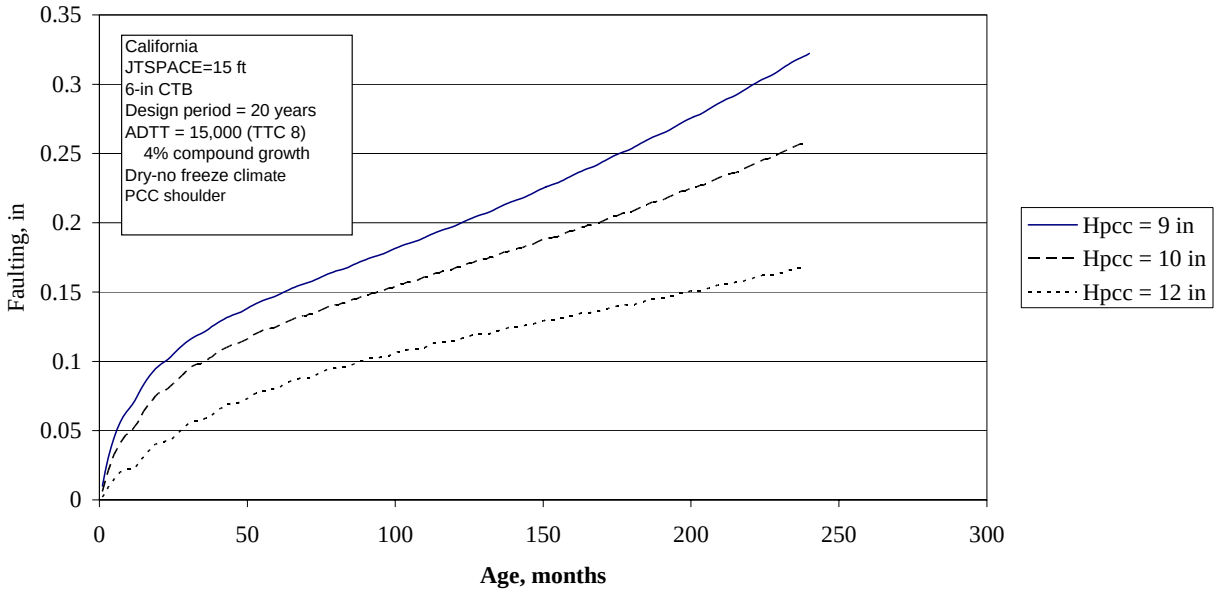


Figure 37. Effect of PCC thickness on predicted faulting in non-doweled JPCP.

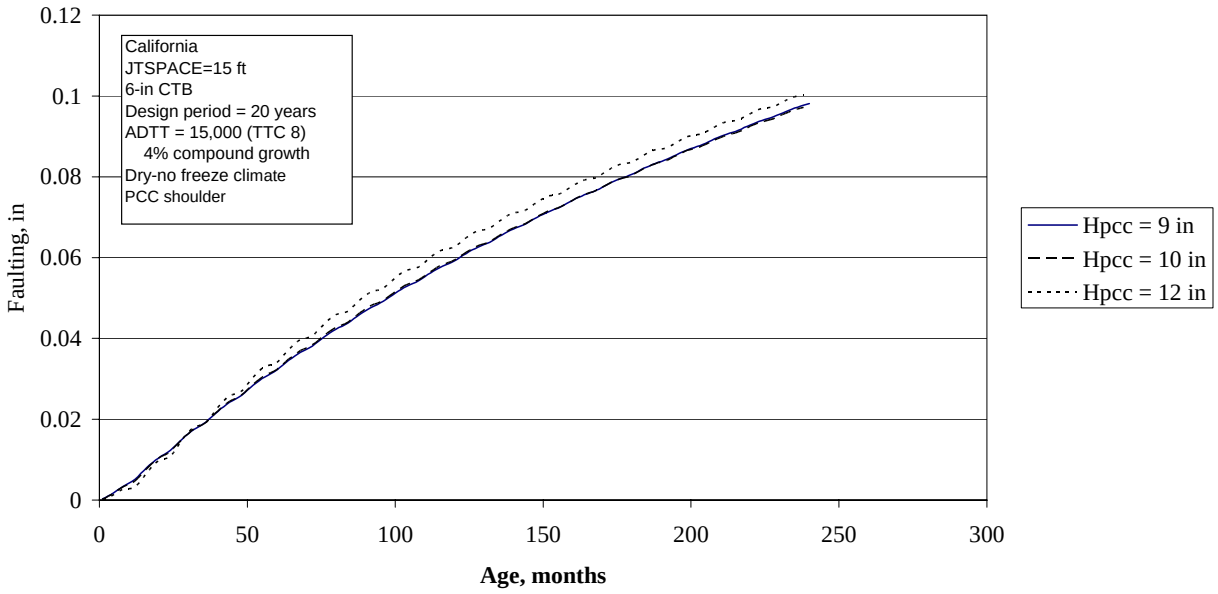


Figure 38. Effect of PCC thickness on predicted faulting in doweled JPCP.

## DEVELOPMENT OF RELIABILITY PREDICTION PROCEDURE

The definition of reliablity for joint faulting for a given project under design is as follows:

$$R = P [ \text{ Faulting of design project} < \text{Critical Level of Faulting } ] \quad (49)$$

Faulting of the design project depends on many factors but specifically the design of the pavement and joints, subdrainage, traffic, climate, construction quality particularly of the joints, climate during construction, and other factors. Faulting is a stochastic variable whose prediction is uncertain; however, it does follow some type of distribution and is bounded by practical conditions.

This section summarizes the development of the joint faulting design reliability procedure. This porcedure is based on analysis of the predicted versus measured faulting (see figure 11) and estimation of parameters of the corresponding error distribution.

### Step 1. Group all data points by the level of predicted faulting

All data points in the calibration database were divided into subgroups based on the level of predicted faulting. The following groups were established after inspection of the data plots showing the residual (predicted – measured) on the y-axis versys predicted faulting on the x-axis:

Table 10. Definition of faulting groups

| Group | Range of predicted faulting, in | Number of data points |
|---|---|---|
| 1 | 0 – 0.01 | 324 |
| 2 | 0.01 – 0.03 | 41 |
| 3 | 0.03 – 0.1 | 114 |
| 4 | 0.075 – 306 | 85 |

### Step 2. Compute descriptive statistics for each group of data

For each predicted faulting group, the following paramaters were computed:

- Mean predicted faulting, in
- Mean measured faulting, in
- Standard deviation of measured faulting, STDMeas, in

These parameters are presented in table 11.

Table 11. Computed statistical paramaters for each faulting group.

| Group | Mean Predicted Faulting, in | Mean Measured faulting | Standard Deviation of Measured Faulting |
|---|---|---|---|
| 1 | 0.001617901 | 0.006947699 | 0.012856231 |
| 2 | 0.018726829 | 0.021961857 | 0.02200075 |
| 3 | 0.061681579 | 0.070135091 | 0.049565217 |
| 4 | 0.125216471 | 0.120777832 | 0.06358652 |

Figure 39 shows very good correpondence between predicted and mean measured faulting for each group.

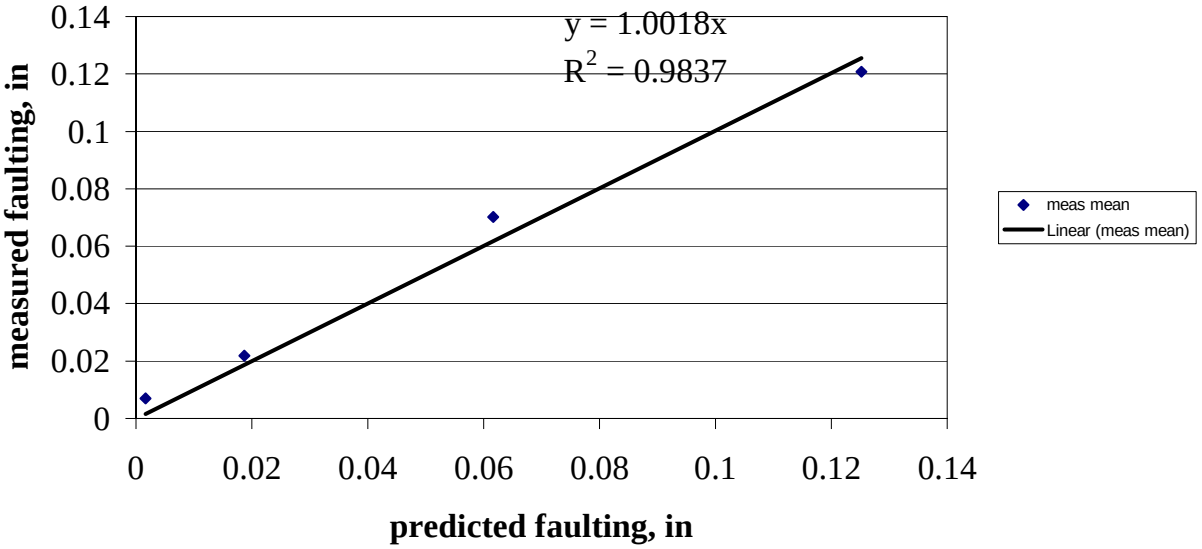


Figure 39. Comparison of mean predicted vs. mean measured for each group.

**Step 3. Determine relationship standard deviation of the measured faulting and predicted faulting.**

Based on data from table 11, the following relationship between measure standard deviation and predicted faulting was identified:

$$STD = \sqrt{0.03261\,Fault\_Meas + 0.00009779} \qquad (50)$$

Where

| | | |
|---|---|---|
| STDMeas | = | Measured standard deviation. |
| FAULT | = | Predicted faulting, in. |
| R^2 | = | 98.1% |
| N | = | 4 |

Figure 40 presents a comparison between predicted and measured standard deviations.

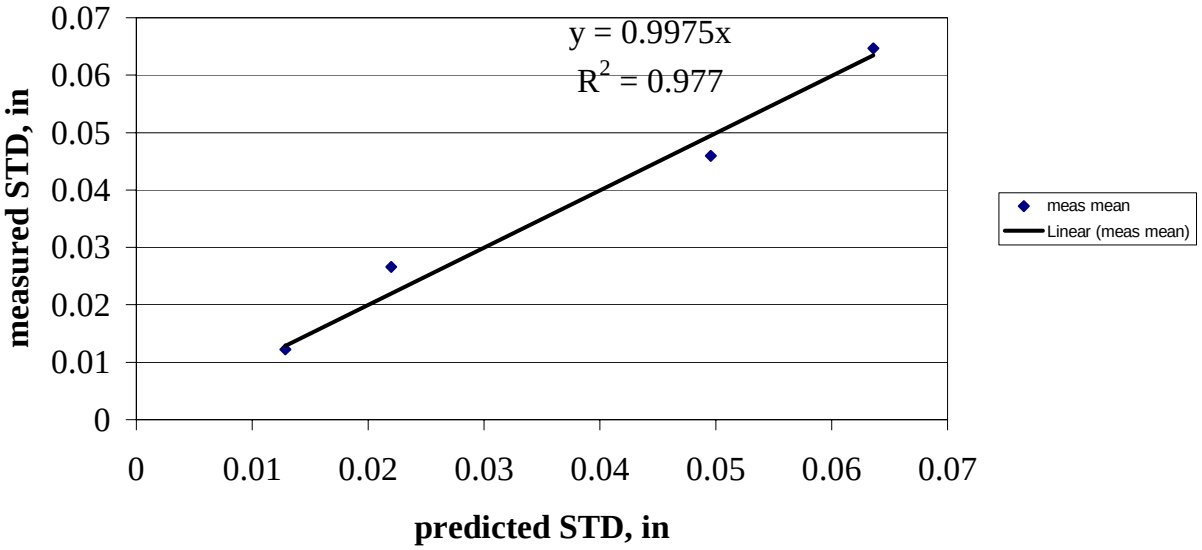


Figure 40. Predicted vs. measured standard deviations.

Many pages of discussion could be written on what the STDMeas actually represents in terms of all the sources of variation of mean project joint faulting. It includes, amoung other sources, at least the following variation:

- Measurement error associated with faulting testing (this could be removed).
- Error associated with any inaccuracies in estimating the many inputs (PCC strength, layer thickness, built-in curling and zero stress temperature, erosion of base, traffic loads, climate over life, and so on) for each of the calibration sections (while Level 1 inputs were used for many inputs, others required Level 2 or 3 because data were not available).
- Error associated with the faulting prediction algorithms used in the 2002 faulting models.

**Step 4. Reliability prediction**

Equation 50 permits a reliability analysis for joint faulting to be conducted based on the results of the deterministic analysis of faulting. The reliability analysis involves the following steps:

1. Using the faulting model, predict the faulting level over the design period using mean inputs to the model. This corresponds approximately to a "mean" joint faulting due to symmetry of residuals.
2. Adjust mean faulting for the desired reliability level using the following relationship:

$$FAULT\_P = FAULT\_mean + STDmeas * Zp \qquad (51)$$

Where

FAULT_P = Faulting level corresponding to the reliability level p.
FAULT = Fauting predicted using the deterministic model with mean inputs (corresponding to 50 percent reliability).

| | | |
|---|---|---|
| STDmeas | = | Standard deviation of fauting corresponding to fauting predicted using the deterministic model with mean inputs. |
| Zp | = | Standardized normal deviate (mean 0 and standard deviation 1) corresponding to reliability level p. |

Figure 41 shows predicted faulting for different reliability levels for the Illinois section. One can see that an increase in reliability level leads to a reasonable increase in predicted faulting. If a pavement designer wants a 90 percent reliability for joint faulting, then the predicted 90 percent curve must not exceed some preselected critical value of joint faulting. This level should be selected by the designer prior to conducting the pavement design.

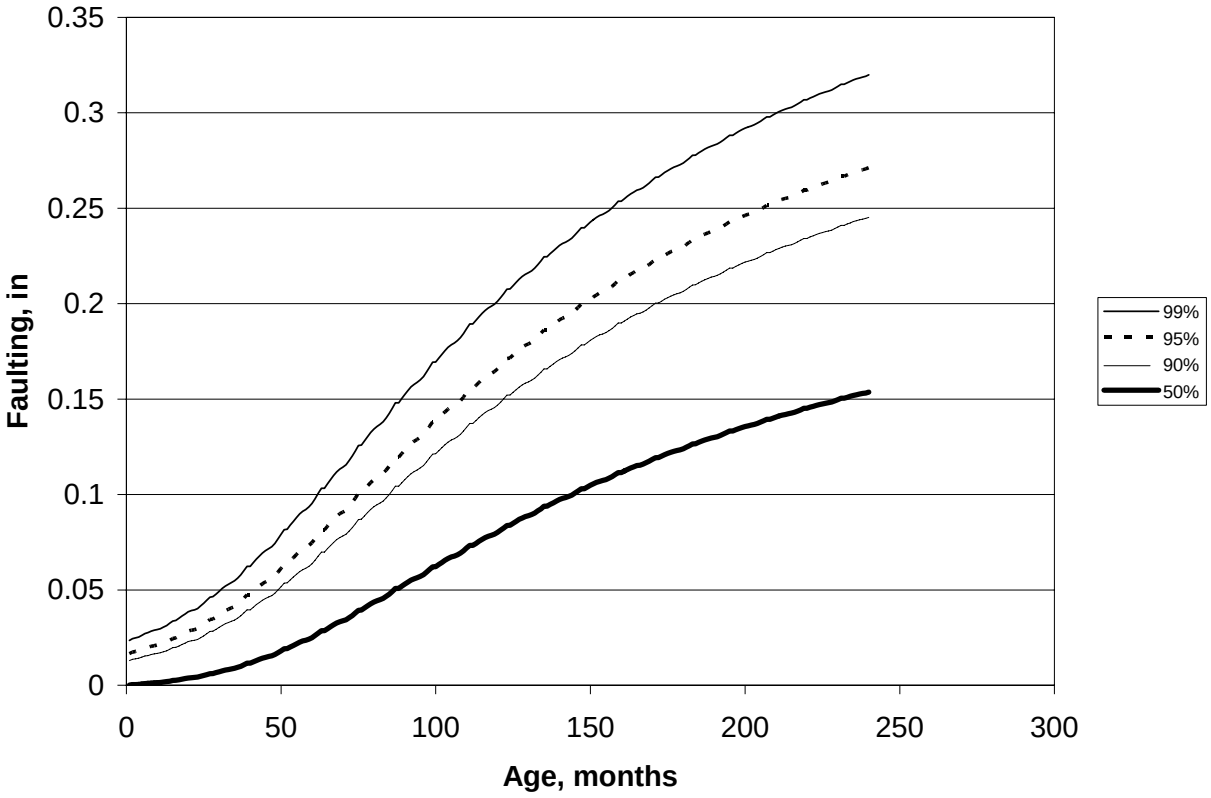


Figure 41. Effect of reliability level on faulting prediction.

## STEP-BY-STEP PROCEDURE

Presented in this section is the step-by-step procedure for predicting JPCP transverse joint faulting. The steps involved include the following:

1. Tabulate input data – summarize all inputs needed for predicting JPCP transverse joint faulting.
2. Process input data and initialize parameters
3. Determine initial maximum faulting
4. Determine PCC free shrinkage strains
5. Calculate joint LTE
6. Calculate effective slab parameters
7. Calculate effective temperature gradient
8. Compute adjusted load/pavement weight ratios (normalized loads)
9. Compute critical deflections
10. Compute differential energy increment deflections
11. Find faulting increment
12. Find current faulting
13. Find current maximum faulting index
14. Evaluate loss of aggregate shear capacity
15. Calculate damage of doweled joins

Although some of the equations for faulting predictions have been presented above, they will be repeated as necessary, for the reader's convenience.

### Step 1: Tabulate input data

The 2002 Design Guide software conducts faulting analysis after execution of the traffic module, EICM module, and determination of the equivalent coefficient of subgrade reaction for each month. The required parameters for faulting predictions are prepared and tabulated by the software. These parameters are summarized in table 12.

### Step 2. Process input data and initiate parameters

Step 2.1 Process PCC temperature data

The EICM analysis performed prior to the faulting program generates PCC temperatures at 11 points throughout PCC thickness for each hour of the pavement life after construction. For the faulting analysis, these data are reduced to the following parameters:

- Mean PCC mid-depth night temperature for each month of a year calculated as mean temperature for at the PCC slab mid-depth which occur in a certain month from 8 p.m. to 8 a.m. over the pavement design life.

- Mean nighttime temperature difference between PCC slab top and bottom surfaces for each month of a year calculated as mean difference of temperature between PCC top and bottom surfaces which occur in a certain month from 8 p.m. to 8 a.m. over the pavement design life.
- Base freezing index - percentage of time the bottom of the PCC slab temperature was below 32 $^{o}$F.

Table 12. Summary of input parameters for JPCP transverse joint faulting prediction.

| Input | Variation* | Source |
|---|---|---|
| Design life (months) | Fixed | Direct design input |
| Month of project opening | Fixed | Direct design input |
| PCC age at opening (mo) | Fixed | Direct design input |
| PCC strength for each month (psi) | Design mo | Result of PCC strength input processing (section 3.4.3.6 *Pavement Structure Input*) |
| PCC modulus for each month (psi) | Design mo | |
| Joint spacing (ft) | Fixed | Direct design input |
| Dowel diameter (in) | Fixed | Direct design input |
| Lane-shoulder deflection LTE (%) | Fixed | Direct design input |
| Widened slab (yes/no) | Fixed | Direct design input |
| Poisson's ratio | Fixed | Direct design input |
| PCC unit weight (pcf) | Fixed | Direct design input |
| Coefficient of thermal expansion (/°F) | Fixed | Direct design input |
| Ultimate shrinkage strain ($10^{-6}$) | Fixed | Direct design input |
| Reversible shrinkage strain ($10^{-6}$) | Fixed | Direct design input |
| Time to 50% ult. shrinkage (days) | Fixed | Direct design input |
| Base thickness (in) | Fixed | Direct design input |
| Base unit weight (pcf) | Fixed | Direct design input |
| Monthly base modulus (psi) | Calendar mo | Result of Seasonal Analysis (section 3.4.3.6 *Pavement Structure Input*) |
| Base erodibility | Fixed | Direct design input |
| Monthly effective subgrade k-value (psi/in) | Calendar mo | Results of "E-to-k" conversion (section 3.4.3.6 *Pavement Structure Input*) |
| Permanent curl/warp (°F) | Fixed | Direct design input |
| PCC zero-stress temperature | Fixed | Direct design input or estimated from construction month and cement content |
| Lane width (ft) | Fixed | Direct design input |
| Mean wheel path (in) | Fixed | Direct design input |
| Traffic wander standard deviation (in) | Fixed | Direct design input |
| Axle load spectrum for each month of pavement life | monthly | Results of traffic analysis |
| Slab width (ft) | Fixed | Direct design input |

* Design mo: parameters that vary with pavement age; Calendar mo: parameters that vary seasonally.

Step 2.2 Determine maximum and average mean monthly relative humidity

The EICM analysis provides mean ambient relative humidity for each month of a year. From these values, the maximum value should be determined.

$$RH_{\max} = \max(RH_m), \qquad m = 1,12$$
$$RH_{average} = \frac{1}{12}\sum_{m=1,12} RH_m \tag{52}$$

where:

$RH_{\max}$ = maximum ambient relative humidity

$RH_{average}$ = average yearly ambient relative humidity

$RH_m$ = average monthly ambient relative humidity for month m.

Step 2.3 Determine base LTE for each month

The base LTE for each month depends on base type and the mean PCC temperature at the PCC mid-depth. If for a certain month the PCC mid-depth temperature is less than 32 $^{o}$F, then the base LTE is assigned to be 90 percent; otherwise it is determined based on the base type from table 7.

Step 2.4 Determine shoulder-lane LTE for each month

The shoulder-lane base LTE for faulting analysis is determined from the user-provided shoulder–lane LTE input. Considering that the LTE at nighttime near a transverse joint is lower than daytime LTE at mid-slab, shoulder LTE for the faulting analysis is reduced using the following equation:

$$LTE_{sh} = 5 + \frac{LTE_{shoulder,input}}{2} \tag{53}$$

where

$LTE_{sh}$ = Shoulder/lane deflection LTE used in faulting analysis.

$LTE_{shoulder,input}$ = User-provided shoulder/lane deflection LTE.

Step 2.5 Set initial parameters

Set initial values for the aggregate joint initial shear capacity, dowel damage, dowel joint stiffness, aggregate interlock damage, and aggregate interlock stiffness using the following equations:

$$\Delta s_{tot} = 0 \tag{54}$$
$$J_0 = \frac{38.20 A_d}{h_{PCC}} \tag{55}$$

$$DOWDAM_0 = 0 \tag{55}$$

$$J^*_d = \begin{cases} 118, & if \ \dfrac{A_d}{h_{PCC}} > 0.835 \\ 52.52\dfrac{A_d}{h_{PCC}} - 19.8, & if\ 0.039 \le \dfrac{A_d}{h_{PCC}} \le 0.835 \\ 0.4, & if \ \dfrac{A_d}{h_{PCC}} < 0.039 \end{cases} \tag{56}$$

where

$S_o$ = Initial cumulative loss of shear capacity of the aggregate joint.

$DOWDAM_0$ = Initial damage of dowel/PCC contact.

$J_0$ = Initial nondimensional dowel stiffness.

$J^*_d$ = Critical initial nondimensional dowel stiffness.

$A_d$ = Area of dowel cross-section:

$$A_d = \frac{\pi d^2}{4} \tag{57}$$

d = dowel diameter

**Step 3. Determine initial maximum faulting**

Step 3.1 Find effective slab thickness

Using representative PCC modulus of elasticity (modulus of elasticity at the end of the first year after opening of the pavement to traffic, find effective slab thickness for every month, m, to account for seasonal variation in the base modulus.

$$H_{eff,m} = \sqrt{h_{PCC}^2 + \frac{E_{BASE,m}}{E_{PCC}} H_{BASE}^2} \qquad m = 1,12 \tag{58}$$

where

$H_{eff,m}$ = Effective slab thickness.

$h_{PCC}$ = PCC slab thickness.

$H_{BASE}$ = Base thickness.

$E_{PCC}$ = Representative PCC modulus of elasticity

$E_{BASE,\,m}$ = Base modulus of elasticity for month m

Step 3.2 Calculate unit weight of the equivalent slab

The weight of a unit area of the effective slab should be equal to the weight of a unit area of the original two-layered (PCC slab and base). Since the base layer is assumed to be weightless, the weight of a unit area of the effective slab should be equal to the weight of a unit area of the PCC slab. However, since the effective slab thickness is different for different months then the unit weight of the effective slab should be adjusted as follows:

$$\gamma_{eff,m} = \frac{\gamma_{PCC} h_{PCC}}{H_{eff,m}} \qquad m = 1,12 \qquad (59)$$

where

$\gamma_{eff}$ = Effective unit weight.
$h_{PCC}$ = PCC slab thickness.
$\gamma_{PCC.}$ = PCC unit weight.
$h_{eff}$ = Effective thickness.

Step 3.3 Find radius of relative stiffness for this month

$$\ell_m = \sqrt[4]{\frac{E_{PCC} H_{eff,m}^3}{12(1-\mu^2)k_m}} \qquad (60)$$

$H_{eff,\,m}$ = Effective slab thickness for month m.
$E_{pcc}$ = PCC modulus of elasticity for this month.
$\mu$ = PCC Poisson's ratio.
$k_{eff,\,m}$ = Coefficient of subgrade reaction for this month.

Step 3.4 Calculate reversible shrinkage contribution to long-term curling

Seasonal variations in relative humidity cause changes in slab curling. This can be described through an equivalent temperature gradient that would cause the same deflection basin. Calculation of the effective temperature gradient involves the following steps:

*Step 3.4.1 Determine free shrinkage strains if the relative is equal to the average relative humidity*

For each month, free shrinkage strain of an old concrete pavement would be determine using the following equation:

$$\varepsilon_{sh,average}(t) = \begin{cases} \varepsilon_{su} \cdot (1.4 - 0.01 * RH_{averagex}), & if\ RH_{average} < 80 \\ \varepsilon_{su} \cdot (3 - 0.03 * RH_{average}), & if\ RH_{average} \geq 80 \end{cases} \qquad (61)$$

where

$\varepsilon_{sh,\,average}$ = Shrinkage strain for the average relative humidity, x $10^{-6.}$
$\varepsilon_{sh}$ = Ultimate shrinkage strain for the relative humidity equal to 40. percent (discussed in section 2.6.1), x $10^{-6.}$
$RH_{average}$ = Average mean monthly ambient relative humidity, percent.

*Step 3.4.2 Determine free shrinkage stress as if the relative humidity is equal to the relative humidity of the driest month using equations from section 2.2.6.2 of the Design Guide:*

$$\varepsilon_{sh,m}(t) = \begin{cases} \varepsilon_{su} \cdot (1.4 - 0.01 * RH_m), & if\ RH_m < 80 \\ \varepsilon_{su} \cdot (3 - 0.03 * RH_m), & if\ RH_m \geq 80 \end{cases} \qquad m = 1, \quad 12 \qquad (62)$$

where

$\varepsilon_{sh,\,m}$ = Free shrinkage strain for the mean relative humidity of month m, x $10^{-6}$.
$\varepsilon_{sh}$ = Ultimate shrinkage strain for the relative humidity equal to 40 percent (discussed in section 2.6.1), x $10^{-6}$.
$RH_m$ = Ambient relative humidity for month m, percent.

*Step 3.4.3 Calculate shrinkage contribution to curling*

Moisture warping is adjusted seasonally based on atmospheric relative humidity as follows:

$$\Delta T_{SH,m} = \frac{3 \cdot \varphi \cdot (\varepsilon_{h,m} - \varepsilon_{h,\,average}) \cdot h_s \cdot \left( \frac{h_{PCC}}{2} - \frac{h_s}{3} \right)}{\alpha \cdot h^2 \cdot 100} \qquad (63)$$

where,

$\Delta T_{SH,m}$ = Temperature gradient equivalent of moisture warping for month i, °F.
$\varphi$ = Reversible shrinkage factor, fraction of total shrinkage. Use 0.5 unless more accurate information is available.
$\varepsilon_{su}$ = Ultimate shrinkage (equation 2.2.25 of PART 2, Chapter 2 of the Design Guide), x $10^{-6}$.
$RH_{hi}$ = Average relative humidity for month i, percent.
$S_{h\,ave}$ = Annual average relative humidity, percent.
$h_s$ = Depth of the shrinkage zone (typically 2 in).
$h_{PCC}$ = PCC slab thickness, in.
$\alpha$ = PCC coefficient of thermal expansion, in/in/°F.

<u>Step 3.5 Calculate effective temperature differential</u>

Equivalent temperature differential is determined from equation:

$$\Delta T_{eff,m} = \frac{h_{PCC}^2}{H_{eff}^2} * \left[ (T_{top,m} - T_{bot,m}) + \Delta T_{BI} + \Delta T_{sh,m} \right] \qquad m = 1,12 \qquad (64)$$

where

| | | |
|---|---|---|
| $\Delta T_{eff, m}$ | = | Difference between temperatures at the top and bottom surfaces of the effective slab for month m. |
| $T_{top, m,}$ | = | Mean night temperature of the top PCC surface for month m. |
| $T_{bot, m,}$ | = | Mean night temperature of the bottom PCC surface for month m. |
| $\Delta T_{BI}$ | = | Built-in curling and temperature shrinkage temperature differential. |
| $\Delta T_{sh, m,}$ | = | Equivalent temperature differential due to reversible portion of shrinkage. |
| $h_{PCC}$ | = | PCC thickness. |
| $H_{eff}$ | = | Effective thickness computed. |

Step 3.6. Compute Korenev's nondimensional temperature gradient

$$\phi_m = \frac{2\,\alpha_{PCC}\,(1+\mu_{PCC})\ell_m^2}{H_{eff,m}^{\ 2}} \frac{k_m}{\gamma_{eff,m}} \Delta T_{eff,m} \qquad (65)$$

where

| | | |
|---|---|---|
| $\phi_m$ | = | Nondimensional temperature gradient for month m. |
| $h_{PCC}$ | = | PCC slab thickness. |
| $\alpha_{PCC}$ | = | PCC coefficient of thermal expansion. |
| $\mu_{PCC}$ | = | Poisson's ratio for PCC. |
| $\gamma_{eff}$ | = | Effective unit weight for month m. |
| k | = | Modulus of subgrade reaction (k-value) for month m. |
| $\ell_m$ | = | Radius of relative stiffness for month m. |
| $\Delta T_{eff, m}$ | = | Effective temperature gradient for month m. |

Step 3.7 Compute corner deflections due to temperature curling

Using neural networks, compute deflections in the equivalent slab system due to temperature curling only. This deflection is defined as a difference between the deflection due to temperature curling and self weight and deflection due to self weight only.

$$\delta_{curl.m} = \frac{34100596.7 h_{eff,m}}{\ell_m^4\ k_m} \left[ NN_c(JTSpace, \ell_m, \phi_m) - NN_c(JTSpace, \ell_m, 0) \right] \qquad (66)$$

where

| | | |
|---|---|---|
| $\delta_{curl,m}$ | = | Corner deflection due to curling only. |
| JTSpace | = | Mean transverse joint spacing. |
| $\ell_m$ | = | Radius of relative stiffness for month m. |

$\phi_m$ = Nondimensional temperature gradient for month m.

$NN_c(JTSpace, \ell_m, \phi_m)$ = Neural network trained to determine corner deflections due to slab curling only (no axle loading)

Step 3.8. Determine maximum corner deflection

Determine maximum deflections from the twelve deflections computed in step 3.7:

$$\delta_{curl,\max} = \max_{m=1,12} \delta_{curl,m}$$

$\delta_{curl,m}$ = Corner deflection due to curling only for month m.

$\delta_{curl,\max}$ = Maximum corner deflection due to curling.

Step 3.9. Determine overburden pressure

$$p_s = h_{PCC}\gamma_{PCC} + h_{base}\gamma_{base} \quad (67)$$

where

$p_s$ = Overburden pressure.

$h_{PCC}$ = PCC slab thickness.

$\gamma_{PCC}$ = PCC unit weight.

$h_{base}$ = PCC slab thickness.

$\gamma_{base}$ = PCC unit weight.

Step 3.10. Determine maximum initial faulting

$$FMAX_0 = C_{12} * \delta_{eff,\max} * \left[ Log \frac{P200 * WetDays}{p_s} Log(1 + C_5 * 5^{EROD}) \right]^{C_6} \quad (68)$$

Where

| | | |
|---|---|---|
| $FMAX_0$ | = | Initial maximum faulting. |
| P200 | = | Percent subgrade material passing 0.075-mm (#200) sieve. |
| EROD | = | Erodibility of the base layer. |
| WetDays | = | Number of wet days per year. |
| $\delta_{eff,\max}$ | = | Maximum corner deflection due to curling. |

$C_{12} = C_1 + C_2 * FR^{0.25}$

FR = base freezing index

$C_1$, $C_2$, $C_5$, and $C_6$ are calibration parameters:

$C_1$ = 1.29

$C_2$ = 1.1

$C_5$ = 250

$C_6$ = 0.4

Steps 4 through 15 should be repeated for each month of the pavement design life.

**Step 4. Determine PCC free shrinkage strains**

Step 4.1 Determine PCC age

Determine PCC age in days using the following equation:

$$t = 30.4 * (MONTH + MOPEN) \quad (69)$$

where

| | | |
|---|---|---|
| t | = | Average PCC age for this month, days. |
| MONTH | = | Pavement age from the traffic opening, month. |
| MOPEN | = | Pavement age at the opening to traffic. |

Step 4.2 Determine free shrinkage stress as if the relative is equal to the relative humidity of the driest month using equations from section 2.2.6.2 of the Design Guide

$$\varepsilon_{sh.\max}(t) = \begin{cases} \varepsilon_{su} \cdot \frac{t}{n+t} \cdot (1.4 - 0.01 * RH_{\max}) & if\ \mathrm{RH}_{\max} < 80 \text{ percent} \\ \varepsilon_{su} \cdot \frac{t}{n+t} \cdot (3 - 0.03 * RH_{\max}) & if\ \mathrm{RH}_{\max} < 80 \text{ percent} \end{cases} \quad (70)$$

where

| | | |
|---|---|---|
| $\varepsilon_{sh,\max}$ | = | Shrinkage strain at time t days from placement, x $10^{-6.}$ |
| $\varepsilon_{su}$ | = | Ultimate shrinkage strain (discussed in section 2.6.1), x $10^{-6.}$ |
| t | = | Time since placement, days. |

| | | |
|---|---|---|
| n | = | Time to achieve 50 percent of ultimate shrinkage strain, days. Use n = 35, unless more accurate information is available. |
| $RH_{max}$ | = | Ambient relative humidity, percent. |

Step 4.3 Determine free shrinkage stress as if the relative humidity is equal to the relative humidity of the driest month using equations from section 2.2.6.2

$$\varepsilon_{sh,MONTH} = \begin{cases} \varepsilon_{su} \cdot \dfrac{t}{n+t} \cdot \left(1.4 - 0.01 * RH_{MONTH}\right) & if\ \mathrm{RH_a} < 80 \text{ percent} \\ \varepsilon_{su} \cdot \dfrac{t}{n+t} \cdot \left(3 - 0.03 * RH_{MONTH}\right) & if\ \mathrm{RH_a} < 80 \text{ percent} \end{cases} \quad (71)$$

where

| | | |
|---|---|---|
| $\varepsilon_{sh,\ MONTH}$ | = | Shrinkage strain at time t days from placement, x $10^{-6.}$ |
| $\varepsilon_{su}$ | = | Ultimate shrinkage strain (discussed in section 2.6.1), x $10^{-6.}$ |
| t | = | Time since placement, days. |
| n | = | Time to achieve 50 percent of ultimate shrinkage strain, days. Use n =3,unless more accurate information is available. |
| $RH_{MONTH}$ | = | Ambient relative humidity for this month, percent. |

Step 4.4 Determine total free shrinkage strain at the top surface of the PCC slab

$$\varepsilon'_{sh,MONTH} = \varepsilon_{sh,\max} - \left(\varepsilon_{sh,\max} - \varepsilon_{s,MONTH}\right) \cdot \varphi \quad (72)$$

where

| | | |
|---|---|---|
| $\varepsilon'_{sh,\ MONTH}$ | = | Shrinkage strain for month *i* at any time t days from placement, x $10^{-6.}$ |
| $\varepsilon_{sh,\ max}$ | = | Shrinkage strain for the driest month determined using eq. 2.2.29 from the Design Guide,x $10^{-6.}$ |
| $\varepsilon_{sh,\ MONTH}$ | = | Nominal shrinkage strain for month *i* determined using eq. 2.2.29 Design Guide, x $10^{-6.}$ |
| $\varphi$ | = | Reversible shrinkage factor, fraction of total shrinkage. Use 0.5 unless more accurate information is available. |

Step 4.5 Determine free shrinkage stress as if the relative humidity is equal to the relative humidity at the bottom of the PCC slab

$$\varepsilon_{sh,bot} = \begin{cases} \varepsilon_{su} \cdot \dfrac{t}{n+t} \cdot (1.4 - 0.01 * RH_{bot}) & if \ \text{RH}_{\text{bot}} < 80 \text{ percent} \\ \varepsilon_{su} \cdot \dfrac{t}{n+t} \cdot (3 - 0.03 * RH_{bot}) & if \ \text{RH}_{\text{bot}} < 80 \text{ percent} \end{cases} \quad (73)$$

where

$\varepsilon_{sh,\ bot}$ = Shrinkage strain at the bottom of the PCC slab for the current month, x $10^{-6.}$

$\varepsilon_{su}$ = Ultimate shrinkage strain (discussed in section 2.6.1), x $10^{-6.}$

t = Time since placement, days.

n = Time to achieve 50 percent of ultimate shrinkage strain, days. Use n = 35, unless more accurate information is available.

$RH_{bot}$ = PCC relative humidity at the bottom slab surface.

**Step 5. Calculate joint LTE**

Step 5.1 Calculate PCC aggregate LTE

*Step 5.1.1 Determine mean shrinkage strain (thought PCC slab)*

The average shrinkage strain, $\varepsilon_{sh,mean}$, is defined as follows:

$$\varepsilon_{sh,mean} = \varepsilon_{sh,bot} + (\varepsilon_{sh,MONTH} - \varepsilon_{sh,bot}) * \frac{h_d}{h_{PCC}} \quad (74)$$

where

$\varepsilon_{sh,,bot}$ = Free shrinkage strain at the bottom surface of the PCC slab.

$\varepsilon_{sh,MONTH}$ = Fee shrinkage strain at the top surface of the PCC slab.

$h_d$ = Depth of a drier portion of the PCC slab, in.

*Step 5.1.2 Determine overall joint opening*

$$jw = Max(12000 * STSpace * \beta * (\alpha_{PCC} * (T_{constr} - T_{mean}) + \varepsilon_{sh,mean}), 0) \quad (75)$$

where,

jw = Joint opening, mils (0.001 in).

$\varepsilon_{sh,mean}$ = PCC slab mean shrinkage strain.

$\alpha_{PCC}$ = PCC coefficient of thermal expansion, in/in/$^0$F.

JTSpace = Joint spacing, ft.

$\beta$ = Joint open/close coefficient assumed equal to 0.85 for a stabilized base 0.65 for a unbound granular base.

$T_{mean}$ = Mean monthly nighttime mid depth temperature, $^0$F.

$T_{constr}$ = PCC temperature at set, $^0$F.

*Step 5.1.3 Determine joint shear capacity*

$$S = 0.05*h_{PCC*}e^{-0.032jw} - \Delta s_{tot} \quad (76)$$

where,

| | | |
|---|---|---|
| $s$ | = | Dimensionless aggregate joint shear capacity. |
| jw | = | Joint opening, mils (0.001 in). |
| h | = | PCC slab thickness, in. |
| $\Delta s_{tot}$ | = | Cumulative loss of sheer capacity at the beginning of the current month. |

*Step 5.1.4 Calculate aggregate joint stiffness*

The aggregate joint stiffness is determined as a function of load shear capacity, S.

$$Log(J_{AGG}) = -28.4 * e^{-e^{-\left(\frac{S-e}{f}\right)}} \quad (77)$$

where,

| | | |
|---|---|---|
| $J_{AGG}$ | = | $(Agg/kl)_c$ = Joint stiffness on the transverse joint for current increment. |
| e | = | 0.35. |
| f | = | 0.38. |
| S | = | Joint shear capacity (equal to $s_0$ at the first time increment). |

*Step 5.1.5 Calculate aggregate interlock LTE*

Load transfer efficiency due to aggregate interlock is determined using the following equation:

$$LTE_{AGG} = \frac{100}{1 + 1.2 * J_{AGG}^{-0.849}} \quad (78)$$

where,

| | | |
|---|---|---|
| $LTE_{AGG}$ | = | Load transfer efficiency on the transverse joint due to aggregate interlock. |
| $_{AGG}$ | = | Transverse joint stiffness. |

*Step 5.1.6 Calculate dowel contribution to joint stiffness (if dowels are present).*

A nondimensional stiffness of a joint due to dowel is determined as follows:

$$J_d = J_d^* + (J_0 - J_d^*)\exp(-DAM_{dowels}) \quad (78)$$

where:

| | | |
|---|---|---|
| $J_d$ | = | Nondimensional dowel stiffness. |

$J_0$ = Initial nondimensional dowel stiffness.
$J^*_d$ = Critical nondimensional dowel stiffness.
$DAM_{dowels}$ = Damage accumulated by a doweled joints due to past traffic.

*Step 5.1.7 Calculate dowel component of LTE*

Dowel component of LTE is determined as follows:

$$LTE_{dowel} = \frac{100}{1+1.2*J_d^{-0.849}} \quad (79)$$

*Step 5.1.8 Calculate total joint LTE for the current month*

$$LTE_{joint} = 100\left(1-(1-LTE_{dowel}/100)(1-LTE_{agg}/100)(1-LTE_{base}/100)\right) \quad (80)$$

**Step 6. Calculate effective slab parameters**

Step 6.1 Find effective slab thickness

$$H_{eff,MONTH} = \sqrt{h_{PCC}^2 + \frac{E_{BASE,\,\mathrm{MONTH}}}{E_{PCC,\,\mathrm{MONTH}}} H_{BASE}^2} \quad (81)$$

$H_{eff,,\,MONTH}$ = Effective slab thickness.
$h_{PCC}$ = PCC slab thickness.
$H_{BASE}$ = Base thickness.
$E_{PCC,\,MONTH}$ = Representative PCC modulus of elasticity for month MONTH.
$H_{BASE,\,MONTH}$ = Base modulus of elasticity for month MONTH.

Step 6.2 Calculate unit weight of the equivalent slab

$$\gamma_{eff,MONTH} = \frac{\gamma_{PCC} h_{PCC}}{H_{eff,MONTH}} \quad (82)$$

where

$\gamma_{eff,\,MONTH}$ = Effective unit weight.
$h_{PCC}$ = PCC slab thickness.
$\gamma_{PCC.}$ = PCC unit weight.
$h_{eff}$ = Effective thickness.

Step 6.3 Find radius of relative stiffness for this month

$$\ell = \sqrt[4]{\frac{E_{PCC,MONTH} H_{eff,MONTH}^3}{12(1-\mu_{PCC}{}^2)k_{MONTH}}} \quad (83)$$

| | | |
|---|---|---|
| $H_{eff,, MONTH}$ | = | Effective slab thickness. |
| $E_{PCC, MONTH}$ | = | Representative PCC modulus of elasticity for month MONTH. |
| $\mu_{PCC}$ | = | Poisson's ratio for PCC. |
| $k_{, MONTH}$ | = | Coefficient of subgrade reaction for this month. |

**Step 7. Calculate effective temperature difference**

Step 7.1 Calculate shrinkage contribution to curling

Moisture warping is adjusted seasonally based on atmospheric relative humidity as follows:

$$\Delta T_{SH,MONTH} = \frac{t}{t+n} \Delta T_{SH,m} \quad (84)$$

where,

| | | |
|---|---|---|
| $\Delta T_{SH,MOMTH}$ | = | Temperature gradient equivalent of moisture warping for month MONTH, °F. |
| $\Delta T_{SH,mHi}$ | = | Equivalent temperature gradient of long term moisture warping for month m (the same month of the year as MONTH) determined in Step2, °F. |
| t | = | Time since placement, days. |
| n | = | Time to achieve 50 percent of ultimate shrinkage strain, days. Use n = 35, unless more accurate information is available. |

Step 7.2 Calculate effective temperature differential

Equivalent temperature differential is determined from the following equation:

$$\Delta T_{eff,MONTH} = \frac{h_{PCC}^2}{H_{eff,MONTH}^2} * \left[ (T_{top,MONTH} - T_{bot,MONTH}) + \Delta T_{BI} + \Delta T_{sh,MONTH} \right] \qquad MONTH = 1,12 \quad (85)$$

where

| | | |
|---|---|---|
| $\Delta T_{eff}$ | = | Difference between temperatures at the top and bottom surfaces of the effective slab. |
| $T_{top, MONTH}$ | = | Mean night temperature of the top PCC surface for month m. |
| $T_{bot, MONTH}$ | = | Mean night temperature of the bottom PCC surface for month m. |
| $\Delta T_{BI}$ | = | Built-in curling and temperature shrinkage temperature differential. |
| $\Delta T_{sh, MONTH}$ | = | Equivalent temperature differential due to reversible portion of shrinkage. |

$h_{PCC}$ = PCC thickness.
$H_{eff,\ MONTH}$ = Effective thickness computed.

Step 7.3 Compute Korenev's nondimensional temperature gradient

$$\phi_{MONTH} = \frac{2\,\alpha_{PCC}\,(1+\mu_{PCC})\ell^{2}_{MONTH}}{H_{eff,MONTH}{}^{2}} \frac{k_{MONTH}}{\gamma_{eff,MONTH}} \Delta T_{eff,MONTH} \quad (86)$$

where

$\phi_{MONTH}$ = Nondimensional temperature gradient for month m.
$h_{PCC}$ = PCC slab thickness.
$\alpha_{PCC}$ = PCC coefficient of thermal expansion.
$\mu_{PCC}$ = Poisson's ratio for PCC.
$\gamma_{eff.\ MONTH}$ = Effective unit weight for month m.
$k_{MONTH}$ = Modulus of subgrade reaction (k-value) for month m.
$\ell_{MONTH}$ = Radius of relative stiffness for month m.
$\Delta T_{eff,\ MONTH}$ = Effective temperature gradient for month m.

**Step 8. Compute adjusted load/pavement weigh ratios (normalized loads)**

For each category of axle types and weights, compute normalized load:

$$q_i * = \frac{P_i}{A\,\gamma_{eff,MONTH} H_{eff,MONTH}} \quad (87)$$

where

$q_i$* = Adjusted load/pavement weigh ratio.
$P_i$ = Axle load.
$h_{PCC}$ = PCC slab thickness.
$\gamma_{PCC}$ = PCC unit weight.
A = Parameter depending on axle type.
= 1 for single axles.
= 2 for tandem axles.
= 3 for tridem axles.

**Step 9. Compute critical deflections**

Step 9.1 Compute NN deflections in the loaded slab

Using NN, compute axle loading induced deflections in the equivalent structure that has the same radius of relative stiffness, joint spacing, Korenev's nondimensional temperature gradient, traffic offset, normalized load ratio, transverse joint LTE, and shoulder LTE.

$$\delta_{L,i,A} = \frac{34100596.7 H_{eff,MONTH}}{\ell_{MONTH}^4 \; k_{MONTH}} [NN_{L,A}(JTSpace, \ell, LTE_{sk}, LTE_{jt,} \phi, q_i^{*}{}_{L,i}, s) - NN_{L,A}(JTSpace, \ell, LTE_{sk}, LTE_{jt,} \phi, 0, s)] \quad (88)$$

Where

$\delta_{L,i,A}$ = Corner deflections of the loaded slab caused by axle loading of type A and weigh category i.

$NN_{L,A}$ = Neural networks for computing deflections at the loaded slab corners due to temperature curling and axle type A.

A = Axle type index.
= 1 for single axles.
= 2 for tandem axles.
= 3 for tridem axles.

i = Parameter defining axle weight.

JTSpace = Mean transverse joint spacing.

$q_i$* = Adjusted load/pavement weigh ratio.

$\phi$ = Nondimensional temperature gradient for the current month.

$\ell$ = Radius of relative stiffness for the current month.

$LTE_{sh}$ = Shoulder load transfer efficiency for flat slab conditions.

$LTE_{jt}$ = Transverse joint load transfer efficiency for flat slab conditions.

s = Traffic wander.

Step 9.2 Compute NN deflections in the unloaded slab

Using NN, compute axle loading induced deflections in the equivalent structure that has the same radius of relative stiffness, joint spacing, Korenev's nondimensional temperature gradient, traffic offset, normalized load ratio, transverse joint LTE, and shoulder LTE.

$$\delta_{U,i,A} = \frac{34100596.7 H_{eff,MONTH}}{\ell^4_{MONTH}\ k_{MONTH}} [NN_{U,A}(JTSpace, \ell, LTE_{sh}, LTE_{jt,} \phi, q^*_{A,i}, s) - NN_{U,A}(JTSpace, \ell, LTE_{sh}, LTE_{jt,} \phi, 0, s)] \quad (89)$$

Where

$\delta_{U,i,A}$ = Corner deflections of the loaded slab caused by axle loading of type A and weigh category i.

$NN_{U,A}$ = Neural networks for computing deflections at the loaded slab corners due to temperature curling and axle type A.

A = Axle type index.

= 1 for single axles.
= 2 for tandem axles.
= 3 for tridem axles.

i = Parameter defining axle weight.

JTSpace = Mean transverse joint spacing.

$q_i$* = Adjusted load/pavement weight ratio.

$\phi$ = Nondimensional temperature gradient for the current month.

$\ell$ = Radius of relative stiffness for the current month.

$LTE_{sh}$ = Shoulder load transfer efficiency for flat slab conditions.

$LTE_{jt}$ = Transverse joint load transfer efficiency for flat slab conditions.

s = Traffic wander.

**Step 10. Compute differential energy increment deflections**

$$DE_{MONTH} = \sum_{A=1}^{3} \sum_{i=1}^{N_A} n_{i,A} \left( k_{MONTH} \frac{\delta_{L,i,A}^2}{2} - k_{MONTH} \frac{\delta_{U,i,A}^2}{2} \right) \qquad (90)$$

where

$DE_{MONTH}$ = Differential energy density of subgrade deformation accumulated for month MONTH.

$\delta_{L,i,A}$ = Corner deflections of the loaded slab caused by axle loading.

$\delta_{U,i,A}$ = Corner deflections of the unloaded slab caused by axle loading.

$n_{i,A}$ = Number of axle load applications for current increment and load group *j*.

$N_A$ = Number of load categories for the axle type A.

**Step 11. Find faulting increment**

Determine increment of faulting accumulated for month MONTH.

$$\Delta Fault = C_{34} * (FMAX_{MONTH-1} - FAULT_{MONTH-1})^2 * DE_{MONTH} \qquad (91)$$

where

$\Delta Fault$ = Increment of faulting accumulated for month MONTH.

$FAULT_{MONTH-1}$ = Magnitude of faulting at the beginning of month MONTH.

= 0 if MONTH =1.

$FMAX_{MONTH-1}$ = Maximum faulting parameter at the beginning of month MONTH.

= $FMAX_0$ if MONTH =1.

$DE_{MONTH}$ = Differential energy density of subgrade deformation accumulated for month MONTH.

$C_{34} = C_3 + C_4 * FR^{0.25}$

FR = Base freezing index.

$C_3$ and $C_4$ are calibration parameters:

$C_3$ = 0.001725

$C_4$ = 0.0008

**Step 12. Find current faulting**

$$FAULT_{MONTH} = FAULT_{MONTH-1} + \Delta Fault \quad (92)$$

where

| | | |
|---|---|---|
| $FAULT_{MONTH}$ | = | Magnitude of faulting at the end of month MONTH. |
| $FAULT_{MONTH-1}$ | = | Magnitude of faulting at the beginning of month MONTH. |
| | = | 0 if MONTH =1. |
| $\Delta Fault$ | = | Increment of faulting accumulated for month MONTH. |

**NOTE: steps 13 through 15 are not necessary for the last month of the design period.**

**Step 13. Find current maximum faulting index**

Find current maximum faulting index

$$FMAX_{MONTH} = FMAX_{MONTH-1} + C_7 * DE_{MONTH} \left[ Log(1 + C_5 * 5^{EROD}) \right]^{C_6} \quad (93)$$

where

| | | |
|---|---|---|
| $FMAX_{MONTH}$ | = | Maximum faulting parameter at the end of month MONTH. |
| $FMAX_{MONTH-1}$ | = | Maximum faulting parameter at the beginning of month MONTH |
| | = | $FMAX_0$ if MONTH =1. |
| $DE_{MONTH}$ | = | Differential energy density of subgrade deformation accumulated for month MONTH. |
| EROD | = | Erodibility of the base layer. |
| $C_5$ | = | 250 |
| $C_6$ | = | 0.4 |
| $C_7$ | = | 1.2. |

**Step 14 Evaluate loss of aggregate shear capacity**

Step 14.1 Calculate reference shear stress

$$\tau_{ref} = 111.1 * exp(-exp(0.9988 * exp(-0.1089 \log J_{AGG}))) \quad (94)$$

where

| | | |
|---|---|---|
| $\tau_{ref}$ | = | Reference shear stress derived from the PCA test results. |
| $J_{AGG}$ | = | Aggregate joint stiffness computed for the time increment. |

Step 14.2 Calculate shear stress induced by each axle

$$\tau_{iA} = J_{AGG} * \left( \delta_{L,i,A} - \delta_{U,i,A} \right) \quad (95)$$

where

$\tau_{iA}$ = Maximum shear stress at the PCC slab joint surface caused by axle loading of type A and weigh category i.

$J_{AGG}$ = Aggregate joint stiffness computed for the time increment.

$\delta_{L,i,A}$ = Corner deflections of the loaded slab caused by axle loading.

$\delta_{ij,A}$ = Corner deflections of the unloaded slab caused by axle loading.

A = Axle type index.
= 1 for single axles.
= 2 for tandem axles.
= 3 for tridem axles.

i = Parameter defining axle weight.

Step 14.3 Calculate loss of aggregate shear capacity accumulated during the month

$$\Delta s_{i,A} = \begin{cases} 0 & if \quad jw < 0.001\, h_{PCC} \\ \dfrac{0.005*10^{-6}}{1.0+(jw\ /h_{PCC})^{-5.7}}\left(\dfrac{\tau_{i,A}}{\tau_{ref}}\right) & if \quad 0.001 < jw < 3.8\, h_{PCC} \\ \dfrac{0.068*10^{-6}}{1.0+6.0*(jw\ /h_{PCC}-3)^{-1.98}}\left(\dfrac{\tau_{i,A}}{\tau_{ref}}\right) & if \quad jw > 3.8\, h_{PCC} \end{cases} \quad (96)$$

where

$\Delta s_{i,A}$ = Loss of shear from a single repetition of an axle load of group i and axle type A.

$h_{PCC}$ = PCC slab thickness, in.

jw = Joint opening, mils (0.001 in).

$\tau_{i,A}$ = Shear stress on the transverse joint surface from the response model for the load group i and axle type A.

$\tau_{ref}$ = Reference shear stress derived from the PCA test results.

Step 14.4 Calculate shear stress accumulated during the month

$$\Delta s_{tot} = \sum_{A=1}^{3}\sum_{i=1}^{N_A} \Delta s_{i,A} n_{i,A} \quad (97)$$

where

$\Delta s_{tot}$ = Cumulative loss of sheer for the current month.

$\sum_{i=1}^{Na} \Delta s_{i,A}$ = Loss of shear from a single repetition of an axle load of group i and axle type A.

$n_{i,A}$ = Number of axle load applications for current increment and load group *j*.

$N_A$ = Number of load categories for the axle type A.

Step 14.5 Calculate loss of shear capacity

$$S_{MONTH} = S_{MONTH-1} + \Delta s_{tot} \quad (98)$$

**Step 15. Calculate damage of doweled LTE**

Step 15.1 Calculate dowel shear force

$$F_{i,A} = J_d * \left(\delta_{L,i,A} - \delta_{U,i,A}\right) * DowelSpace \quad (99)$$

where

$F_{i,A}$ = Dowel shear force induced by axle loading of type A and load category i.

$J_d$ = Joint stiffness on the doweled joint computed for the time increment.

$\delta_{L,i,A}$ = Corner deflections of the loaded slab caused by axle loading of type A and load category i.

$\delta_{Ui,A}$ = Corner deflections of the unloaded slab caused by axle loading of type A and load category i.

A = Axle type index.
= 1 for single axles.
= 2 for tandem axles.
= 3 for tridem axles.

i = Parameter defining axle weight.

DowelSpace = Space between adjacent dowels in the wheel path, in.

Step 15.2 Calculate increment of dowel joint damage

Dowel joint damage accumulated for the current month is determined from the following equation:

$$\Delta DOWDAM_{tot} = \sum_{A=1}^{3} \sum_{i=1}^{Na} C_8 * F_{i,A} \frac{n_{i,A}}{d\, f_c^*} \quad (100)$$

where

$\Delta DOWDAM_{tot}$ = Cumulative dowel damage for the current month.

$F_{i,A}$ = Dowel shear force induced by axle loading of type A and load category i.

$n_{i,A}$ = Number of axle load applications for current increment and load

group i.

$N_A$ = Number of load categories for the axle type A.

$f_c^*$ = PCC compressive stress estimated from the PCC modulus of rupture, Mr, using the following equation:

$$f_c^* = \left(\frac{Mr}{9.5}\right)^2 \quad (101)$$

$C_8$ = Calibration constant.
$C_8$ = 400.

Step 15.3 Find total dowel damage

$$DOWDAM_{MONTH} = DOWDAM_{MONTH-1} + \Delta DOWDAM_{tot} \quad (102)$$

$DOWDAM_{MONTH}$ = Dowel damage at the end of month MONTH.
$DOWDAM_{MONTH-1}$ = Dowel damage at the beginning of month MONTH.
= 0 if MONTH=1
$\Delta DOWDAM_{tot}$ = Cumulative dowel damage for the current month.

## REFERENCES


1. Owusu-Antwi, E.B. and M.I. Darter. "Early Results of the LTPP Concrete Pavement Data Analysis." Third International Workshop on the Design and Evaluation of Concrete Roads, Vienna, Austria, 1994.
2. Darter M. I., J. M. Beck, M.B. Snyder, and R.E. Smith. "Portland Cement Concrete Pavement Evaluation System-COPES," *NCHRP Report 277*, Transportation Research Board, Washington, DC, 1985.
3. Yu, H.T., M.I. Darter, K.D. Smith, J. Jiang and L. Khazanovich. *Performance of Concrete Pavements Volume III - Improving Concrete Pavement Performance.* Final Report, Contract DTFH61-91-C-00053, Federal Highway Administration, McLean, VA, 1996.
4. Permanent International Association of Road Congresses. *Combating Concrete Pavement Slab Pumping by Interface Drainage and Use of Low-Erodibility Materials: State of the Art and Recommendations*, Permanent International Association of Road Congresses, Paris, France, 1987.
5. Christory, J.P. "Assessment of PIARC Recommendations on the Combatting of Pumping in Concrete Pavements." *Sixth International Symposium on Concrete Roads*. Madrid, Spain, 1990.
6. Owusu-Antwi, E.B., L. Titus-Glover, L. Khazanovich, and J.R. Roesler. "Development and Calibration of Mechanistic-Empirical Distress Models for Cost Allocation." Final Report, Federal Highway Administration, Washington, DC, March 1997.
7. Titus-Glover, L., E. Owusu-Antwi, and M I. Darter. *Design and Construction of PCC Pavements, Volume III: Improved PCC Performance.* Report No. FHWA-RD-98-113, Federal Highway Administration, Washington, DC, January 1999.
8. Wu, C.L., J.W. Mack, P.A. Okamoto, and R.G. Packard. "Prediction of Faulting of Joints in Concrete Pavements," *Proceedings, Fifth International Conference on Concrete Pavement Design and Rehabilitation, Vol. 2.*, Purdue University, West Lafayette, IN, April 1993.
9. ERES Consultants Inc., "Evaluation of Unbonded Portland Cement Concrete Overlays," NCHRP, Transportation Research Board, Washington, DC, 1998.
10. Highway Research Board. "The AASHO Road Test–Report 5, Pavement Research." *Special Report 61E*. National Academy of Sciences–National Research Council, Washington, DC: Highway Research Board, 1962.
11. Poblete, M. "Informe Anual 1986," Control y Seguimiento de Pavimentos de Hormigon, IDIEM-Direccion de Vialidad, Universidad de Chile, 1986.
12. Neal, B.F. *Evaluation of Design Changes and Experimental PCC Construction Features*. FHWA/CA/TL-85/07. Sacramento, CA: California Department of Transportation, 1987.
13. Simpson, A.L., J.B. Rauhut, P.R. Jordahl, E. Owusu-Antwi, M.I. Darter, and R. Ahmad. *Early Analysis of LTPP General Pavement Studies Data, Volume 3: Sensitivity Analyses for Selected Pavement Distresses*, Report SHRP-P-393, Strategic Highway Research Program, Washington, DC, 1994.
14. Packard, R.G. "Design Considerations for Control of Joint Faulting of Undoweled Pavements," *Proceedings of the International Conference on Concrete Pavement Design*. Lafayette, IN: Purdue University, 1977.

15. Yu, H.T., L. Khazanovich, S.P. Rao, M.I. Darter, and H. Von Quintus. *Guidelines for Subsurface Drainage Based on Performance, Appendices*. Washington, DC: National Cooperative Highway Research Program, Project 1-34, August 1998.
16. Hoerner, T.E., M.I. Darter, L. Khazanovich, L. Titus-Glover, and K.L. Smith. *Improved Prediction Models for PCC Pavement Performance-Related Specifications, Volume I: Final Report,* Publication No. FHWA-RD-00-130, August 2000.
17. Larralde, J. "Structural Analysis of Rigid Pavements with Pumping," Ph.D. thesis, Purdue University, West Lafayette, IN, 1984.
18. Van Wijk, A.J., Larralde, J., Lovell, C.W., and Chen, W.F. "Pumping Prediction Model for Highway Concrete Pavements," ASCE, *Journal of Transportation Engineering*, Vol. 115, No. 2, 1989, pp. 161-175.
19. Bhatti, M.A., Barlow, J.A., and Stoner, J.W. "Modeling Damage to Rigid Pavements Caused by Subgrade Pumping," ASCE, *Journal of Transportation Engineering*, Vol. 122, No. 1, Jan-Feb 1996, pp. 12-21.
20. Yao, Z. "Design Theory and Procedure of Concrete Pavements in China," 2nd International Workshop on the Theoretical Design of Concrete Pavements, Siguenza, Spain, 1990.
21. Permanent International Association of Road Congresses. *Combating Concrete Pavement Slab Pumping by Interface Drainage and Use of Low-Erodibility Materials: State of the Art and Recommendations*, Permanent International Association of Road Congresses, Paris, France, 1987.
22. De Beer, M. "Erodibility of Cementitious Subbase Layers in Flexible and Rigid Pavements." Second International Workshop on the Theoretical Design of Concrete Pavements, Siguenza, Spain, 1990.
23. Dempsey, B.J., Carpenter, S.H., and M.I. Darter. "Improving Subdrainage and Shoulders of Existing Pavements," FHWA, Final Report, 1980.
24. Dempsey, B.J., "Laboratory and Field Studies of Channeling and Pumping," Transportation Research Board, *Transportation Research Record 849*, 1982, pp. 1-12.
25. Ioannides, A.M., and G.T. Korovesis. "Aggregate Interlock: A Pure-Shear Load Transfer Mechanism." *Transportation Research Record 1286.* Transportation Research Board, Washington, DC, 1990.
26. Ioannides, A.M., and G.T. Korovesis. "Analysis and Design of Doweled Slab-On-Grade Pavement Systems." *Journal of Transportation Engineering*, ASCE, Vol. 118, No. 6, New York, 1992, pp. 745-768.
27. Zollinger, D.G., N. Buch, D. Xin, and J. Soares. *Performance of CRCP Volume 6 - CRCP Design, Construction, and Performance*, FHWA-RD-97-151, Report, U.S. Department of Transportation, Washington, DC, February 1998.
28. Freiberg, B.F. "Design of Dowels in Transverse Joints of Concrete Pavements," *Transactions*, ASCE. Volume 105, 1940.
29. Tabatabie, A.M. and Barenberg, E.J. "Structural Analysis of Concrete Pavement Systems," *ASCE, Transportation Engineering Journal.* Vol. 106, No. 5, 1980, pp. 493-506.
30. Scarpas, A., E. Ehrola, and J. Judycki. "Simulation of Load Transfer Across Joints in RC Pavements," *Proceedings*, Third International Workshop on the Design and Evaluation of Concrete Pavements, Krumbach, Austria, 1994, pp. 113-122.
31. Guo H, J.A. Sherwood, and M.B. Snyder. "Component Dowel-Bar Model for Load-Transfer Systems in PCC Pavements," *Journal of Transportation Engineering*, Vol. 121, 1996, pp. 289-298.

32. Davids, W.G., G.M. Turkiyyah, and J. Mahoney. "EverFE—A New Rigid Pavement Finite Element Analysis Tool," *Transportation Research Record*, Washington, DC: National Research Council, 1998, pp. 69-78.
33. Khazanovich, L., H.T. Yu, S. Rao, K. Galasova, E. Shats, and R. Jones. *ISLAB2000—Finite Element Analysis Program for Rigid and Composite Pavements. User's Guide*. ERES Consultants, Champaign, IL, 2000.
34. Hutchinson, R.L. "Resurfacing With Portland Cement Concrete." *NCHRP Synthesis of Highway Practice 99,* 1982.
35. Birmman, D. "Erosion of Cement Treated Subbases Below Concrete Pavements." Eighth International Symposium on Concrete Roads. Theme III, Pavement Performance and Evaluation. Lisbon, Portugal, 1998.
36. Khazanovich, L., M. Darter, and R. Bartlett. *Common Characteristics of Good and Poorly Performing PCC Pavements.* Federal Highway Administration, Washington, DC, 1997.

2do

1. references
2. database
3. reliability